High Power Chirally-Couple-Core (CCC) Fiber Lasers for Coherent Combining Systems

by

Cheng Zhu

A dissertation submitted in partial fulfillment
of the requirements for the degree of
Doctor of Philosophy
(Electrical Engineering)
in The University of Michigan
2014

Doctoral Committee:

Professor Almantas Galvanauskas, Co-chair
Professor Herbert G. Winful, , Co-chair
Associate Professor Alexander G. R. Thomas
Professor Kim A. Winick

Dedicated to my parents

ACKNOWLEDGEMENTS

I would never have been able to survive through the graduate years without help and caring from many people.

First and foremost, I would like to express my sincere gratitude to my advisor Professor Almantas Galvanausks, for his continuous guidance and support throughout my PhD studies. His confidence in me encouraged me through many bottlenecks. His patience and generosity helped me through many tough times. His perspective and enthusiasm in research has also motivated and guided me in many interesting works. I will always be grateful to all his academic guidance and support.

I would also like to thank my committee members, Professeror Kim Winick, Professor Herbert Winful and Professor Alexander Thomas for taking time out from their busy schedules to review my research work and participated in my dissertation proposal and final oral defense. In addition, I would like to thank Professor Kim Winick for all the generous help and kind advices offered on my graduate life and future career. I would like to thank Professor Herbert Winful for the great Nonlinear Optics course he offered. His unique style of teaching makes the whole learning delightful and fruitful. I would also like to thank Professor Alexander Thormas for always being nice and readily to help when I knocked on door and interrupted his work.

I am also thankful to Dr. Peter Weßels and Malte Karrow in Laser Zentrum Hannover for the support in collaboration work of modal content measurement for CCC fibers. I would like to thank John Nees for always being there and willingly to help when I encountered problems in

experiments. I would also like to thank all the staff in EE department and CUOS, especially Linda Owens, Bett Weston, Shonda Bottke, Deb Dieterie, Car Nosel, Beth Stalnaker and Steven Pejuan. Their work makes my graduate and research life much easier.

I am blessed to have been work with many excellent and talented colleagues. Many thanks to Richard Hou, Chi-Hung Liu and Shenghong Huang for the great guidance and help they offered in the beginning years of my graduate study. I am also grateful to Craig Swan, Matt Rever, Wei-Zung Chang, Leo Siiman, Michael Haines and Paul Stanfield for the cheerful chats and helps in the lab. I am also thankful to Tong Zhou and John Ruppe for the cooperation in a challenging work and always been friendly and sharing with me their understandings on coherent combining and ultra-fast optics. Moreover, I owe a lot of debt to Xiuquan Ma and I-Ning Hu. Many thanks to Xiuquan Ma for educating me with knowledge on CCC fibers and especially for his excellent work on CCC fiber designing which makes most of my graduate research possible. Deeply appreciations to I-Ning Hu for fruitful discussions on thermal effects, fiber laser and polarization in fibers, standing next to the emergency button during my power scaling experiments, and cheering me up when I am frustrated.

I also would like to thank many of my friends who enriched my life in Ann Arbor: Lu Tian, Ruixuan Li, Ning Wang, Yang Lin, Guang Yang, Ling Gao, Chi-Mei Liu, Ning Wang (EECS), Cheng Li, Yuxing Luo. I am also grateful to my friends in China, whose support and caring never stopped over the long distance: Wenyan Xu, Yan Tie, Xiaoxue Yang.

Last but not the least, I want to express special thanks to my parents and cousin Beiyi Jin for being the constant source of support and love for me throughout all of the years. And deepest gratitude to my husband, Zhouzhou Zhao, whose understanding, support and love accompanied me all the way through.

TABLE OF CONTENTS

LIST OF FIGURES

LIST OF TABLES

ABSTRACT

High Power Chirally-Couple-Core (CCC) Fiber Lasers for Coherent Combining Systems

by

Cheng Zhu

Chair: Almantas Galvanauskas

High-power fiber lasers constitute a rapidly developing technology, with numerous current and future applications ranging from industrial to fundamentals scientific. The revolutionary advances of high-power fiber lasers are primarily associated with the development of large core fibers. Over the last 10 years there have been numerous innovations proposed and demonstrated that aim to increase fiber core size while maintaining diffraction limited beam output. One broad class of solutions are so-called photonic-crystal rod fibers, with core sizes currently reaching up to 135μm, but which achieve that core size at the cost of sacrificing their compatibility with compact integration by fiber splicing, coiled packaging, etc. Alternative solutions based on so-called chirally-coupled core (CCC) fibers have been recently demonstrated with the cores sizes reaching around 60μm and operating with robust single-mode output, which are completely compatible with standard fiber processing approaches based on fusion splicing

and coiled packaging, and which, therefore, are well suited for developing monolithically-integrated compact and robust high power fiber laser systems.

In this dissertation we present a detailed study of using this novel CCC fiber technology for high pulse energy and high average power systems. Particular emphasis here is for using this CCC technology for different types of coherently-combined fiber laser arrays, where compatibility of CCC fiber technology with monolithic integration becomes an enabling factor for constructing complex but practical high-power laser "circuitry".

In this thesis, we first develop a detailed theoretical and experimental study of general power handling and thermal characteristics in high power fiber amplifiers, with particular emphasis on specific aspects associated with CCC fibers (or, in general, with any effectively single-mode fibers), such as impact of modal leakage from a fiber core on the fiber amplifier and laser efficiency. Furthermore, we explore the unique polarization preservation characteristics of CCC fibers, which, as we show here are primarily the result of their spun nature, and their effectively single-mode performance. Practical importance of these findings is that they provide theoretical foundation for design guidelines to achieve stable polarization preservation in high power CCC fiber systems. In subsequent chapters we present experimental exploration of high average power scaling of CCC fiber amplifiers, reporting up to 576W of single frequency output from a 37μm core CCC fiber amplifier, as well as a laboratory study of large-core CCC fiber amplifier modal output performance at high average powers. Further chapters of the thesis are devoted to high energy pulsed operation of large core CCC fibers. First, we report demonstration of up to 9.1mJ at ~1MW peak power extraction from a 55μm core Yb-doped double-clad CCC fiber amplifier, the highest ever reported pulse energy from any effectively single-mode large-core fiber. Then we theoretically explore novel pulsed pumping approach, which could lead to an

order of magnitude increase in extracted pulsed energies compared to what is currently possible with cw pumping. For example, when applied to 55μm core CCC fiber and used in conjunction with a recently demonstrated coherent pulse stacking technique, this approach could lead to the generation of ~100mJ energy ultrashort pulses from a single fiber amplifier. This would constitute a two-orders of magnitude increase of fiber CPA energies from the current state-of-the-art.

To summarize, the results of the work presented in this thesis establish a foundation for using CCC fibers in high power pulsed laser systems. We anticipate that this contribution will be particularly useful when developing coherently combined fiber amplifier arrays based on CCC fiber technology, and high intensity (TW to PW peak power) kHz repetition rate ultrashort-pulse laser systems for driving laser plasma accelerators in particular.

Chapter 1

Introduction

1.1 Current status of high power fiber lasers

Over the last decade fiber lasers have enabled remarkable advance in average power and energy scaling. With important practical advantages such as diffraction-limited beam output, high efficiency, as well as the robustness and compactness, fiber lasers are very attractive as high-power and high-energy laser sources for various applications ranging from high field science research to materials processing and industrial micromachining.

Shortly after the demonstration of the first Ruby laser [1,2], lasing in Nd: glass fiber was demonstrated in the early 1960s [3,4] using discharge-lamp pumping. Further progress in fiber lasers was tied to the development of laser diode pumps and the development of high quality (single mode and low loss) optical fibers. First demonstration of fiber laser diode pumping was achieved in early 1970's [5,6], and single-mode optical fibers were also developed at about the same time in response to the ideas promoted by Charles Kao of using optical fibers for high-speed telecommunications (Nobel Prize in Physics in 2009 [7]). However, it was not until 1985 when the first single mode fiber laser was demonstrated in Nd-doped low-loss silica fibers [8,9]. Fiber lasers based on other rare earth dopants such as Sr [10], Pr [11], Er [12], Yb [13], Tm [14] have been also demonstrated shortly after that. The introduction of a double cladding structure [15,16] was the beginning of high-power fiber laser development, because this approach enabled pumping with high-power multimode diodes, thus overcoming power scaling limitations

associated with single mode diodes. As shown in Fig. 1.1, the average power form a continuous-wave (CW) fiber lasers with single transverse-mode output exponentially increased from few Watts in early 1990s to around 10kW in late 2000's [17-24]. It is worth noting that all the power records achieved after 1999 were from Yb-doped fiber lasers. Yb doped fibers has shown distinct advantages for high power operations due to its simple electronic structure. With only two 4f energy levels: $^2F_{7/2} \rightarrow {}^2F_{5/2}$, Yb-doped fiber provides a more efficient way for power scaling with elimination of unwanted processes such as excited state absorption, multiphonon non-radiative decay and concentration quenching [26]. In addition, the very broad absorption (from 800nm to 1064nm) and emission (from 970nm to 1200nm) bands respectively also makes it applicable to a wide range of pumping and operation conditions.

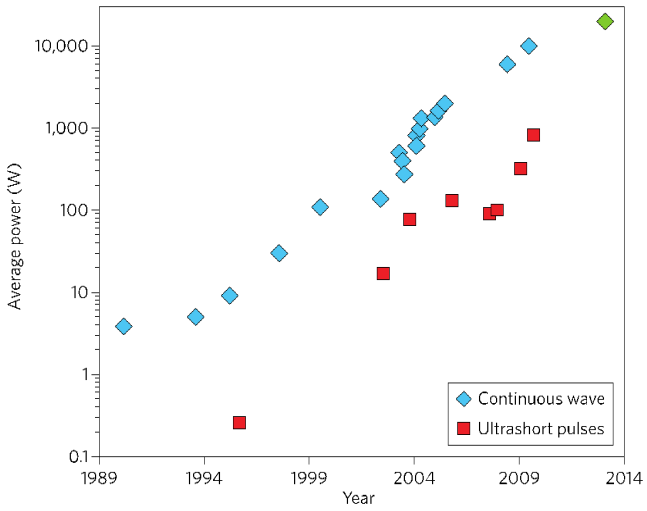

Figure 1.1: Progress in average output power from near-diffraction-limited fiber lasers [25]. Blue marks are power of CW fiber laser output, and the red ones represent average power of ultra-short pulse generation. The green mark is a 20kW CW fiber laser output with unspecified beam quality.

Furthermore, this broad spectral bandwidth is also favored for ultra-short pulse amplification. Ultrafast fiber lasers have also been continuously developing since mid-1990s and recently reached up to 830W of average power [27-29].

Although the scaling of average power with fiber lasers has been exponentially increasing over the past two decades, a number of challenges remains, particularly in achieving high pulse energies. Relatively small core size and long signal propagation distances in a fiber limits achievable peak power due to optical damage and detrimental nonlinear effects. Ultimate limits to pulse energy and peak power are set by optical damage [30] and self-focusing [31]. In general, different nonlinear effects appear as limitations for different types of amplified signals. For example, stimulated Brillouin scattering (SBS) limits achievable power of narrow-linewidth signals, stimulated Raman scattering (SRS) and four-wave mixing are the main limiting factors in nanosecond pulse amplification [31], and self-phase modulation (SPM) is the main limitations occurring in chirped pulse pulse amplification of sub-picosecond pulses [34]. SPM constraints achievable ultrashort pulse energy to ~100μJ to ~1mJ, which is orders of magnitude below the stored energy in a fiber amplifier. General approach that emerged to address these peak power limitations is to increase fiber core size. However, this has lead to a new type of limitation - transverse modal instability (TMI) - which is associated with a multi-mode nature of large-core fibers, when thermally induced grating occurring at high average power due to beating between different modes initiates coupling from fundamental to higher order modes, and thus degrades beam quality at the fiber output [32-33]. To circumvent these barriers towards further power scaling of fiber laser systems, novel approaches in both optical fibers and fiber laser systems are required.

1.2 Chirally-Coupled-Core fibers for integratable high power lasers and laser arrays

The main challenge to increasing fiber core size is the multiple-transverse mode nature of large cores. In the late 1990s, researchers demonstrated that a relatively robust single mode operation in multimode fibers is achievable with core size smaller than 25μm [45,46], by either

careful single-mode excitation or using coiling induced higher-order mode filtering. However, such single-mode operation in a multimode core is very sensitive to perturbations such as stress, misalignment of seed signal, and sensitivity to core mismatch at the splice point between different optical fibers. Furthermore, with increasing core sizes, it becomes increasingly more difficult to achieve modal differentiation between fundamental and higher-order modes (HOMs) using coiling-induced modal filtering.

To increase fiber core size beyond the limitations of these techniques, various novel large output have been proposed and demonstrated over the last decade.

Photonic crystal fibers (PCF), with an air-hole structure in the fiber cladding to effectively lower its refractive index, retains single mode waveguide property in fibers with core sizes of few tens of micrometers [47, 48]. Up to 40μm flexible PCF, as well as 100um rod-type PCF have been developed to fulfill the requirements of a high power fiber amplifier [49, 50]. Pulses with 1ns duration, 4.5MW peak power and 4.3mJ energy has been demonstrated [51]. However, due to the air-hole structure within the fiber and the low core NA nature, splicing of this fiber is very challenging. Furthermore, a rod-type structure, which is necessary for PCF cores larger than 40μm, cannot be coiled making it rather cumbersome to accommodate the complete fiber length (typically ~1m) as a stiff rod, sacrificing the compact aspect of fiber technology.

Recently, large-pitch-fiber (LPF) with up to 135μm has been developed based on HOM delocalization [52]. Up to 26mJ from sub 60ns pulses as well as 3.8Gw from sub 500fs pulses have been demonstrated [53, 54]. However, single mode operation in this fiber can only be achieved in a pumped fiber, with heat deposition present, and thus such fibers can be operated only at a specific power level. This makes it impossible to incorporate passive-fiber components

with similar core sizes. In addition, considering that they can only be made in rod-type geometry, such fibers essentially are a variety of free-space solid-state lasers, used to only achieve power performance, but with none of the technological fiber advantages remaining.

A practical alternative to such "brute-force" approaches, Chirally-Coupled-Core (CCC) fiber has been proposed [55-57], which increases fiber core size with effectively single-mode characteristics while maintaining all relevant fiber attributes such as compatibility with fusion splicing, coiling, and which is compatible with both doped (i.e. "active") and undoped (i.e. "passive") fibers. Unlike conventional fibers, two waveguides or more are introduced into within the fiber structure for CCC fibers. As shown in Fig. 1.3, one of these two waveguides is a large diameter, central (main) core and the other/others are a smaller size, off-center side cores, which are helically wound around the central core. This unique structure is helically symmetric, and interaction in this structure can occur only between helical symmetrical modes. Since, in general, such modes possess optical angular momentum (orbital and spin/polarisation momentum), phase-matched coupling between the modes occurs when matching between various combinations of modal phase velocities and their angular momenta is achieved, i.e. so-called quasi-phase-matching (QPM). Consequently, QPM provides with new degrees of freedom in designing modal interactions in CCC structure, and highly selective modal coupling between the main core and the side core, or directly between the main core and the cladding can be achieved. This modal-coupling selectivity can be exploited to design structures in which the fundamental LP01 mode in the main core remains unaffected, while all higher order modes are coupled into the cladding (either directly or via side-core, which then radiates into the cladding due to its helical curvature). Operation of properly designed CCC structures has been shown to be

effectively single-mode, and very robust and insensitive to external perturbations and excitation conditions [55-57].

Both passive (i.e. Ge-doped) and active - amplifying Yb-doped large core CCC fibers have been fabricated and demonstrated. Various lasing and amplification experiments have been reported. With single-side structure, up to 37μm CCC fiber has been demonstrated with both passive and active doping. 200W output power (130W compressed) with pulse duration of 350fs has been generated with a 35μm CCC fiber based CPA system [58]. Up to 600W SBS free single frequency amplifier output was achieved with single transverse mode output and single polarization [59] (Chapter IV). For core size scaling over 40μm, an advanced structure with multi-side core was introduced and successfully demonstrated with up to 60μm passive fiber and 55μm Yb-doped fiber. SRS suppression using spectrally tailored transmissions of CCC has been demonstrated with up to 140kW coupled in a 4m long Ge-doped 60μm CCC fiber [60]. A nanosecond pulse amplifier based on 55μm CCC fiber has been demonstrated, emitting 10ns pulses with energy of 9.1mJ and close to 1MW peak power and no SRS onset [61] (Chapter V).

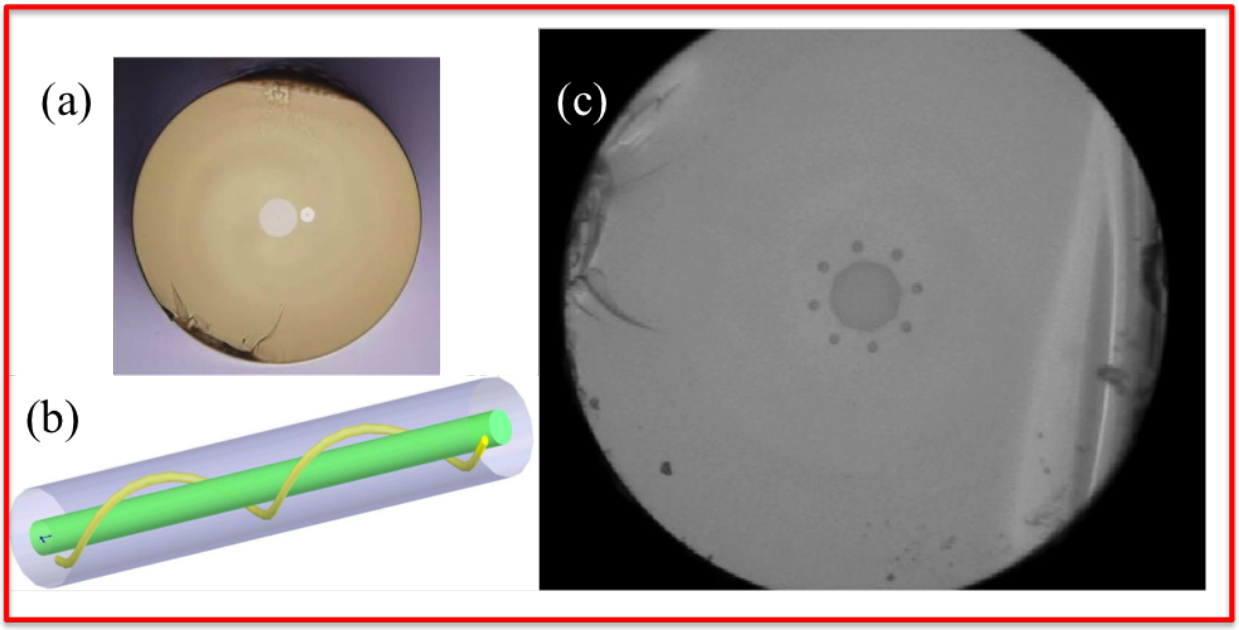

Figure 1.2: Illustration of structure of CCC fibers: a) single-side CCC fiber, b) 3D geometry of CCC structure, c) multi-side CCC fiber with a polygonal shaped central core

Although none of the demonstrated CCC fiber structures have any polarisation-preserving means in them, experimental empirical evidence unexpectedly revealed very robust polarization-preserving performance of CCC based laser and amplifier structures [59, 62]. The detailed description of this polarisation-preserving performance as well as through analysis of its origins is presented in Chapter III of this thesis.

In summary, unlike PCF-based large core fibers, CCC fibers are all-glass and flexible structures, which are completely compatible with coiled packaging and standard fusion splicing. Strong HOM suppression also ensures negligible modal-scattering loss at the splicing points between different CCC fibers, or even between single-mode and CCC fibers. Consequently, CCC fiber is a large-core and core-size scalable structure that maintains all advantageous attributes of conventional single-mode fibers, and thus serves as a technological platform for

developing full range of standardized integratable passive and active components for practical high power monolithic fiber laser systems.

1.3 Coherent combining system

Active coherent combining of several fiber laser channels is a promising approach for average power scaling to over 100kW [35]. Average and peak power in individual fiber channels could be at a relatively low level, so that all the peak power dependent nonlinear effects mentioned in the previous section could be mitigated. With applying this technique single frequency fiber amplifier arrays with over 2kW of output power have been demonstrated [36].

Recently it has been also recognized that coherent combining of multiple parallel fiber CPA channels offers a path towards simultaneously achieving high average power and high pulse energy in ultrashort-pulse systems. One of the most interesting scientific as well as practical application areas for such sources would be high-intensity laser driven plasma acceleration, and other high-intensity laser-matter interactions. The problem is that none of the existing solid-state (or other) laser technologies can offer even a potential solution. Currently, fiber laser arrays appear to be the only viable path. This approach is at the early stages of development, with up to four femtosecond-CPA channels combining demonstrated [123], and up to 1.3mJ and 530W average power with sub-picosecond pulses achieved [37]. This still very far from the objective of achieving pulses in the 100mJ to >10J range, which will require much larger array sizes.

The challenge of reaching 1J to >10J pulse energies is associated with very large array sizes that would be needed. Indeed, considering that individual fiber CPA channel is limited in energy of approximately 100μJ to 1mJ, reaching such energies would require array sizes of the order of 10^4 - 10^5 parallel channels. Such astronomically large array sizes certainly present a

formidable technological challenge. Recently our group introduced an idea of temporal pulse stacking, which allows to overcome individual FCPA-channel peak power limitations and to potentially extract all stored pulse energy with negligible nonlinearity. Such pulse stacking can be considered as a time-domain coherent pulse combining technique. In this coherent pulse stacking (CPS) technique [42] single pulse amplification is substituted by amplification of a burst of multiple pulses, which are stacked into a single pulse at the system output. This effectively increases amplified pulse duration so that the peak power of individual pulses in an amplifier is reduced, and the peak-power related nonlinear effects are mitigated. CPS technique is implemented by taking high-repetition mode-locked laser oscillator periodic pulse train and "carving" it into properly amplitude and phase modulated pulse bursts, each of which after amplification is stacked into a single output pulse using Gires-Tournois Interferometer cavities [43]. Theoretical analysis of this CPS technique shows that large number of 100 to 1000 equal-amplitude pulses per burst can be stacked into a single pulses, thus providing similar extractable energy enhancement for an individual FCPA channel. This thesis is not addressing implementation of the CPS technique itself. However, ability to amplify effectively very long (~100ns to ~1μs) pulses calls for analysis of how much pulse energy can be extracted from a large core fiber amplifier, given that pulse duration limitations are removed. In Chapter VI we present such an analysis, where we show that by using novel pulsed pumping scheme one can increase extractable energy with such effectively-long pulses by an order of magnitude, to potentially ~100mJ for 55μm CCC fibers. This have an immediate implication for the required FCPA array sizes, potentially reducing from 10^4 - 10^5 parallel channels down to 10 - 100 parallel channels for achieving 1J - 10J pulse energies.

It is worth noting that other concepts for temporal pulse combining have been proposed by other groups. Another way to extend single pulse into multiple ones is by splitting and delaying stretched pulse replicas and then compensated the delay and recombine them by a series of Mach–Zehnder-type delay lines, a so-called divided-pulse-amplification (DPA) [41]. This DPA technique, however, is in practice limited to less than ~10 pulses due to delay-line length increasing exponentially with the number of divided pulses, and therefore can not increase FCPA channel energy substantially.

Basic architecture of the envisioned coherently combined system incorporating both spatial beam and temporal pulse combining schemes is outlined in Fig. 1.2. Mode-locked oscillator is a seed source, common to all channels. Fiber CPA is implemented using common pulse stretcher at the system input, and common pulse compressor at the system output. Both pulse stretcher and pulse compressor can be implemented using conventional diffraction-grating based free-space arrangements. Coherent pulse stacking is implemented by using an amplitude and a phase modulator, also common to all channels and placed right after the pulse stretcher, and using GTI reflective-cavity based pulses stacker, common to all channels and positioned right before pulse compressor. Coherently combined fiber array is positioned between the modulation and stacking stages. For implementing spatial combining, the seed signal (in the form of a prepared burst of stretched pulses) is first split into multiple paths, for example, using all-fiber components, each then amplified within individual fiber amplifier channels, and subsequently are combined into a single beam using free-space optics at the output of the array. Spatial beam combining of output beams can be achieved by spatial tiling at the far field [38], or they can also be combined into a single beam by either 2-to-1 components such as polarization beam splitters (PBS) [39], or N-to-1components such as diffractive gratings [40]. Note that CPS

amplification can be implemented with a single fiber channel, particularly advantageous if 10mJ to 100mJ pulse energies could be achieved per individual channel. This system should also contain necessary electronics for achieving required coherent-control and signal monitoring feedback loops for coherent beam and pulse combining.

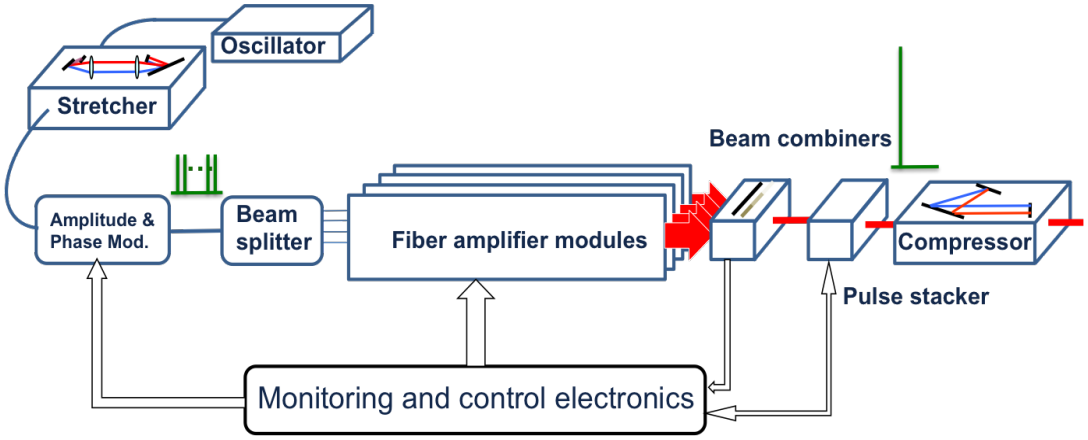

Figure 1.3: Basic architecture of coherent combined fiber laser array incorporating spatial and temporal combining techniques.

From Figure 1.2 it is quite clear that implementing multiple-channel arrays will require large-core fiber modules, which are monolithically integrated and comprise of standard, interchangeable fiber-optic components. This has been the main technological motivation for developing CCC fibers. In general, use of large core fibers in this type of applications require that a number of critical performance requirements would be met [44]:

1) Single transverse mode output from the amplifier is necessary for achieving efficient beam combining and high beam quality output of a combined beam.

2) Polarization maintenance in each parallel individual fiber amplification channel is necessary for the combining efficiency and the stability of the combined beam intensity.

3) Each parallel channel should be implemented as a compact, robust and reliable integrated (and “standardized”) module.

1.4 Chapter overview

In this dissertation, the performance of CCC fibers for high power coherent combining systems is explored theoretically and experimentally.

In Chapter II, a detailed model of fiber operation in a high power laser system is presented, which includes a thermal model, pumping and signal propagation models of a fiber laser or amplifier. Since in any effectively single-mode fiber selective suppression of higher-order modes cannot be achieved without inducing some finite leakage-loss for the fundamental mode, it is very important to understand how fiber laser or amplifier efficiency is affected by this loss. We have studied this dependence using both analytical and numerical models, presented at the end of the chapter.

Chapter III is devoted to the exploration of polarization preservation properties of CCC fibers. We first establish theoretical background by presenting general description of fiber polarisation performance using standard Poincare Sphere and coupled mode equation approaches, and review a full range of known internal and external perturbations and their effects on polarization preservation in a fiber. Further, using these theoretical tools as well as experimental characterisation, we show that in CCC fibers effect of all internal perturbations is eliminated due to rapid spinning of CCC fiber preform during fiber fabrication process, and due to the effectively single-mode nature of the fiber core. We also demonstrate that due to the large cladding size, CCC fiber sensitivity to external perturbations is significantly reduced. At the end of the chapter we consider effects of coiling-induced linear birefringence and twisting-induced circular birefringence on CCC fiber polarization properties, an important practical aspect for designing an integrated fiber system.

In Chapter IV we describe CW single-frequency fiber amplifier demonstration experiments based on 37μm CCC fibers, with SBS-free output powers reaching to nearly 600W, while preserving single polarization and single transverse mode. The TEM00 modal content from a single frequency CCC fiber amplifier is also measured in a collaboration work with a group from Hannover, Germany. This work is relevant for potential use of CCC fibers for the next generation gravitational wave detectors. Demonstration of high power single-frequency and single-transverse mode output is also relevant for using CCC fibers as parallel amplifier channels in multi-kW power CW fiber laser arrays.

In Chapter V, energy scalability of a 55um CCC fiber operating in a few-nanosecond regime is explored, achieving up to 9.1mJ and nearly 1MW of peak power with 10ns-long pulses. Energy saturation, SRS suppression as well as splice-ability of this large core CCC fiber are also studied. Results of this study are particularly relevant for designing high energy pulsed fiber amplifier systems operating in nanosecond and in ultrashort pulse ranges.

Chapter VI is devoted to exploring energy extraction scalability associated with coherent pulse stacking amplification. As a background, a recent CPS demonstration experiment is briefly described, which was performed using 55μm core Yb-doped CCC fibers. Development of the CPS method itself is not part of this thesis. However, CPS enables a new pulsed amplification regime, in which multiple ~1-ns stretched pulses are amplified in a large core amplifier. Anticipated total duration of these pulse bursts is in the range from ~100ns to >1μs, which is very unusual for pulsed fiber amplifiers. In this chapter we propose and explore a new pulsed-pumping approach, which exploits such long pulse-burst durations to increase extractable pulse energy by at least an order of magnitude compared to what is possible with 1ns-10ns short pulses. We first present an analytical method which treats the high repetition rate pulses in a burst as a

quasi-CW signal. Furthermore, we develop a more accurate quasi-analytical model, and compare the predictions of the two models. We show that when using high peak power pump pulses, achievable from Q-switched fiber lasers, one can completely overcome saturation-fluence limited energy storage, which is on the order of ~10mJ for a 55μm core Yb-doped CCC fiber, and can achieve output pulse-burst energies exceeding ~100mJ for this particular CCC core size

Chapter 2

Exploration of general large core CCC fiber laser properties

To assist building and operating fiber lasers or amplifiers, modeling and estimation of amplifier performance is very useful when choosing fiber length, pumping wavelength, and the arrangement for heat removing, etc so that performance of the system could be optimized. Generally, for majority of fiber lasers and amplifiers, the main properties pre-evaluated are power scalability and pump-signal efficiency of the system as well as heat distribution along the fiber.

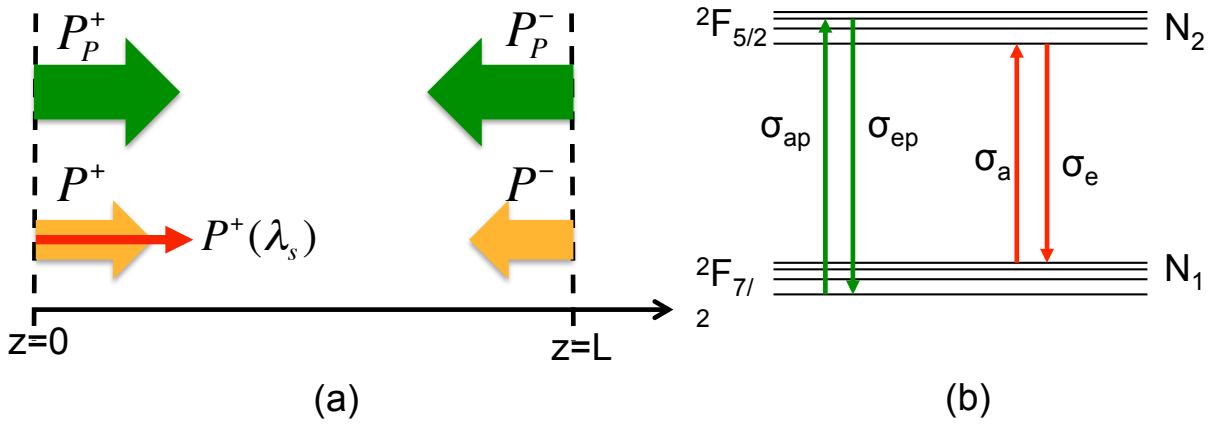

Figure 2.1: (a) Schematic illustration of fiber amplifier geometry. $P^{\pm}(z)$ and $P_p^{\pm}(z)$ are the signal and pump powers propagating in the positive and negative z direction, respectively. (b) Example of energy band diagram of a three-level system such as Yb^{3+}.

2.1 Amplification analysis for continuous-wave (CW) fiber amplifiers

As illustrated in Fig. 2.1(a), a typical fiber amplifier consists of a doped fiber with length L. To achieve high power amplification with diffraction-limited beam output, cladding-pumping

scheme has been proposed [16]. With a doped weakly guiding core which guides only one or few modes, as well as undoped cladding with larger brightness and acceptance angle, such fiber structure is capable of delivering signal beam with high beam quality whereas efficiently working with pump source with high power output but low brightness. Assuming the fiber end with seeding power $P_0^+(\lambda_s)$ launched in at z=0, all the beam propagating in the same direction as seeding signal is called forward or co-propagating while all the beam in the opposite direction is backward or counter-propagating. Pump power $P_p^+(z)$ at λ_p could be coupled into the fiber at z=0 or z=L allowing for either one of these two pumping configurations. Note that amplified spontaneous emission (ASE) produced in a pumped fiber is propagating in both directions.

Since for all the fiber amplifiers discussed in this thesis are doped with Yb^{3+}, our model is based on the transitions in Yb-doped gain medium. Fig. 2.1(b) depicts the energy band diagram for Yb-doped systems. With only one excited state manifold ($^2F_{5/2}$) and the ground-state manifold ($^2F_{7/2}$), Yb^{3+} is basically a 2-level system. However, according to the pump absorption and signal amplification to occur at different sublevels, it works as a quasi 3-level system for amplification at <1040nm and a quasi 4-level system for amplification at >1040nm [64].

The model for CW amplification is based on a set of time-independent rate equations, Eqn. 2.1-2.3 for upper-level population density $N_2(z)$, pump wave $P_p^{\pm}(z)$, signal wave $P^+(\lambda_s)$ as well as ASE [63]. Due to various emission and absorption cross-section over the broad bandwidth of ASE, the calculation is done by dividing the spectral width $\Delta\lambda$ by the spectral power density $P^{\pm}(\lambda)\ with\ \lambda \neq \lambda_s$. All the transitions described in Fig. 2.1 (b), such as pump absorption and emission, signal stimulated emission and absorption, spontaneous emission as well as scattering losses of pump and signal wave are included in these rate equations.

$$\frac{N_2(z)}{N} = \frac{\frac{[P_p^+(z)+P_p^-(z)]\sigma_{ep}\Gamma_p}{h\nu_p A}+\frac{\Gamma_s}{hcA}\int \sigma_a(\lambda)[P^+(z,\lambda)+P^-(z,\lambda)]\lambda d\lambda}{\frac{[P_p^+(z)+P_p^-(z)](\sigma_{ep}+\sigma_{ap})\Gamma_p}{h\nu_p A}+\frac{1}{\tau}+\frac{\Gamma_s}{hcA}\int [\sigma_a(\lambda)+\sigma_e(\lambda)][P^+(z,\lambda)+P^-(z,\lambda)]\lambda d\lambda} \quad (2.1)$$

$$\pm {dP_p^{\pm}(z)}\Big/_{dz} = -\Gamma_p\{\sigma_{ap}N - (\sigma_{ap}+\sigma_{ep})N_2(z)\}P_p^{\pm}(z) - \alpha(z,\lambda_p)P_p^{\pm}(z) \quad (2.2)$$

$$\pm {dP^{\pm}(z,\lambda)}/_{dz} = \Gamma_S\{[\sigma_a(\lambda)+\sigma_e(\lambda)]N_2(z) - \sigma_a(\lambda)N\}P^{\pm}(z,\lambda) + \frac{2hc^2}{\lambda^3}\Gamma_s\sigma_e(\lambda)N_2(z) - \alpha(z,\lambda)P^{\pm}(z,\lambda) \quad (2.3)$$

where h is the Plank constant, c is light speed in vacuum and N is the dopant concentration (per unit length). τ is the upper-level lifetime. A is size of core area. Pump power filling factor Γ_p is the ratio of core and cladding area. Similarly, signal power filling factor Γ_s is given by the ratio of core and mode area. σ_{ep}, σ_{ap} are respectively emission and absorption cross-sections of pump wave at ν_p, whereas $\sigma_a(\lambda)\ and\ \sigma_e(\lambda)$ are the emission and absorption cross-section of wave propagating along the core. $\alpha(z,\lambda)$ represents the scattering loss coefficient for pump or signal wave.

The calculation always starts from the input pump power end for both co-pumping and counter-pumping scheme with all the powers propagating towards the other end, using Runge-Kutta integrations. Estimation for output ASE and signal wave that propagate along the opposite direction is made at the beginning and further refined in an iterative procedure until the calculated input power for ASE and signal power equals the given value.

Fig. 2.2 shows an example of simulation results of a counter-pumped fiber amplifier based on a 3m piece of 37μm core, 250μm cladding CCC fiber. Parameters used in the computation are listed in Table 2.1. Values for emission and absorption cross-section of Yb^{3+} in a germanosilicate glass were obtained by spectroscopic measurements by Paschotta et al [64]. Note that in the calculation results presented here, the efficiency of amplification is close to 90%, which is purely due to the quantum defect. However, in real system, additional factors such as

non-radiative decay from the upper level, the efficiency of Yb-doped fiber lasers and amplifiers does not exceed 80% in practice.

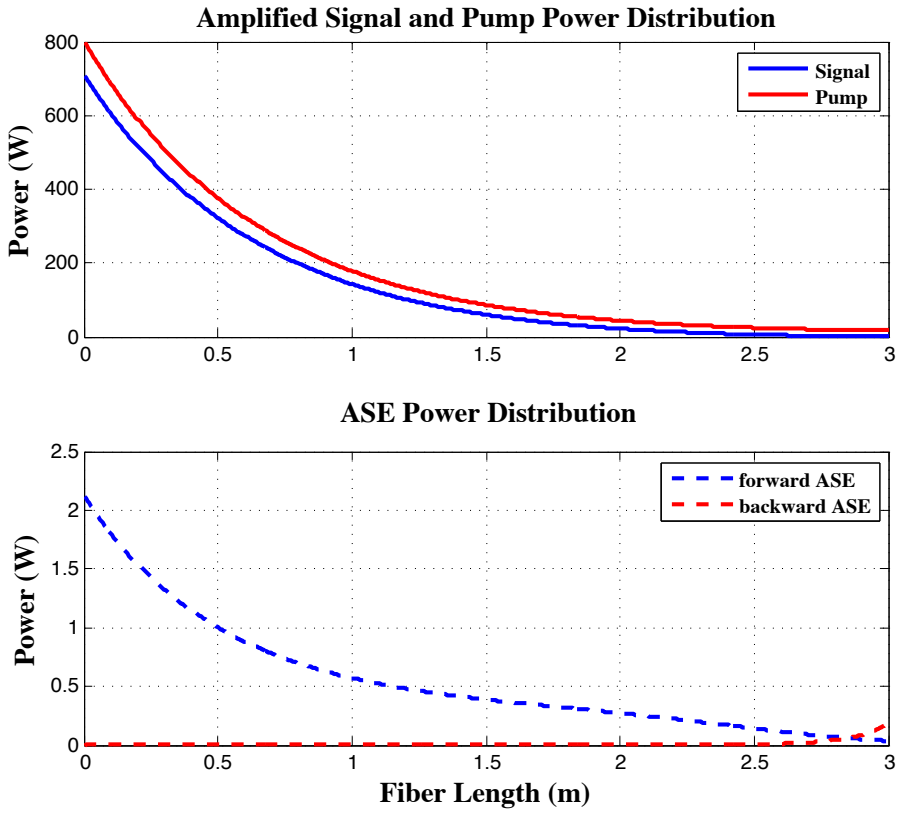

Figure 2.2: Power distribution along the fiber with 1W seeding power at 1064nm and 800W pumping power at 976nm.

Table 2.1 Parameters used in computation

Parameter	Value
λ_p	976nm
λ_s	1064nm
τ	0.8ms
σ_{ep}	$2.5\times10^{-24}m^2$
σ_{ap}	$2.5\times10^{-24}m^2$
$\sigma_a(\lambda_s)$	0
$\sigma_e(\lambda_s)$	$0.3\times10^{-24}m^2$
$\sigma_a(\lambda)$	see ref. [2]
$\sigma_e(\lambda)$	see ref. [2]
A	1369 μm^2
N	3.787×10^{25} m^{-3}
Γ_s	1

Γ_s	0.0219
α	3×10^{-3} m^{-1}

2.2 Analysis of the effect of fundamental-mode leakage-loss on amplifier efficiency

As discussed in section 1.4, for achieving high power output with near diffraction-limited beam from a fiber amplifier, it is advantageous to use a specially designed effectively-single-mode fiber, in which HOM propagation is "blocked" by inducing HOM leakage from the core to the cladding. However, with significant HOMs leakage-loss introduced, some residual leakage-loss for fundamental mode also appears in these fibers. In this section the effect of this fundamental mode loss on amplifier for laser efficiency is investigated.

Firstly, to explicitly understand the influence of core signal loss on system efficiency, an analytical solution for slope efficiencies of core and total power was derived for a fiber laser system. The model for fiber laser system is shown in Fig. 2.3, which consists of a piece of fiber with length of L and two reflection mirrors with reflectivity R_1 and R_2 respectively.

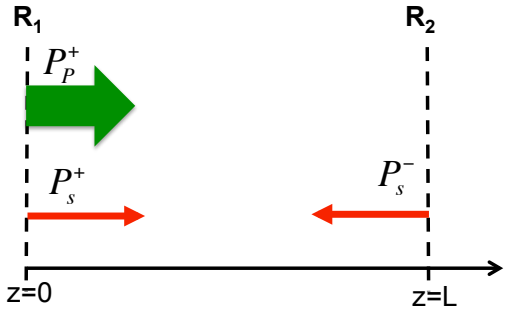

Figure 2.3: Illustration of fiber laser model.

The rate equations for lasing are as follows:

$$\frac{dN_2}{dt} = -\frac{N_2}{\tau} + \frac{(\sigma_{ap}N_1 - \sigma_{ep}N_2)\Gamma_p P_p}{h\nu_p A} - \frac{(\sigma_e N_2 - \sigma_a N_1)\Gamma_s (P_S^+ + P_S^-)}{h\nu_s A} \tag{2.4}$$

$$\frac{dP_p}{dz} = -(\sigma_{ap}N_1 - \sigma_{ep}N_2)\Gamma_p P_p \tag{2.5}$$

$$\pm\frac{dP_S^\pm}{dz} = [(\sigma_e + \sigma_a)\Gamma_s N_2 - \sigma_a \Gamma_s N_{tot} - \alpha]P_S^\pm \tag{2.6}$$

where N1, N2 are longitudinal ion populations density at ground level and upper level respectively. A is fiber core area while $\Gamma_p = A_{core}/A_{clad}$ is pump power filling factor and Γ_s is the ratio of mode area to core area. ν_p, ν_s are pump and signal frequency, h is Plank constant, and τ is upper level lifetime. α represents scattering loss coefficient for signal wave.

The steady state solution for upper level population ratio $n_2(z) = N_2(z)/N_{tot}$ is then:

$$n_2 = -\frac{\tau}{AN_{tot}}\left[\frac{dP_p}{h\nu_p dz} + \frac{1}{h\nu_s}\left(\frac{dP_s^+}{dz} + \alpha P_s^+\right) - \frac{1}{h\nu_s}\left(\frac{dP_s^-}{dz} - \alpha P_s^-\right)\right] \tag{2.7}$$

With $N_1 = (1 - n_2)N_{tot}$ and (2.7), Eqn. (2.5) could be solved as:

$$P_p(z) = P_p(0)\exp\left[-\sigma_{ap}\Gamma_p N_{tot} z + \frac{\tau(\sigma_{ep}+\sigma_{ap})\Gamma_p}{A}\left(\frac{P_{pabs}(z)}{h\nu_p} - \frac{P_{tot}^+(z)+P_{tot}^-(z)}{h\nu_s}\right)\right] \tag{2.8}$$

where

$$P_{pabs}(z) = P_p(0) - P_p(z) \tag{2.9}$$

$$P_{tot}^{\pm}(z) = \pm\left(P_s^{\pm}(z) - P_s^{\pm}(0)\right) + P_{sloss}^{\pm}(z) \tag{2.10}$$

$$P_{sloss}^{\pm}(z) = \int_0^z \alpha P_s^{\pm}(\xi)d\xi \tag{2.11}$$

Note that $P_{sloss}^-(z)$ is not the power loss to cladding at z position, it is actually the total power in cladding subtract the loss accumulated from z to 0. Similar definition applies for $P_{tot}^-(z)$. And $\frac{P_{pabs}(z)}{h\nu_p}$ and $\frac{P_{tot}^+(z)+P_{tot}^-(z)}{h\nu_s}$ are indeed photon flux of pump absorption and total signal amplification respectively.

In a similar fashion, we obtain:

$$P_s^+(z) = P_s^+(0)\exp\left[-(\sigma_a\Gamma_s N_{tot} + \alpha)z + \frac{\tau(\sigma_e+\sigma_a)\Gamma_s}{A}\left(\frac{P_{pabs}(z)}{h\nu_p} - \frac{P_{tot}^+(z)+P_{tot}^-(z)}{h\nu_s}\right)\right] \tag{2.12}$$

$$P_s^-(z) = P_s^-(0)\exp\left[(\sigma_a\Gamma_s N_{tot} + \alpha)z - \frac{\tau(\sigma_e+\sigma_a)\Gamma_s}{A}\left(\frac{P_{pabs}(z)}{h\nu_p} - \frac{P_{tot}^+(z)+P_{tot}^-(z)}{h\nu_s}\right)\right] \tag{2.13}$$

For a fiber laser, the boundary condition is given by:

$$\mathrm{P_s^-}(L) = R_2 \cdot \mathrm{P_s^+}(L)\ and\ \mathrm{P_s^+}(0) = R_1 \cdot \mathrm{P_s^-}(0) \tag{2.14}$$

Using Eqn. (2.13-14) we can further get:

$$\frac{\tau(\sigma_e+\sigma_a)\Gamma_s}{A}\left(\frac{P_{pabs}(L)}{h\nu_p} - \frac{P_{tot}^+(L)+P_{tot}^-(L)}{h\nu_s}\right) = (\sigma_a\Gamma_s N_{tot} + \alpha)L - \frac{1}{2}\ln(R_1R_2) \tag{2.15}$$

Plug (2.15) into (2.8, 2.12 and 2.13),

$$\mathrm{P_p}(L) = \mathrm{P_p}(0)\exp\left[-\sigma_{\mathrm{ap}}\Gamma_{\mathrm{p}}\mathrm{N_{tot}}L + \frac{(\sigma_{\mathrm{ep}}+\sigma_{\mathrm{ap}})\Gamma_{\mathrm{p}}}{(\sigma_e+\sigma_a)\Gamma_s}\left((\sigma_a\Gamma_s N_{tot} + \alpha)L - \frac{1}{2}\ln(R_1R_2)\right)\right] \tag{2.16}$$

$$\mathrm{P_s^+}(L) = \frac{\mathrm{P_s^+}(0)}{\sqrt{R_1R_2}} \tag{2.17}$$

$$\mathrm{P_s^-}(0) = \frac{\mathrm{P_s^-}(L)}{\sqrt{R_1R_2}} \tag{2.18}$$

And the absorbed pump power can be expressed as

$$\mathrm{P}_{pabs}(L) = \mathrm{P_p}(0)\{1 - \exp\left[-\sigma_{\mathrm{ap}}\Gamma_{\mathrm{p}}\mathrm{N_{tot}}L + \frac{(\sigma_{\mathrm{ep}}+\sigma_{\mathrm{ap}})\Gamma_{\mathrm{p}}}{(\sigma_e+\sigma_a)\Gamma_s}\left((\sigma_a\Gamma_s N_{tot} + \alpha)L - \frac{1}{2}\ln(R_1R_2)\right)\right]\} \tag{2.19}$$

Using Eqn. (2.11-13), one can get an expression for the total power lost into cladding $\mathrm{P}_{sloss}^{\pm}$.

$$\mathrm{P}_{sloss}^{\pm} = \alpha\mathrm{P_s^{\pm}}(0)\int_0^L \exp\left[\mp(\sigma_a\Gamma_s N_{tot} + \alpha)z \pm \frac{\tau(\sigma_e+\sigma_a)\Gamma_s}{A}\left(\frac{P_{pabs}(z)}{h\nu_p} - \frac{P_{tot}^+(z)+P_{tot}^-(z)}{h\nu_s}\right)\right]dz \tag{2.20}$$

Since $\frac{P_{pabs}(z)}{h\nu_p} - \frac{P_{tot}^+(z)+P_{tot}^-(z)}{h\nu_s}$ is indeed the difference between integral of photon flux for pump absorption and signal amplification from 0 to z, the maximum value of this term is at fiber end z=L, i.e. $\frac{P_{pabs}(L)}{h\nu_p} - \frac{P_{tot}^+(L)+P_{tot}^-(L)}{h\nu_s}$. From (2.15) we can get

$$\Delta\mathrm{N_{max}} = \frac{[(\sigma_a\Gamma_s N_{tot}+\alpha)L - \frac{1}{2}\ln(R_1R_2)]A}{\tau(\sigma_e+\sigma_a)\Gamma_s} \tag{2.21}$$

This is also the threshold pump power photon flux to start the lasing oscillation. And one reasonable assumption is that this threshold pump power photon flux is homogeneously distributed along the fiber length, hence one can get:

$$\Delta N(z) = \frac{\Delta N_{max} \cdot z}{L} \tag{2.22}$$

Using Eqn. (2.20) and (2.22), $P_{sloss}^{\pm}$ can be further calculated as

$$P_{sloss}^{+} = \beta^{+} \cdot P_s^{+}(0) \tag{2.23}$$

where $\beta^{+} = \frac{(\sqrt{R_1 R_2}-1)}{\sqrt{R_1 R_2}\ln(R_1 R_2)} 2\alpha L$.

Similarly, one can also get:

$$P_{sloss}^{-} = \beta^{-} \cdot P_s^{-}(0) \tag{2.24}$$

where $\beta^{-} = \frac{(\sqrt{R_1 R_2}-1)}{\ln(R_1 R_2)} 2\alpha L$. From the expression of β^{+} and β^{-}, it is clearly shown that the power loss from the core signal is strongly dependent on the total loss rather then the loss ratio per unit length.

Hence, the total amplified power from 0 to L is given by

$$P_{tot}^{+}(z) + P_{tot}^{-}(z) = \chi \cdot P_s^{+}(0) \tag{2.25}$$

where $\chi = \frac{(1-\sqrt{R_1 R_2})(\sqrt{R_1}+\sqrt{R_2})}{R_1\sqrt{R_2}}(1 - \frac{2\alpha L}{\ln(R_1 R_2)})$.

With Eqn. (2.15) and (2.25) we can get an expression for $P_s^{+}(0)$ with dependence on $P_{pabs}(L)$ as follows:

$$P_s^{+}(0) = \frac{h\nu_s}{\chi}\{\frac{P_{pabs}(L)}{h\nu_p} - \frac{\left[(\sigma_a \Gamma_s N_{tot}+\alpha)L - \frac{1}{2}\ln(R_1 R_2)\right]A}{\tau(\sigma_e+\sigma_a)\Gamma_s}\} \tag{2.26}$$

For co-propagating laser output, i.e. $R_2 \ll 1$ and $R_1 \approx 1$, the output power in core is:

$$P_{s,out}^{+} = P_s^{+}(L)(1-R_2) = \frac{(1-R_2)}{\sqrt{R_1R_2}} P_s^{+}(0) \tag{2.27}$$

With (2.26) the slope efficiency of laser signal in core is given by:

$$\eta_{s,co} = \frac{dP_{s,out}^{+}}{dP_{\text{pabs}}(L)} = \frac{\nu_s}{\nu_p} \cdot \frac{(1-R_2)}{\chi\sqrt{R_1R_2}} \tag{2.28}$$

The total power output is then can also be calculated by:

$$P_{tot,out}^{+} = [\frac{1}{\sqrt{R_1R_2}} + \beta^{+} + \beta^{-}](1-R_2)P_s^{+}(0) \tag{2.29}$$

Similarly as the calculation for core signal slope efficiency, one can also get expression for total power slope efficiency as follows:

$$\eta_{tot,co} = \frac{dP_{tot,out}^{+}}{dP_{\text{pabs}}(L)} = [1 + \frac{(R_1R_2-1)}{\ln(R_1R_2)} 2\alpha L]\eta_{s,co} \tag{2.30}$$

For counter-propagating laser output, i.e. $R_1 \ll 1$ and $R_2 \approx 1$, the expressions for slope efficiencies of core signal $\eta_{s,ct}$ and that of total power $\eta_{tot,ct}$ could be derived following the same steps:

$$\eta_{s,ct} = \frac{dP_{s,out}^{-}}{dP_{\text{pabs}}(L)} = \frac{\nu_s}{\nu_p} \cdot \frac{(1-R_1)}{\chi R_1} \tag{2.31}$$

$$\eta_{tot,ct} = \frac{dP_{tot,out}^{+}}{dP_{\text{pabs}}(L)} = [1 + \frac{(R_1R_2-1)}{\ln(R_1R_2)} 2\alpha L]\eta_{s,ct} \tag{2.32}$$

From the relations shown in (2.28 and 2.30-32), the dependence of slope efficiencies of core signal and total power on total loss in the fiber rather than the loss ration per unit length both for co-pumping and counter-pumping schemes. Moreover, for usual laser system, reflectivity of one of the mirror would be close to one, and the following expression is true for $\alpha L \gg |\ln(R_1R_2)|$.

$$\frac{1+\frac{(R_1R_2-1)}{\ln(R_1R_2)}2\alpha L}{1-\frac{2\alpha L}{\ln(R_1R_2)}} = 1 - R \tag{2.33}$$

where R is the reflectivity of pick up value. This means the slope efficiency of total power would remain the same for small total loss, and then with total loss increases, it degrades slowly to (1-R) of the original value with no loss in core.

In Fig. 2.4 simulation results of relation between slope efficiencies and core signal loss ratio both from numerical and analytical model are depicted and compared for 3m long 37μm core, 250μm cladding CCC fiber with parameters listed in Table 2.1. The calculations were for counter-propagating laser output with pick-up mirror reflectivity of 4%. The red curves are analytical solution while the blue ones are from numerical modeling. The total slope efficiency is illustrated in solid lines while the core signal efficiency is with dashed lines. The numerical calculation was carried out with lasing wavelength at 1064nm and pump power of 100W with wavelength at 976nm and 966nm respectively. The disagreement between numerical and analytical modeling for 976nm at loss ratio larger than 5dB/m is because with such high loss, the lasing condition is not satisfied and no lasing oscillation started. Therefore, the assumption made with Eqn. (2.22) is not valid. However, one should also keep in mind that in real system, fundamental mode loss in fiber is usually no more than 3dB/m. And for leakage loss smaller than 3dB/m, we have excellent agreement between the analytical expressions and exact solutions.

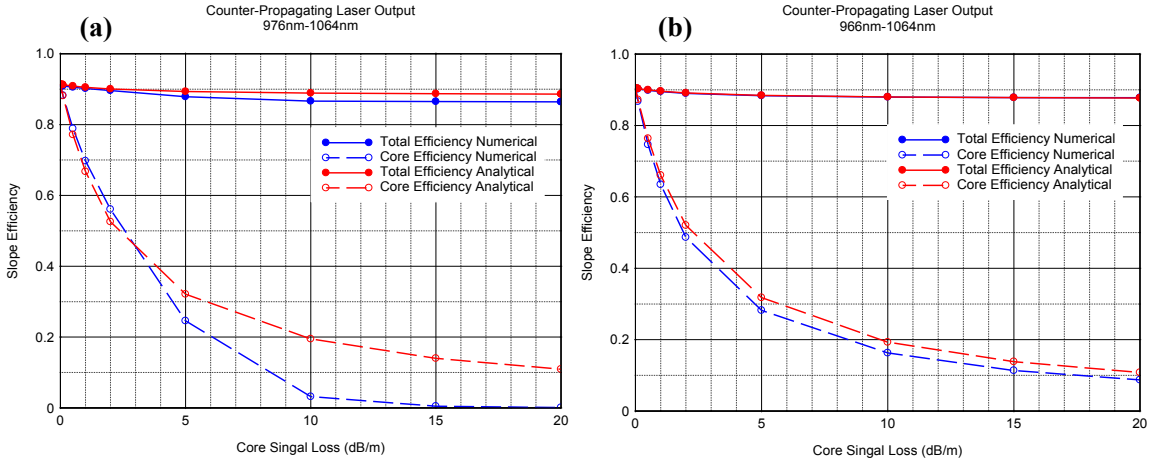

Figure 2.4: Comparison of analytical solution and numerical calculation for the slope efficiency dependence on fundamental mode loss in core. The solid lines are total power efficiency while the dashed lines represent core signal efficiency. The simulation results following numerical models are in blue while the ones following analytical solution are in red. (a) with pumping wavelength at 976nm. (b) with pump wavelength at 966nm.

Since for fiber amplifier model, it only has initial boundary condition known, it is hence not possible to get an explicit solution for the efficiency and loss rate relation. But one can still study the effect of fundamental mode leakage loss on amplifier efficiency with numerical calculation introduced in the previous section. Furthermore, fiber design criteria could also be achieved based on such simulation. The following examples were calculated with the same 3m long 37μm core, 250μm cladding CCC fiber as in the previous section. And effects of fundamental mode loss for both co-pumping and counter-pumping scheme were compared and further investigation on impact of signal loss on amplifier efficiency was also done. To simplify the calculation, strong seeding for the amplifier is assumed and hence the power of the ASE is negligible in the model.

First, power amplification with 0dB/m and 5dB/m loss of fundamental mode in a 3m long piece of fiber with 9dB/m pump absorption at 975nm for both co-pumping and counter-pumping schemes are compared, as shown in the Fig. 2.5. The system is seeded with 3W at 1064nm and pumped with 100W at 975nm. For counter-pumping configuration, the signal power monotonically increases along the fiber to 90W at the output when fundamental mode has no

loss, and to 45W when it possesses a 5dB/m leakage. For the co-pumping configuration, signal output power reaches also 90W when signal is lossless, which is the same as in the counter-pumping case. However, when fundamental mode experiences 5dB/m leakage, propagating signal power first monotonically increases until it reaches 34.7W at 1.3m from the input, and then monotonically decreases with further propagation reaching 11.5W at the output. This happens because co-propagating pump decreases along the fiber, and at some point signal gain becomes lower than signal leakage. If to shorten fiber amplifier to the length of 1.3m where signal reaches its maximum, then considerable residual pump power would be transmitted, indicating that efficiency of the amplifier is far from its optimum. This comparison shows clearly that to have efficient power extraction, the counter-pumping scheme is more immune to the signal loss and less sensitive to the fiber length than the co-pumping case.

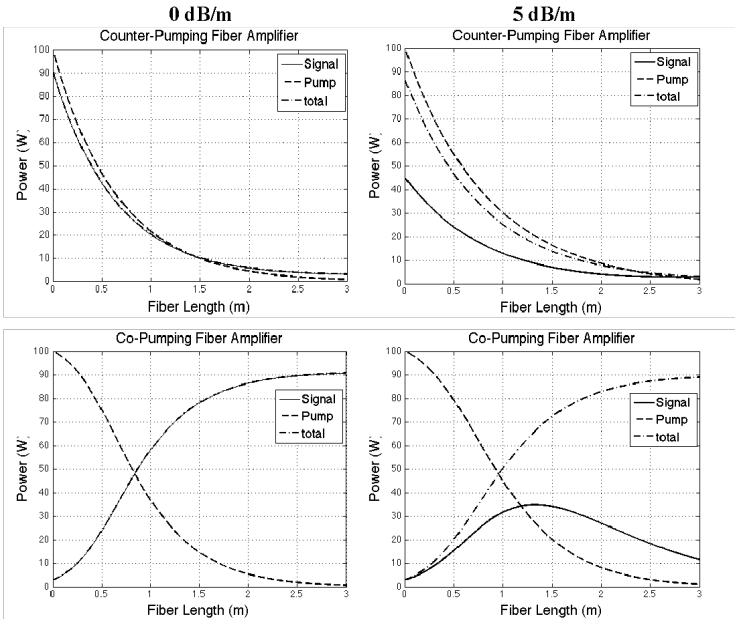

Figure 2.5: Power distribution along the fiber under both counter-pumping and co-pumping configuration with assumption of fundamental mode loss in core as 0dB/m and 5dB/m respectively. The dashed curve is the pump power distribution. The solid curve represents signal power in core while the dash-dot curve is the total signal power distribution

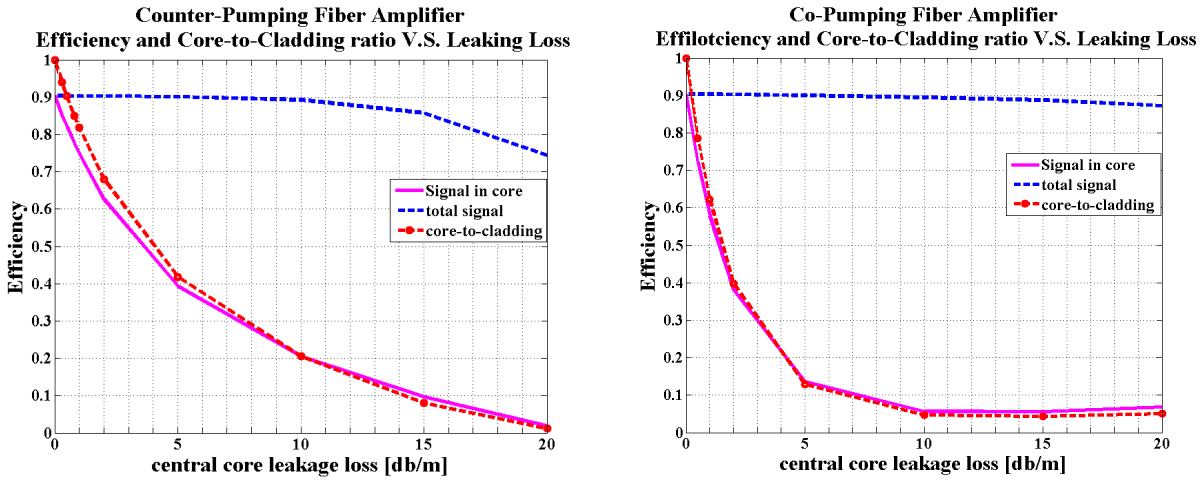

Figure 2.6: Slope efficiencies of signal in core and total amplified power as well as core-to-total power ratio versus fundamental mode loss in core. The dashed curve is the slope efficiency of total power and the solid line is that of the signal power in core. The dashed curve with circles represents the core-to-total power ratio.

Impact of loss of core signal on amplifier efficiency and core-to-total power ratio is further explored for both pumping schemes with the same system parameters as in previous simulation. The slope efficiencies of core signal and total signal power versus absorbed pump power as well as core-to-total power ratio were calculated for various core signal losses per unit length range from 0dB to 20dB/m and the simulation results are depicted in Fig. 2.6. Both counter-pumping and co-pumping cases were computed with 3W seeding power at 1064nm and 100W pump power at 976nm. For both pumping configurations, the slope efficiency of total amplified power experiences negligibly small degradation, decreasing from 90% to 87% when fundamental mode leakage loss increases to 20dB/m, while the in-core signal efficiency degrades significantly with increasing fundamental mode loss. The degradation of core signal slope efficiency in co-pumping amplifier with leakage loss is more pronounced than that in counter-pumping systems. This behavior is due to the less efficient pump power conversion when the signal propagates away from the pump end in co-pumping system. It is confirmed again that counter-pumping configuration is more suitable for optimizing conversion efficiency of power

amplification. It is worth noting again that in practical system, the fundamental mode loss in fiber core is usually much less than 3dB/m, with a typical design requirement being less than 1dB/m.

The fundamental mode leakage from core to cladding not only degrades the efficiency of an amplifier or a laser system, but it also affects output beam quality due to power present in the cladding. Therefore, an important characteristic of an effectively single-mode fiber laser or amplifier is the core-to-cladding power ratio of the output beam, defined as the ratio between the in-core signal power to the total signal power from the fiber. If to require that a beam with acceptable quality should have core-to-cladding power ratio higher than 90%, then according to the simulation results from Fig. 2.6 for the 37μm core, 250μm cladding CCC fiber, less than 0.5dB/m fundamental mode leakage loss is allowed.

Fiber length is a critical parameter in determining the performance of fiber amplifiers and lasers. On one hand, the longer fiber length facilitates thermal management; on the other hand, increasing length usually reduces the threshold for nonlinear effects, which are detrimental to the power scalability of the system. Slope efficiencies of core signal and total amplified power versus various fiber lengths for both counter-pumping and Co-pumping systems are shown in Fig. 2.7. The fundamental mode loss ratio α and ion concentration N were adjusted for different fiber lengths to keep the total loss and pump absorption value constant. From Fig. 2.7 one can conclude that the slope efficiency is dependent on the total loss of the system but not the loss per unit length, which is consistent with the analytical solution for fiber lasers. As a result, higher doping concentration for the fiber is preferred if the fundamental mode loss ratio is constant so that fiber length in need is shortened which in turn will reduce the over all loss in amplification as well as increase the slope efficiency.

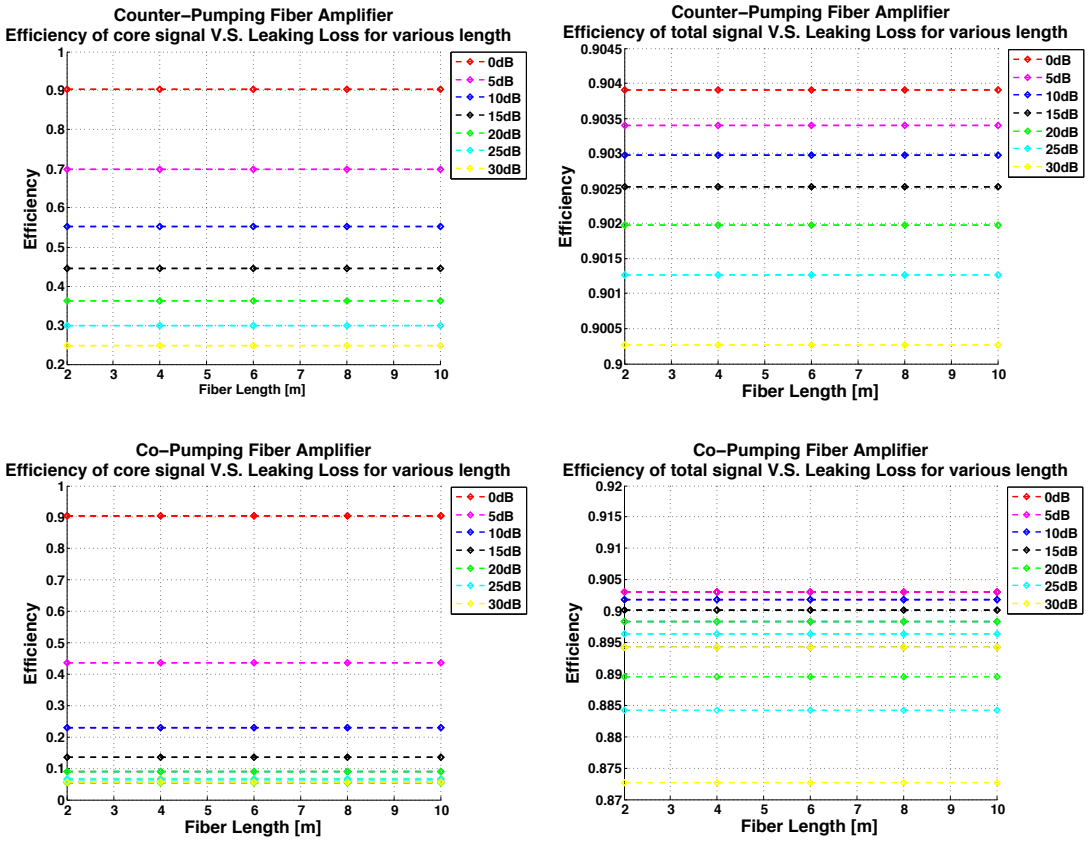

Figure 2.7: Slope efficiency dependence on fiber length with total fundamental mode loss fixed.

A comparison of experimental measurements with the numerical calculation of both amplifier and laser is depicted in Fig. 2.8. Core-to-cladding power ratio from the same 2.5m long 55μm core Yb-doped CCC fiber was measured under various tests. Firstly, both ends of the fiber were straight cleaved and pumped with up to 40W. The core-to-cladding ratio was measured with output beam from both ends, which was 84% for the counter propagating signal and 52% for the co-propagating signal. And then the core-to-cladding ratio of 62% was measured from lasing output with implementing a dielectric filter at the pump output end. Both ends of the fiber were then endcaped and polished to 12^{o}. Seeding with 10mW and 600mW respectively, the core-to-cladding power ratios of amplified output were measured with counter-pumping to 50W. For 10mW seeding, core-to-cladding ratio was about 71%, and for 600mW seeding, that was around

62%. As shown in Fig. 2.8, most of these measured values correspond to a calculated leakage loss rate of approximately 2dB/m.

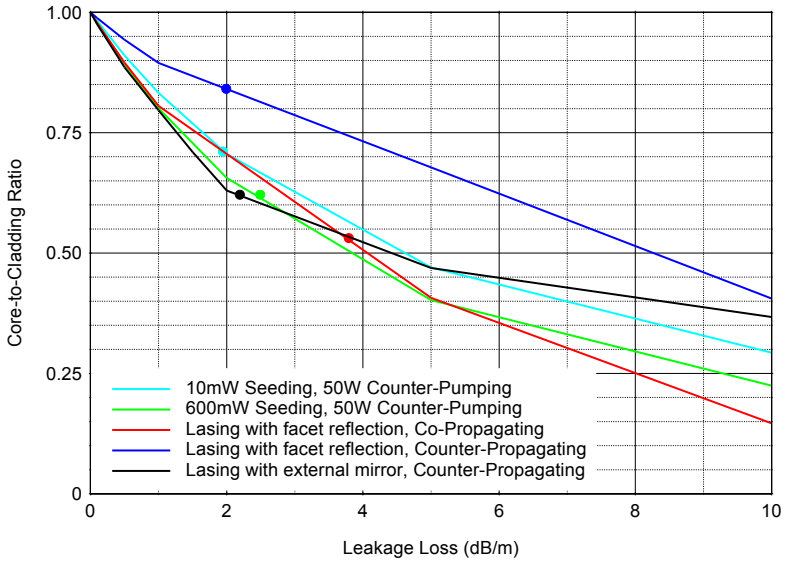

Figure 2.8: Comparison of experimental measuerement of core-to-cladding ratio from fiber amplifier and laser to the simulated result. The sollid lines are simulation results. The dots are the measured value.

2.3 Thermal analysis for heat distribution along fiber during amplification

Heat is generated in the core of fibers due to intrinsic quantum defect and non-radiative decay [65]. The intrinsic quantum defect is the energy difference between pump and lasing photons, which is lost during the non-radiative transition from pump absorption band to the lasing level. It is hence given by:

$$\eta_q = 1 - {\lambda_p}/{\lambda_s} \tag{2.34}$$

Ideally, the efficiency of the system is the quantum efficiency defined only be λ_p / λ_s. However, in practice, the system efficiency is lower than this quantum efficiency since there is non-radiative decay from the lasing level due to multi-photon decay and ion-ion energy transfer such as concentration quenching, diffusion and cross relaxation. As illustrated in Fig. 2.9,

for general double-clad fibers, the heat is then transported from core to the surface of the fiber by thermal conduction in silica and polymer and further removed by various cooling techniques, such as natural convection and radiation to ambient air and forced convection by fan or water-cooled metal mount.

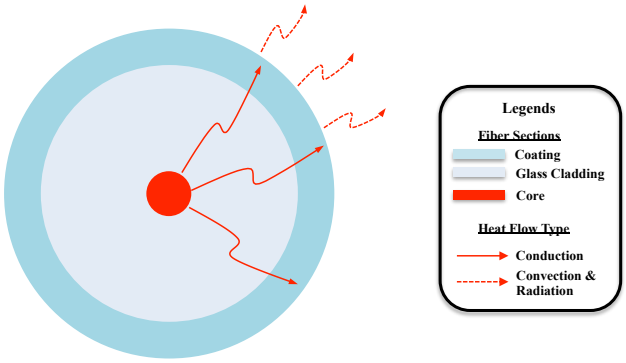

Figure 2.9: Illustration of heat dissipation in cross section of double clad fibers. The solid line represents conductive heat transmission, and the dashed lines are dissipation by convection and radiation

With heat generation and dissipation in fibers, a temperature gradient ΔT would be formed across the fiber, i.e. from the fiber core to the coating. This temperature gradient would then affect the fiber laser or amplifier performance in the following ways: 1) thermal stress induced fracture of fiber, 2) polymer coating degradation, 3) beam distortion by thermal induced refractive index change, 4) decrease in quantum efficiency due to the temperature dependent non-radiative decay rate [65]. Although one of the advantages of fiber lasers is good heat dissipation due to large surface-to-volume ratio of a fiber, thermal effects still occur when very high powers are reached. As a result, analysis of temperature distribution across and along the fiber is a prerequisite for the design of cooling arrangement as well as the evaluation of power scalability of the system. The design criterion for the thermal management is to keep the temperature of fiber core 165^{o}C, which corresponds to a drop of 6% of quantum efficiency [65]

while the polymer coating temperature always has to be below 60°C to avoid degradation of the coating material.

To simplify the calculation of temperature distribution across the fiber without considering its influence on beam distortion, one could assume the profile of the beam propagates along the fiber is flattop with power uniformly distributed across the symmetric fiber core. Heat dissipated per unit volume Q(z) is hence given by:

$$\begin{cases} Q(z) = (1-\eta)\frac{R_P(z)P_p(z)}{\pi r_o^2}, 0 < r < r_0 \\ Q(z) = 0, \qquad\qquad r_0 < \ r \end{cases} \tag{2.35}$$

where η is the efficiency of amplifier, r_0 is the radius of fiber core and $P_p(z)$ is the pump power distribution at longitudinal position z of the fiber with $R_P(z)$ as the pump rate at that point. With the heat source specified, temperature distribution could be derived by solving Fourier equation in cylindrical coordinates over the fiber volume:

$$\kappa\left\{T(r) + \frac{T'(r)}{r}\right\} + Q = 0 \tag{2.36}$$

where κ is the temperature conductivity of fiber material for different sections.

Boundary condition at the center of fiber core (r=0), interface between different fiber materials ($r=r_b$) and the outer surface of coating ($r=r_{coat}$) are as follows [68]:

$$\left.\frac{\partial T(r)}{\partial r}\right|_{r=0} = 0, \tag{2.37}$$

$$\partial T(r)|_{r=r_{b-}} = \partial T(r)|_{r=r_{b+}} \quad \left.\frac{\partial T(r)}{\partial r}\right|_{r=r_{b-}} = \left.\frac{\partial T(r)}{\partial r}\right|_{r=r_{b+}}, \tag{2.38}$$

$$\left.\frac{\partial T(r)}{\partial r}\right|_{r=r_{coat}} = \frac{h}{\kappa_{coat}}[T_0 - T(r_{coat})] + \frac{\delta\epsilon}{\kappa_{coat}}[T_0^4 - T^4(r_{coat})], \tag{2.39}$$

where $h = C_1(\frac{\Delta T}{2r_{coat}})^{1/4}$ is the surface heat transfer coefficient, where C_1 is the coefficient of heat convection with reservoir, which varies due to different cooling method utilized. T_0 is the

ambient temperature. δ is Stefan Boltzmann constant and ε is surface emissivity. The first term on right-hand side of Eqn. 2.39 represents heat convection to the external reservoir, while the second term is for radiative heat dissipation.

For double-clad fibers, the solution of (2.36) is:

$$r_{clad} < r \leq r_{coat}, \quad T(r) = T(r_{coat}) + \frac{Q(z)r_o^2}{2\kappa_{coat}} \ln\left(\frac{r_{coat}}{r}\right) \tag{2.40}$$

$$r_o < r \leq r_{clad}, \quad T(r) = T(r_{clad+}) + \frac{Q(z)r_o^2}{2\kappa_{clad}} \ln\left(\frac{r_{clad}}{r}\right) \tag{2.41}$$

$$0 \leq r \leq r_o, \quad T(r) = T(r_{o+}) + \frac{Q(z)r_o^2}{4\kappa_{core}} \left[1 - \left(\frac{r}{r_o}\right)^2\right] \tag{2.42}$$

where r_o, r_{clad} and r_{coat} are radii of fiber core, cladding and coating respectively. κ_{coat}, κ_{clad} and κ_{core} are thermal conductivity for theses different fiber sections.

Table 2.2 Parameters for temperature distribution calculation

Parameter	Value
C_{air}	1.38 W/($m^{1.75}K^{1.25}$)
C_{water}	105 W/($m^{1.75}K^{1.25}$)
κ_{coat}	0.23 W/(mK)
κ_{clad}	1.37 W/(mK)
κ_{core}	1.37 W/(mK)
δ	5.67×10^{-8} W/(m^2K^4)
ε	0.95

Values for parameters commonly used in calculation for temperature distribution across the fiber is listed in Table 2.2.

Fig. 2.10 shows an example of simulation results for power and temperature distribution of a piece of fiber during high power operation. The fiber used in this calculation is a piece of 2.5m LMA fiber with 37μm core, 400μm cladding and 550μm coating. Seeding power for the amplifier is assumed to be 5W at 1064nm while the pump power is 150W at 976nm and follows a counter-propagating scheme.

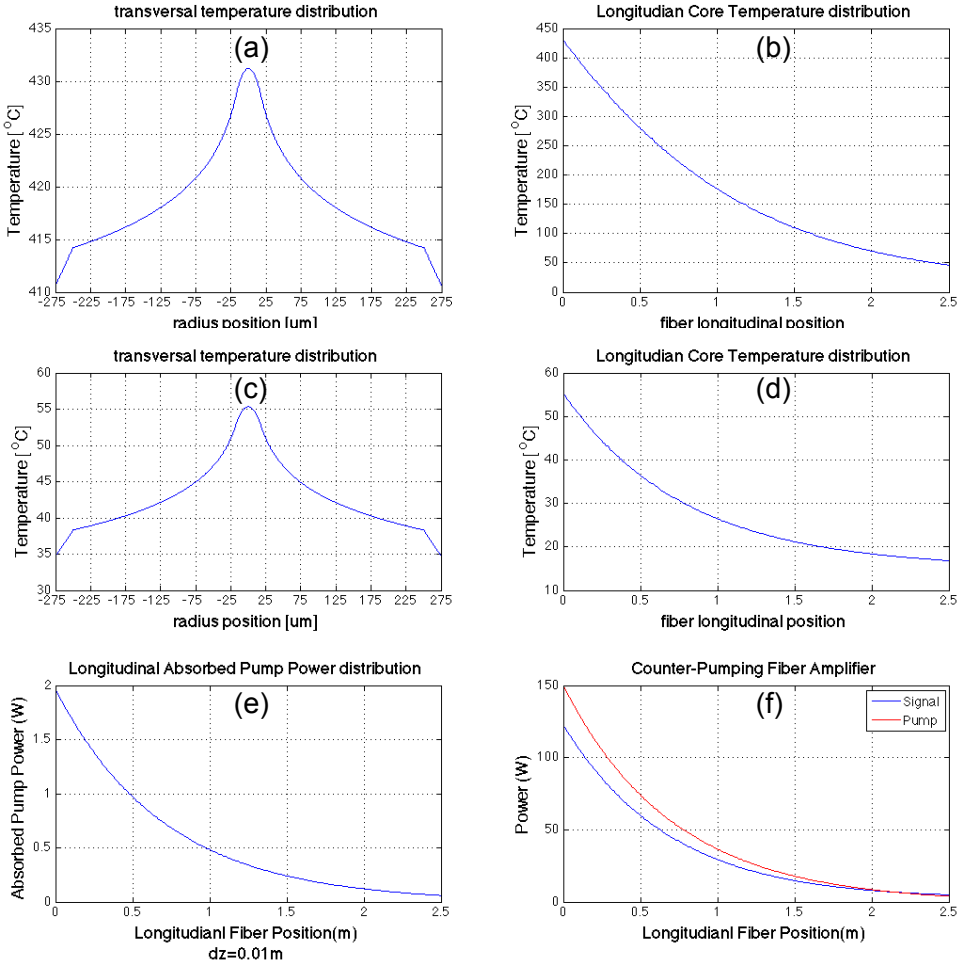

Figure 2.10: Example of simulation results for power and temperature distribution of a 2.5m double-clad fiber with 37μm core and 250μm cladding in counter-pumped high power operation. (a-b) Transversal and longitudinal core temperature distribution with passive air convection at fiber surface. (c-d) Transversal and longitudinal core temperature distribution with passive water convection at fiber surface. (e-f) Longitudinal distribution of absorbed power, pump power and signal power along the fiber.

Plots (a) and (c) are transversal temperature distribution at the pump end of the fiber while plots (b) and (d) are longitudinal core temperature distribution along the fiber. Passive air convection at surface of the fiber is assumed for simulation done with plots (a) and (b) and passive water convection is considered for that done with plots (c) and (d). Plots (e) and (f) shows the longitudinal power distribution for absorbed and total pump power as well as signal power. Close to 400°C difference for temperature distribution within and along the fiber between these two cooling methods shows clearly the importance of a proper cooling scheme for high power fiber laser systems.

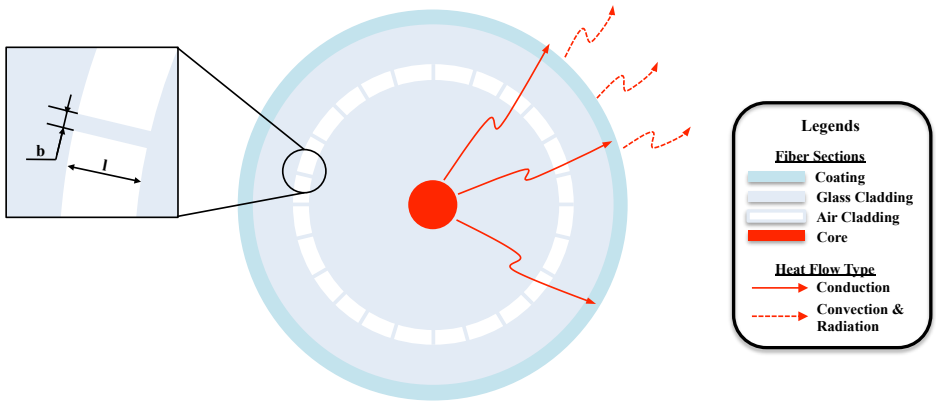

Figure 2.11: Illustration of heat dissipation across the fiber in air-clad fibers. The solid lines represent conductive heat transmission. The dashed lines are thermal convection and radiations.

Recently, with development of Photonic Crystal Fibers (PCF), air-clad fiber technology has been emerged as a novel design for pump cladding [66]. As shown in Fig. 2.11, the two layers of claddings of the fiber are separated by a ring of air holes. With the air-clad, a high NA up to 0.7 is enabled for the pump guiding clad, i.e. inner cladding of the fiber. This new design of fiber cladding structure is hence considered as a promising solution for high power handling with reduced nonlinearity and better thermal management. To investigate the heat dissipation of air-clad fibers, a modified model for temperature distribution calculation is required. In this structure, when heat is transferred to the air-clad level, it further flows to the outer-cladding through both

air chambers and the bridges between them. Although, the transportation of heat is by thermal conduction both in air chamber and fused silica bridge, the thermal conductivity of these two materials are different. Thus a model for the combined thermal conduction at air-clad region is required.

To calculate temperature distribution across air-clad, concept of thermal resistance is brought in as an analog to electrical charge. With such analogy, temperature difference drives heat flow through a thermal resistance as electrical voltage drives the current through electrical charge. Hence, similar to $\Delta V = R \cdot I$, the relationship between temperature difference ΔT and thermal resistance R_t can be expressed by $\Delta T = R_t \cdot \mathcal{P}$, where $\mathcal{P}$ is heat flow [67]. From temperature distribution expressions in Eqn. 2.40-2.42, one can derive that the thermal resistances R_{tcond} and R_{tconv} for heat conduction and convection in fiber cladding and surface respectively are given by:

$$R_{tcond} = \frac{\ln(r_2/r_1)}{2\pi\kappa} \tag{2.43}$$

$$R_{tconv} = \frac{1}{2\pi r_{coat}\alpha} \tag{2.44}$$

where r_1, r_2 are inner and outer radius of the cladding section while κ is the coefficient of heat conductivity for the cladding material. And α is convection coefficient for reservoir medium. For air-clad section, the thermal resistance R_{tac} is the combination of resistances of heat conduction of both bridge $R_{tbridge}$ and chambers $R_{tchamber}$:

$$R_{tac} = \frac{1}{1/R_{tchamber} + 1/R_{tbridge}} \tag{2.45}$$

where

$$R_{tbridge} = \frac{l}{mb\kappa_{clad}} \tag{2.45a}$$

$$R_{tchamber} = \frac{\ln\left(r_{a2}/r_{a1}\right)}{2\pi\kappa_{air}} \tag{2.45b}$$

r_{a2} and r_{a1} are radii of air-cladding inner and outer layer respectively. Thermal conductivity for air κ_{air} is about 0.02 W/(mK). m is the number of air holes, while l and b are bridge length and width respectively. As a result, the temperature distribution across an air-clad fiber is give by:

$$r_{clad2} < r \le r_{coat}, \quad T(r) = T(r_{coat}) + \frac{Q(z)r_o^2}{2\kappa_{coat}} \ln\left(\frac{r_{coat}}{r}\right) \tag{2.46}$$

$$r_{air} < r \le r_{clad2}, \quad T(r) = T(r_{clad2+}) + \frac{Q(z)r_o^2}{2\kappa_{clad}} \ln\left(\frac{r_{clad2}}{r}\right) \tag{2.47}$$

$$r_{clad1} < r \le r_{air}, \quad T(r) = T(r_{air+}) + \frac{Q(z)\pi r_o^2 l}{mb\kappa_{clad} \ln\left(\frac{r_{air}}{r}\right) + 2\pi\kappa_a l} \ln\left(\frac{r_{air}}{r}\right) \tag{2.48}$$

$$r_o < r \le r_{clad1}, \quad T(r) = T(r_{clad1+}) + \frac{Q(z)r_o^2}{2\kappa_{clad}} \ln\left(\frac{r_{clad1}}{r}\right) \tag{2.49}$$

$$0 \le r \le r_o, \quad T(r) = T(r_{o+}) + \frac{Q(z)r_o^2}{4\kappa_{core}} \left[1 - \left(\frac{r}{r_o}\right)^2\right] \tag{2.50}$$

where r_{clad2} and r_{clad1} are radii of inner and outer cladding respectively, r_{air} is outer radii of air clad layer.

A similar calculation for temperature and power distribution was done for an air-clad fiber with the same length of 2.5m as well as the same seeding and pumping power and wavelength as for the calculation of double-clad fiber shown before. The fiber core and coating size are same as that of the double-clad fiber, but with a inner cladding of 250μm and outer cladding of 400μm. The air-clad layer consists with 115 air holes with the bridge length of 5μm and width of 900nm. To compare the heat dissipation for the two different cladding structures, the pump power filling factors were assumed to be the same. The heat dissipation at air-clad fiber surface was also assumed to be with passive water convection. The simulation result is shown in Fig. 2.12. Plot (a) is transversal temperature distribution at the pump end while plot (b)

is the longitudinal core temperature distribution of the fiber. With same power amplification level, which means the same heat load, the temperature differences of fiber surface and reservoir are same for air-clad and double-clad fibers while the core temperature of air-clad fiber is elevated due to the less efficient heat transportation at air-clad region. This is clearly seen from the calculation of surface temperature by boundary condition (2.39) and temperature distribution at coating with Eqn. (2.40) or (2.46). The surface temperature is only dependent on the heat load in core, reservoir temperature, coating material and coating radius. Thus, air-clad structure is not superior at thermal management comparing to double-clad fibers with same size. Indeed, with air holes as a barrier for heat transportation, air-clad fibers would experience higher temperature in fiber cores than that of double-clad fibers, which would lead to a lower threshold for thermal lensing and modal instability in high power operation.

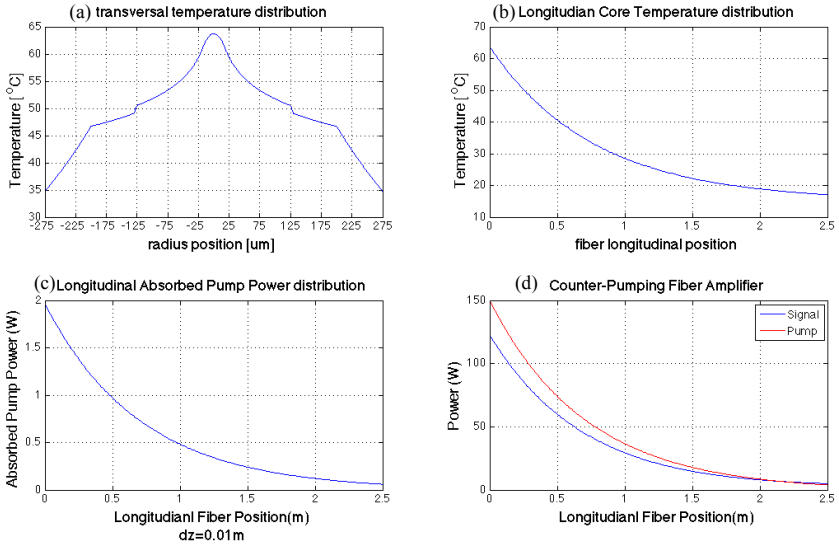

Figure 2.12: Simulation results of temperature and power distribution of an air-clad fiber with 37μm core and 250μm cladding in counter-pumped high power operation. (a-b) Transversal and longitudinal core temperature distribution with passive water convection at fiber surface. (c-d) Longitudinal distribution of absorbed power, pump power and signal power along the fiber.

However, due to the large acceptance angle of inner cladding, air-clad fiber is more efficient and compatible for high power lasing and amplification than double-clad or even triple

clad fibers. One can fabricate air-clad fiber with small inner cladding for high absorption of pump power and hence short fiber length in need to avoid onset of nonlinear effects while the outer cladding is kept large for better heat dissipation.

Table 2.3: Parameters of fiber and pump used in the calculation

Fiber Parameters		
Fiber Type	Double-Clad Fiber	Air-Clad Fiber
Core Size	37 μm	
Cladding Size	250 μm	250/260/400 μm
Coating Size	350 μm	550 μm
Pump Absorption Ratio @ 976nm	9 dB/m	
Seeding Wavelength	1064nm	
Seeding Power	5W	
Pumping Information		
Pump Wavelength	970nm	976nm
σ_{ap}	$0.641\times10^{-24}m^2$	$2.54\times10^{-24}m^2$
σ_{ep}	$0.545\times10^{-24}\ m^2$	$2.1\times10^{-24}m^2$
Fiber Length	5m	2.5m

The main purpose of this power and temperature simulation model is for the design of high power fiber amplifiers. One can compare and choose fiber length, pump wavelength by this calculation to optimize the power scalability of the system. Fig. 2.13 shows an example of analysis for power scalability for different fiber type, fiber length and pump wavelength. In this case, performance of two pieces of double-clad fiber and air-clad fiber with same core size are investigated. The inner cladding of double-clad fiber was chosen to be the same as that of air-clad fiber to keep the pump power filling factors the same for both fiber structure and hence the similar pump absorption ratio for both fibers, which is 9dB/m at 976nm. The coating and core temperature of both fibers under different pumping wavelength choices are calculated with assumption of passive water convection at fiber surface. The length of fiber in use was also adjusted for different pump absorption ratio according to the pump wavelength. Parameters of fibers and pumping used in simulation are listed in table 2.3.

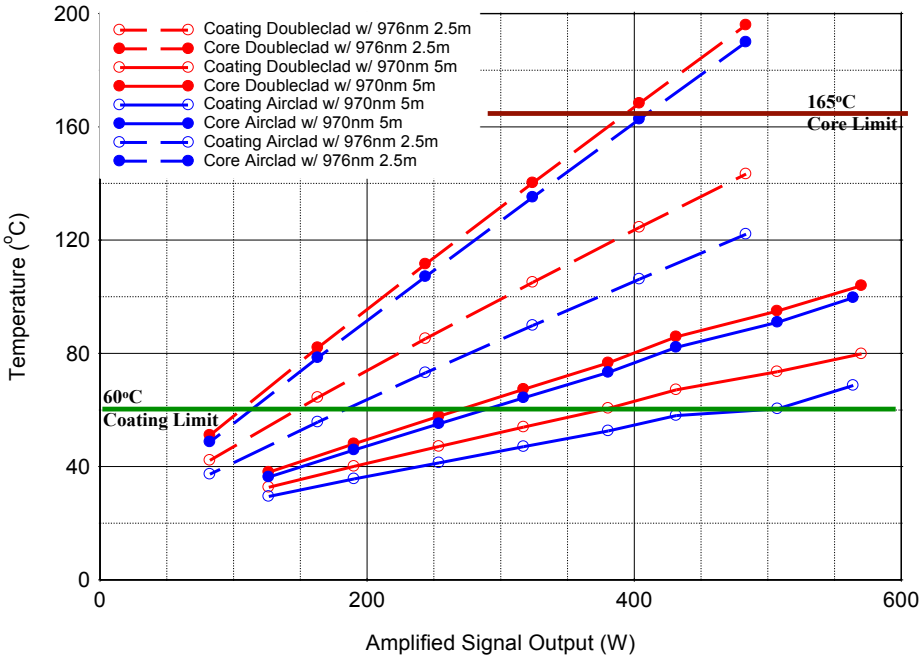

Figure 2.13: Temperature of coating and core of double-clad and air-clad fiber at the pump end of the fibers versus amplified signal power. Red lines are temperature of double-clad fiber while blue lines are that of air-clad fiber. Lines with dot marks are coating temperature and the ones with circular marks are core temperature. Dashed lines are results for 2.5m of fibers pumped at 976nm while the solid lines are that for 5m of fibers pumped at 970nm.

As summarized in Fig. 2.13, temperature with air-clad fiber is lower than that with double-clad fiber at same output amplified signal power level as discussed earlier due to the larger total size of fiber for air-clad fiber. Although with 976nm pumping wavelength, shorter fiber length is needed for high power amplification, the heat load distribution along the fiber is large and hence the temperature of fiber coating exceeds the 60°C coating temperature limit at a very low amplified power level for both types of fiber. Consequently, operation with a 5m long fiber pumped at 970nm is a better choice to optimize the power scalability of the system. More careful analysis is needed for the selection of fiber length and pumping wavelength to keep temperatures of fiber core and coating below the limits under high power operation while onset of nonlinear effects is avoided.

2.4 Conclusion

In this Chapter we presented a numerical model for calculating power and temperature distribution along the fiber. Using this and, additionally, an analytical laser model, we study the effects of fundamental mode leakage from the central core into the cladding on the total and in-core signal efficiencies. It is shown that in-core efficiency is much more sensitive to this leakage-loss magnitude than the total-signal efficiency. It is also shown that only the total loss per amplifier or laser is important. Degradation of this in-core efficiency, as well as output beam quality degradation due to presence of cladding light, with increasing leakage-loss sets the constraints for this loss of less than approximately 1.5dB to 3dB of total loss per amplifier or laser. For a typical pulsed amplifier length of approximately 3m, this corresponds to 0.5dB/m to 1dB/m of acceptable leakage loss. For a high power laser or amplifier, with a longer fiber length this would lead to even lower required leakage loss per unit length.

Chapter 3

Polarization maintaining properties of CCC fibers

Polarization maintenance in optical fibers is very important for numerous fiber laser and amplifier applications, where a *defined and stable* polarization of the output beam is required. For example, a polarized high peak power source is necessary for efficiently nonlinear frequency conversion [69], stable narrow-linewidth fiber laser sources for advanced gravitational wave detectors are also need to be polarized [70], stability of coherently combined laser beam can only be achieved with robustly polarized individual channel outputs, etc.

Currently dominant technique for achieving polarization preservation in optical fibers relies on high-birefringence (Hi-Bi) induced in a fiber. However, as core size of a fiber increases, it becomes increasingly more difficult to achieve high birefringence, since the stress-induced birefringence is inversely related to the separation between stress-producing regions, and geometrical-effects vanish as well, as described in more detail in this chapter. Furthermore, it might be difficult to combine high birefringence with fiber core structures designed to achieve effectively single-mode operation, such as CCC fibers. Nevertheless, experimental observations revealed that CCC fiber based amplifiers and lasers do preserve polarization [59,62,71] to a remarkable degree despite the fact that current CCC structures do not include any Hi-Bi producing elements.

In this chapter, detailed theoretical and experimental analysis of polarization-maintaining characteristics of CCC fibers is presented. We show all the internal random polarization perturbations are eliminated in CCC fibers due to fiber preform spinning during fiber fabrication, and CCC fiber core is effectively single mode fiber. We also show that, large transverse diameters typically associated with the large core CCC fibers lead to increased immunity to external birefringence. At the end of the chapter we consider effects of coiling-induced linear birefringence and twisting-induced circular birefringence on CCC fiber polarization properties, an important practical aspect for designing an integrated fiber system.

3.1 General description of fiber polarization properties.

3.1.1 Origins of polarization effects in optical fibers

Electric wave propagation along a lossless fiber could be represented by linear superposition of two modes as:

$$\overrightarrow{E(z)} = C_x\hat{x} + C_y\hat{y}; \tag{3.1}$$

where $C_j = c_j e^{ik_j z}$ represent the amplitude and phases of the propagating modes. Ideally, in a perfect fiber with circular symmetry, the propagation vector k_j for the two modes equals to each other, and all the polarization modes propagating through the fiber are preserved. However, in practical fibers, defects within fiber core shape as well as asymmetrical lateral stress either within the fiber or from external source would all break this rotational symmetry of the fiber structure, causing variation between refractive indices in orthogonal transverse direction, which is the birefringence of fiber: $\delta n = n_y - n_x$. As a result, modes aligned with different axes traveling with different phase velocities. Therefore, for light fields not aligned with either of the eigen polarization mode axes, the polarization states would shift along the propagation, due to a

linear retardation between orthogonal polarization mode components. Furthermore, these imperfections are usually randomly oriented along the fiber, consequently, for long propagation lengths, no eigen polarization modes exist.

In general, mechanisms introducing birefringence changes in an optical fiber are categorized into two major classes: (i) internal and (ii) external birefringence perturbations [15]. The internal birefringence perturbations stems mainly from geometrical deformation of fiber core, frozen-in asymmetric lateral stress during the fabrication as well as modal scattering in LMA fibers.

Unintentional elliptical deformation of the fiber core is inevitable during the fabrication, since it is difficult to precisely control the heat distribution across fiber preform as well as different thermal contractions with different materials of the fiber structure. The noncircularity of the core then causes different propagation constant for the two modes with orthogonal polarization, which raises intrinsic birefringence of fiber by both geometrical anisotropy and stress birefringence [72,73]. For fibers with large core size, propagating modes are usually confined within the core area and hence the core deformation would not causing stress birefringence. In an elliptical shaped fiber core, light travels faster along the axis that is the smallest transverse dimension. With ellipticity "e", radius "r_c" of the fiber core as well as refractive index difference between core and cladding "Δ" known, the birefringence caused by this geometrical deformation is approximated by [73]:

$$\delta n = \frac{e^2(2\Delta)^3}{r_c k_0}\frac{W^2}{8V^3}\left[U^2 + (U^2 - W^2)\left(\frac{J_0(U)}{J_1(U)}\right)^2 + UW^2\left(\frac{J_0(U)}{J_1(U)}\right)^3\right] \qquad (3.2)$$

where k_0 is the propagation vector of light wave in vacuum. $V = n_{core} r_c k_0 \sqrt{2\Delta}$ is the V number of the fiber. U and W are usual circular waveguide parameters given by:

$$U = r_c\sqrt{n_{core}^2 k_0^2 - \beta^2},$$

$$W = r_c\sqrt{\beta^2 - n_{clad}^2 k_0^2},$$

where β is the fundamental mode propagation vector in the fiber. From the expression in (3.2), it is clearly shown that the birefringence induced by geometrical deformation of fiber core is frequency dependent, and it scales inversely with the fiber core size, i.e. the larger the fiber core size, the smaller the birefringence is with same core ellipticity. It is also worth noting that, magnitude of the core deformation induce birefringence is non-related to the cladding or total size of the fiber, which is also reasonable, since the size of cladding or total fiber does not affect the propagation of modes in core.

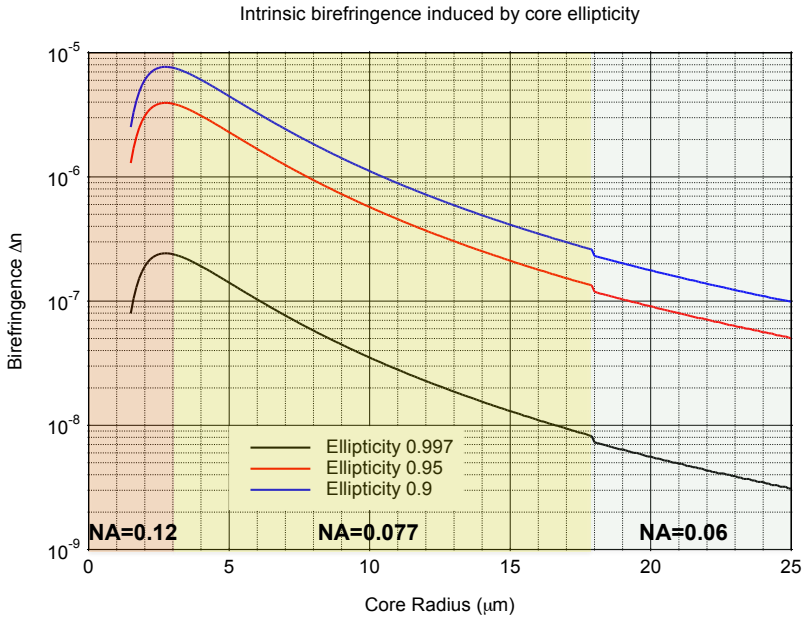

Figure 3.1: Intrinsic birefringence generated by non-circularity of the core. The different color of shades of areas represent different NA of core for various sizes of the fiber. The red area is conventional single mode fiber with NA=0.12, core size smaller than 6μm. The yellow area is for LMA fibers with NA=0.077, core size from 6~35μm. The green area is for LMA fiber with NA=0.06 and core size from 35~50μm. The three curves are calculation results with different core ellipticities. Blue is for e=0.9. Red is for e=0.95 and black is for e=0.997.

Fig. 3.1 depicts calculation results following Eqn. (3.2) for fibers with core radii range from 1.5μm to 25μm. For different core size, NA is adjusted according to specifications of

commercialized single mode and LMA fibers. The computation was done with core ellipticity assumed to be 0.9, 0.95 and 0.997 respectively. The simulation shows intrinsic birefringence induced by core deformation degrades by over one order of magnitude with core size increasing from 6μm standard single mode fiber to 30μm LMA fiber.

In weakly guided fibers, the propagating modes are categorized as LP modes [74], with which the mode fields are almost transverse while the spatial intensity patterns are similar to that of TEM modes in transverse planes. Consequently, each LP mode consists of a set of submodes, which are indeed linear polarization modes. For fiber with negligible birefringence, these submodes are degenerated. For fiber with certain birefringence, two distinct polarization axes are presented in transverse plane, and hence, these submodes will have different propagation velocities from each other. For example, two non-degenerated polarization modes occur for LP_{01} mode, and four distinct polarization modes exhibit for LP_{11} associated with the spatial field patterns, all propagating at different velocities. The field patterns of LP_{01}, LP_{11} mode are depicted in Fig. 3.2.

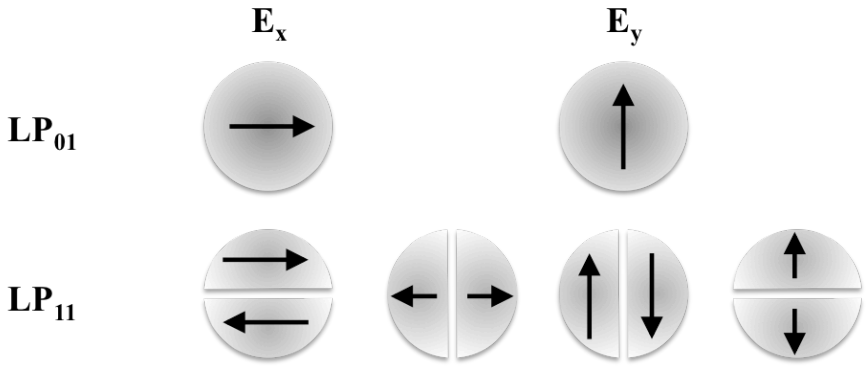

Figure 3.2: Electric field distributions for LP_{01} and LP_{11} mode.

For LMA fibers without effectively single-mode controlling, excitation into HOMs are inevitable by either mode coupling mismatch in free space systems or splicing defects induced

perturbation in monolithic systems. Since the electric fields of scattered HOMs propagating with different phase velocities from that of fundamental mode are randomly oriented due to the cylindrical symmetry of optical fiber, the polarization preservation of the fiber would be degraded. Furthermore, with scaling up of the core size, more and more HOMs are supported in the fiber, and hence, stronger de-polarization would occur.

External birefringence perturbations may be introduced to fibers by asymmetric lateral stress due to mounting, bending of the coiled fiber during packaging, twisting of the fiber associated with the coiling of fiber, and transverse electric field or axial magnetic field applied under certain situations. The last two perturbations are not commonly seen with fiber amplifiers, thus they will not be discussed in this thesis. However, the first three perturbations, which are all basically related to stress induced perturbation, are always inevitable to some degree in mounting and packaging of fiber amplifiers.

Asymmetrical lateral stress generally introduces a linear birefringence by producing an elastic stress anisotropy in the fiber core. When fiber is sandwiched between two parallel plates as for the usual arrangement of fiber cooling with cold plates, the birefringence induced is given by [75]:

$$\delta n_f = 4C_s \frac{f}{\pi r k_0 E} \tag{3.3}$$

where $C_s = 0.5k_0 n_0^3(\rho_{11} - \rho_{12})(1 + \nu_p)$. C_s/k_0 is a strain-optical coefficient related to fiber and material parameters, with n_0 as the average refractive index of fiber core, ρ_{11} and ρ_{12} as strain-optical tensor components of fiber material and ν_p as Poisson's ratio. E is Young's modulus of the fiber material, which is about 7.6×10^{10}N/m^2; f is the line force applied to the fiber per unit length and r is the outer radius of the fiber. The fast axis of this birefringence is along

the direction of the compressive force applied. For fiber pressed into a V-groove, a modified expression could be used for the induced birefringence as [76]:

$$\delta n_V = 2C_s(1 - \cos 2\delta \sin \delta)\frac{f}{\pi r k_0 E} \tag{3.4}$$

where 2δ is the included angle of the V-groove. The fast axis is still along the direction of the compressive force on the fiber. For V-groove mounting scheme, the birefringence is reduced comparing to the case with parallel plates mounting with same amount of force applied and will fall to a minimum value with 60° of the included angle due to the balance of reaction forces and friction from walls of the V-groove. In fused silica, n_0=1.45, ρ_{11}=0.12, ρ_{12}=0.27 and ν_p=0.17. Therefore, $C_s \approx 1.62\times10^6 m^{-1}$ at λ=1064nm. The linear birefringence induced per N/m for various outer cladding sizes is depicted in Fig. 3.3. It clearly shows the inverse dependence of induced birefringence and fiber cladding size.

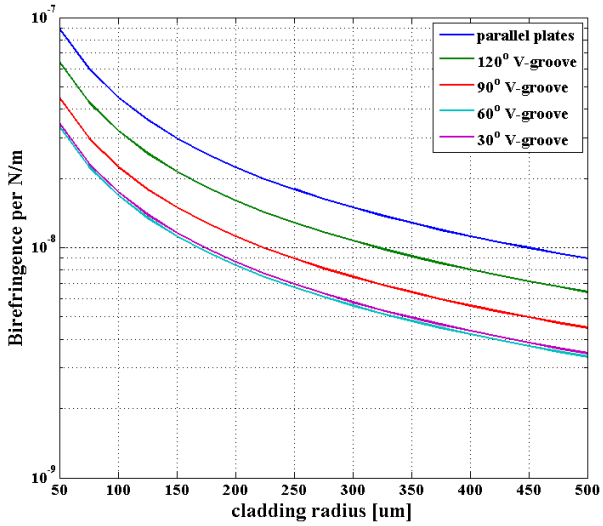

Figure 3.3: Birefringence per N/m induced by asymmetric lateral forces applied externally. Blue curve is with parallel plates. Curves with green, purple, black and red are the birefringence induced by V-groove mounting with the included angle of V-groove as 120°, 90°, 60° and 30°.

Bending of the fiber introduces also a linear birefringence in fiber by elasto-optic index changes. There are three forms of bending in practical fiber mounting situations: (i) freely bent,

(ii) bent around a drum under tension, (iii) kinked over a sharp object on the drum. The total birefringence induced by bending of the fiber would be the sum of individual birefringence induced by these three cases as long as they are presented. For freely bent fiber, as in case when fiber is coiled to a radius of R and lay on a plate, the compressive stress now is the tension from outer portion of fiber cross section pressed laterally onto the inner portion. The induced birefringence would have a fast axis perpendicular to the bending axis and is given by [77]:

$$\delta n_b = 0.5 C_s \frac{r^2}{k_0 R^2} \tag{3.5}$$

Unlike the case with external lateral stress, the birefringence now depends quadratically on the outer cladding size and also inversely related to the bending radius. This could be easily interpreted since for thicker size of the fiber, the more effort needed to bend it to a smaller size, and thus more tension is applied to the fiber.

Winding the fiber around a drum with axial tension F is also a commonly used method for fiber packaging. In this case, additional linear birefringence is produced from the lateral reaction force by the drum to the axial tension F. It is given by [78]:

$$\delta n_{tc} = \frac{C_s}{k_0} \frac{2-3\nu_p}{1-\nu_p} \frac{r}{R} \epsilon \tag{3.6}$$

where $\epsilon = F/(\pi r^2 E)$ is the mean axial strain in the fiber, which may be assumed as a fixed value 0.5% as a moderate large tension applied for various fiber radius.

One practical perturbation usually accompanied with winding the fiber around a drum is the kink of one fiber turn when it crosses another. In this case, an additional birefringence δn_k is added to δn_b and δn_{tc} within the short length of fiber affected by the kink. Denoting height of the obstacle causing kink as H, the local birefringence produce is given by [79]:

$$\delta n_k = 0.5 \frac{C_s}{k_0} \frac{r}{R} \sqrt{\frac{H\epsilon}{R}} \tag{3.7}$$

When the kink is from crossing of the fiber turns, H is the diameter of fiber, i.e. H=2r.

While all the perturbations discussed above produce linear birefringence, twisting of a fiber leads to a coupling of longitudinal electric field of one mode with the transverse field of the orthogonal mode by shear stress. And therefore a circular birefringence is produced, since the phase difference between these two fields are π/2. The resulting circular birefringence δn_t is linearly proportional to the twist rate τ [80]:

$$\delta n_t = \frac{g\tau}{k_0} \tag{3.8}$$

where $g = -0.5 n_0^2 (\rho_{11} - \rho_{12})$. For fused silica fiber, g is about 0.157. Therefore, for operating wavelength of 1064nm, about 1.66×10^{-7} of birefringence is induced for twist rate at 1 turn/m. In practice, one can deliberately twist the fiber with large twist rate to create strong circular birefringence in the fiber. However, the larger the size of the fiber, the harder it is to twist the fiber. Consequently, the maximum circular birefringence one can achieve by twisting the fiber is inversely related to the fiber core size and cannot be utilized to generate Hi-Bi in a fiber. Moreover, it is also worth noting that small amount of twisting is always associated with coiling of the fiber to balance the surface area difference of outer and inner portion of the fiber. For small size fibers such as conventional single mode fibers, the line difference between inner and outer surface of the fiber is about 0.3mm / turn and will not causing fiber twisting until several rounds of coiling. However, for fiber with large cladding size, the influence is more significant since not only the line difference scales up but also the affected surface area also scales up with the fiber size. And the following analysis is only valid for fiber with large cladding size. To

roughly calculate the twisting rated due to coiling, half turn per coil would be a reasonable estimation. And a relation between twisting rate τ and coiling radius R is derived as:

$$\tau = \frac{1}{2R} \tag{3.9}$$

Using Eqn. (3.8) and (3.9), the circular birefringence in the fiber from bending induce twisting is:

$$\delta n_t = \frac{g}{2Rk_0} \tag{3.10}$$

It shows that δn_t is inversely dependent on the coiling radius but immune to the fiber size. This bending related twisting is of practical significance, since it complicates the birefringence perturbation in packaging process, and may largely affect the polarization preservation in real fiber laser systems. Detailed description of the combining effect of linear birefringence induced by bending and lateral stress with twisting induced circular birefringence is given in the next subsection. The birefringence induced by the three bending types as well as from the bending related twisting are calculated and depicted in Fig. 3.4.

The calculation results of birefringence originated from bending of the fiber for the three types all scales up with increasing fiber size while inversely related to the coiling radius. However, winding fiber onto a drum with axial tension may cause more than one magnitude of order of birefringence than that from the freely bending case. Also, the kink induced local birefringence is also non-trivial compared to the free bending birefringence. The total birefringence roots from these three mechanisms, if all were presented, would be roughly around the order of 10^{-6} for fiber cladding size from 200μm to 600μm. Indeed, when fiber size scales up, the achievable coiling radius also increases to avoid substantial leakage loss of fundamental mode. As a result, the bending induce birefringence will grow much more slowly with increasing fiber size in real systems. Similarly, for circular birefringence introduced by twisting associated

with the coiling may degrade with the scaling of fiber size in practical systems. Consequently, this circular birefringence only matters when fiber is freely bent with outer cladding size no more than 600μm.

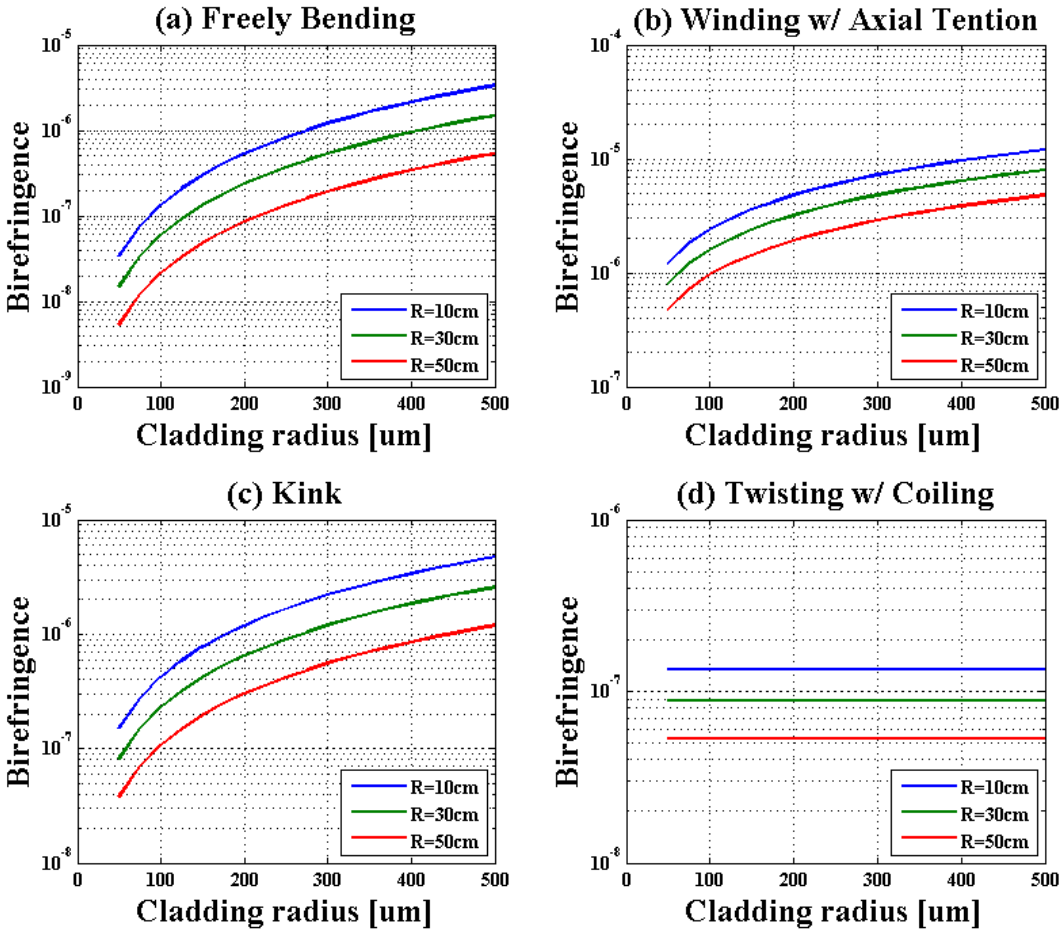

Figure 3.4: Birefringence induced by various sub-conditions associated with coiling of the fiber: (a) freely bending of the fiber; (b) winding of the fiber around a drum with axial Tension $F \approx 0.5\% \times \pi r^2 E$; (c) kink induced localized birefringence change with fiber wound around the drum; (d) coiling induced twisting of the fiber. All the calculations were carried out with fiber size ranging from 100μm to 1000μm. Different colored curves represent different coiling radius applied.

3.1.2 Polarization evolution and coupling along the fiber

In practical fiber laser systems, the polarization state injected into the system may experience with more than one single birefringence perturbation introduced in the previous

section. The combined effect of several birefringences on the propagating polarization states needs to be analyzed for the prediction and controlling of output polarization. Two methods are commonly used in analysis of polarization states evolution along an optical fiber: Poincaré sphere representation [80] and Couple mode theory [82]. For uniformly distributed birefringence known over the whole fiber length, Poincaré sphere representation would be a convenient way for understanding of polarization state evolution along the fiber; while for analysis of polarized light propagation with random perturbations locally applied to the fiber, couple mode theory is more useful.

Fig. 3.5 illustrates a Poincaré sphere representation of an elliptical polarization state with azimuth angle ϕ and ellipticity angle $\psi = \text{atan}(\frac{b}{a})$, where "b" is the minor axis and "a" is the major axis of polarization ellipse. With 2ϕ as the longitude and 2ψ as the latitude on the sphere, all linear polarization states would lie on the equator while the left-hand and right-hand circular polarization stated at the north and south poles respectively. States on the rest of the sphere are all elliptical polarization states with all the left-hand polarization states on the north hemisphere and the right-hand ones on the south hemisphere. The position of the polarization state on the sphere could also refer to angular coordinates χ and ξ, which are given by:

$$\begin{cases} 2\chi = \text{atan}\frac{|c_x/c_y|-1}{|c_x/c_y|+1} \\ 2\xi = \arg\frac{c_x}{c_y} \end{cases} \tag{3.11}$$

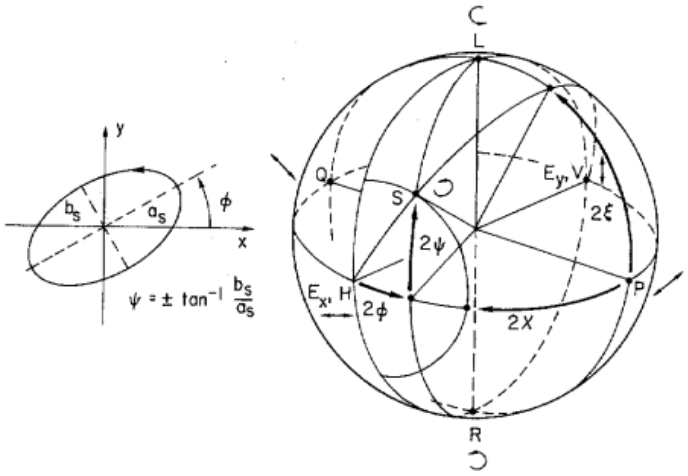

Figure 3.5: Illustration of Poincaré sphere representation for a random elliptical polarization state with azimuth angle ϕ and ellipticity angle ψ [81].

One key feature of Poincaré sphere representation is that for any birefringence perturbation β, the state of polarization will rotate on the surface of the sphere about axis of vector representation of this perturbation through an angle $\omega = \beta \cdot L$, where L is the length of propagation distance. Therefore, the polarization state evolution in fiber with linear, circular and elliptical birefringence perturbation may be depicted as in Fig. 3.6. Individual birefringence perturbation could be represented as a vector in the sphere. The magnitude of the vector equals to that of the birefringence perturbation itself, while its orientation is defined by the azimuth angle ϕ_p and ellipticity angle ψ_p of this perturbation in a similar way as that for the representation of polarization states. For linear birefringence perturbation as shown in Fig. 3.6(a), the vector $\overrightarrow{\beta_p}$ lies in equator plane then, with longitude $2\phi_p$ as two times of the azimuth of the fast axis of this perturbation. And all the input polarization states propagating along the fiber will transform to other states and then reproduce the input state every $L_p = 2\pi/\beta_p$, which is named as the beating length of this perturbation. Only input states at points where the axis of vector $\overrightarrow{\beta_p}$ intersects with the surface of the sphere would remain unchanged through the traveling, which are the

eigenstates of this perturbation and are orthogonal to each other. Likewise, for circular birefringence perturbation, the vector $\vec{\alpha}$ is long the polar axis as shown in Fig. 3.6 (b). And in this case, the eigenstates are the two circular polarization states.

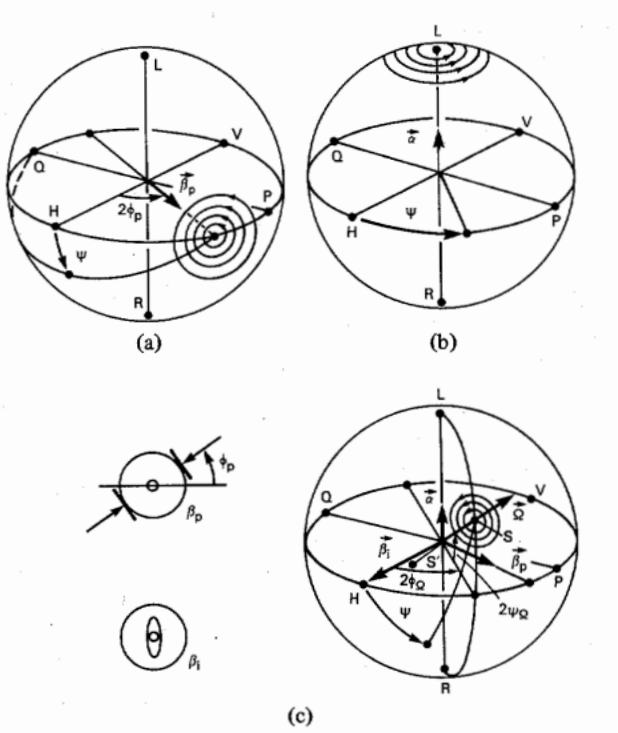

Figure 3.6: Polarization states evolution under birefringence perturbation of (a) linear; (b) circular; (c) elliptical as the combination effects of linear and circular [81].

In practical systems, intrinsic birefringences and external perturbations usually coexist with each other and that leads to the analysis of combined effect of several birefringences. As shown in Fig. 3.6 (c), a vectorial addition of all the individual birefringence perturbations $\vec{\Omega} = \vec{\beta_i} + \vec{\beta_p} + \vec{\alpha}$, may represent this combined effect, with $\vec{\beta_i}$ as the intrinsic birefringence of the fiber, $\vec{\beta_p}, \vec{\alpha}$ as the linear and circular external perturbation respectively. The magnitude of this combined birefringence is then:

$$\Omega = \sqrt{(\beta_i + \beta_p \cos 2\phi_p)^2 + \left(\beta_p \sin 2\phi_p\right)^2 + \alpha^2} \tag{3.12}$$

where ϕ_p is the angle between the fast axes of external linear perturbation and intrinsic birefringence. The physical meaning of the three components constitute Ω is that when external perturbation β_p and α are applied to the fiber, the intrinsic birefringence perturbation β_i is detuned by $\beta_p \cos 2\phi_p$, and the eigenstates of β_i is cross coupled to each other by $\sqrt{\left(\beta_p \sin 2\phi_p\right)^2 + \alpha^2}$. Assuming that the intrinsic birefringence has its fast axis lies along horizontal direction (which is kept for all the theoretical analysis in this chapter, if no other statement is made) and only horizontal linear polarization P_H is sent into the fiber, the coupling of power between the two eigen-polarization-states is given by [81]:

$$\frac{P_V}{P_H+P_V} = \frac{\left(\beta_p \sin 2\phi_p\right)^2+\alpha^2}{\Omega^2} \sin^2\left(\frac{\Omega L}{2}\right) \tag{3.13}$$

Accordingly, to have the same horizontal linear polarization states emitting from the fiber, one of the following two conditions must be satisfied for arbitrary angle ϕ_p:

$$L = \frac{2N\pi}{\Omega}, or \quad {\beta_p}^2 + \alpha^2 \ll {\beta_i}^2 \tag{3.14}$$

where N is arbitrary integer number. With the first condition satisfied, the fiber length is indeed the beating length of the combined birefringence. In this way, the input polarization state continuously transforms during the propagation and reproduces itself at the fiber output end. The second condition is to utilize very large intrinsic birefringence, so that the cross-coupling power between eigenstates is negligible and the input polarization state is preserved all along the fiber as long as it is aligned with the eigenstates of intrinsic birefringence. This is also the principle for most of polarization maintaining (PM) fibers nowadays, which are usually categorized as Hi-Bi fibers. Conventional technique, which dominates the current PM fiber fabrication is to introduce very high (usually > 10^{-4}) internal birefringence by making elliptical inner cladding surrounding

the fiber core or including two stress rods on opposite sides of the fiber core as in the case of PANDA fiber and Bow-tie fiber as illustrated in Fig. 3.7. Both methods are based on introducing different thermal expansions and hence increased stress birefringence with the noncircular cladding or stress bars [83-85]. Although polarization maintenance within conventional single mode fibers by adding stress rod has been fully developed, it becomes more and more difficult to introduce sufficient and stable intrinsic stress for creation of high birefringence in LMA fibers with core size larger than 50μm.

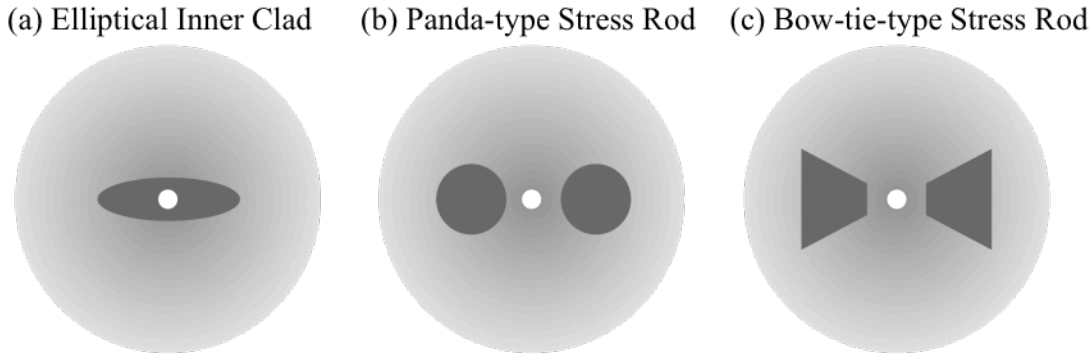

Figure 3.7: Cross-sections of commonly used Hi-Bi fibers.

It is also worth noting that the same principle also applies for fiber with intrinsic circular birefringence. In this case, the cross coupling power is:

$$\frac{P_L}{P_R+P_L} = \frac{{\beta_p}^2}{{\beta_p}^2+\alpha^2}\sin^2\left(\frac{\sqrt{{\beta_p}^2+\alpha^2}L}{2}\right) \tag{3.15}$$

And polarization preservation is also achievable as long as the circular birefringence is much larger that the external perturbation.

When the multiple external perturbations are randomly applied to the fiber, the Poincaré sphere representation for polarization evolution is no longer convenient and the couple-mode

theory is more applicable. The coupled-wave equations for the field amplitudes of the two polarization eigenstates consisted in Eqn. (3.1) are [82]:

$$\begin{cases} dC_x/dz = i\kappa_x C_x + i\kappa C_y \\ dC_y/dz = i\kappa^* C_x + i\kappa_y C_y \end{cases} \tag{3.16}$$

with weak coupling approximation, (3.16) is reduced to:

$$\begin{cases} dc_x(z)/dz = i\kappa c_y(z) e^{i\beta z} \\ dc_y(z)/dz = i\kappa^* c_x(z) \mathrm{e}^{-i\beta z} \end{cases} \tag{3.17}$$

where $\beta = \kappa_y - \kappa_x$ is the detuning coefficient equals to propagation difference between two eigenstates. κ is the coupling coefficient between the two states. Following the denotation of effective combined birefringence $\vec{\Omega}$ in (3.12), these two coefficients are:

$$\beta = \beta_{\mathrm{i}} + \beta_{\mathrm{p}} \cos\left(2\phi_{\mathrm{p}}\right), \quad 2\kappa = \beta_{\mathrm{p}} \sin\left(2\phi_{\mathrm{p}}\right) - i\alpha \tag{3.18}$$

With initial condition $\begin{cases} c_{x0} = c_x(0) \\ c_{y0} = c_y(0) \end{cases}$ *and* $\begin{cases} dc_x(z)/dz\big|_{x=0} = i\kappa c_y(0) \\ dc_y(z)/dz\big|_{\mathrm{y}=0} = i\kappa c_x(0) \end{cases}$ applied, the solutions to (3.17) are:

$$\begin{cases} c_x(z) = \left[c_x(0)\cos\left(\frac{\Omega}{2}z\right) + \frac{i}{\Omega}(2\kappa c_y(0) - \beta c_x(0))\sin\left(\frac{\Omega}{2}z\right)\right] e^{\frac{i\beta z}{2}} \\ c_y(z) = \left[c_y(0)\cos\left(\frac{\Omega}{2}z\right) + \frac{i}{\Omega}(2\kappa^* c_x(0) + \beta c_y(0))\sin\left(\frac{\Omega}{2}z\right)\right] e^{-\frac{i\beta z}{2}} \end{cases} \tag{3.19}$$

where Ω is still the magnitude of combining effect of all the birefringences: $\Omega = \sqrt{4\kappa\kappa^* + \beta^2}$

Eqn. (3.19) can also be write in matrix representation:

$$\begin{bmatrix} c_x(z) \\ c_y(z) \end{bmatrix} = \begin{bmatrix} e^{\frac{i\beta z}{2}} & 0 \\ 0 & e^{-\frac{i\beta z}{2}} \end{bmatrix} \begin{bmatrix} T_{11} & T_{12} \\ T_{21} & T_{22} \end{bmatrix} \begin{bmatrix} c_x(0) \\ c_y(0) \end{bmatrix} \tag{3.20}$$

where

$$\begin{cases} T_{11} = \cos\left(\frac{\Omega}{2}z\right) - \frac{i\beta}{\Omega}\sin\left(\frac{\Omega}{2}z\right) \\ T_{12} = \frac{2i\kappa}{\Omega}\sin\left(\frac{\Omega}{2}z\right) \\ T_{21} = -T_{12}^{*} \\ T_{22} = T_{11}^{*} \end{cases} \tag{3.21}$$

It is again manifested that the output polarization states equals to the input polarization only when $z = \frac{2\pi}{\Omega}$, or $\kappa \ll \beta$ is satisfied, and the latter condition is when polarization preservation achieved.

With all the internal and external birefringences perturbation known, the evolution of polarization states could thus be described by accumulating the calculation in Eqn. (3.20) for individual fiber sections with different birefringence status along the direction of mode propagation.

3.2 Polarization properties of CCC fiber

3.2.1 Intrinsic birefringence properties of CCC fibers

Generally, CCC fiber has local internal birefringences attributed to the structure of itself. First of all, unique structure of side core wound around the central core causes linear birefringence in the spacing between side core and central core due to the different thermal expansion coefficients associated with the two cores and the cladding region in between them [56]. The magnitude of this linear birefringence could be as large as 10^{-3}, however, due to the small area outside the central core it exists, the residual linear birefringence across the central core is largely reduced, which is around 10^{-6} with a reasonable estimation. Additionally, also due to the side core structure which is very close to the central core (<10μm), a pulling tension is exerted to the central core while the fiber is in "molten" state during the fabrication process, which easily leads to a deformation of central core to "egg" shape for CCC fiber with single side

core or a polygonal shape for that with multiple side cores (Fig.3.8). Assuming that the ellipticity of deformed central core is about larger than 0.95, for a CCC fiber with core size around 30~50μm, the birefringence originated from geometrical deformation is less than 1×10^{-7} according to the calculation results shown in Fig. 3.1.

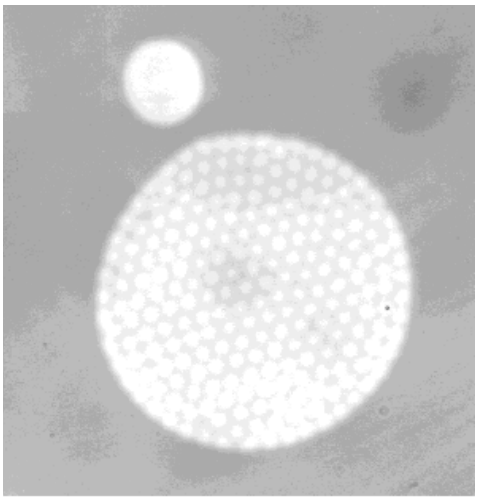

Figure 3.8: Example of central core deformation towards the side core.

Following the description above, one would conclude that CCC fiber is a non-PM fiber which suffers the similar random internal birefringence as for other conventional fibers, though at a lower level due to the large core size. However, one key feature also resulting from the structure of CCC fiber eliminates the effect of internal birefringence, which is the spinning of preform during pulling process of CCC manufacture to creat the hellical structure of side core. The spining of fiber preform while in its 'molten' state, interchanges the fast and slow axis of the internal birefringence within the fiber. Hence, the overall effect of spin on polarizaiton mode propagation could be predicted, using aforementioned couple-mode theory applied to a twisted anisotropic medium [86, 87]. In this case, the intrinsice birefringence β_i is not detuned but a coupling between orthogonal eigenstates by the spin rate ξ is present. The coupling coefficient κ, representing the coupling rate between eigenstates, equals to the spin rate $i\xi$. Assuming that the

fast axis of internal birefringence is along x direction and following Eqn. (3.19), the polarization states along fiber is:

$$\begin{cases} c_x(z) = \left[c_x(0)\cos\left(\frac{\Omega}{2}z\right) + \frac{i}{\Omega}(2\mathrm{i}\xi c_y(0) - \beta_\mathrm{i} c_x(0))\sin\left(\frac{\Omega}{2}z\right)\right] e^{\frac{i\beta_\mathrm{i} z}{2}} \\ c_y(z) = \left[c_y(0)\cos\left(\frac{\Omega}{2}z\right) + \frac{i}{\Omega}(-2\mathrm{i}\xi c_x(0) + \beta_\mathrm{i} c_y(0))\sin\left(\frac{\Omega}{2}z\right)\right] e^{-\frac{i\beta_\mathrm{i} z}{2}} \end{cases} \tag{3.22}$$

where $\Omega = \sqrt{{\beta_i}^2 + 4\xi^2}$ is the combined effect of intrinsic birefringence and the spin induced coupling. The azimuth angle ϕ and ellipticity angle ψ of the polarization states is related to the electric fields at x and y direction as:

$$\phi = \frac{1}{2}\mathrm{atan}\left(\frac{C_x C_y^* + C_y C_x^*}{C_x C_x^* - C_y C_y^*}\right) \tag{3.23}$$

$$\psi = \frac{1}{2}\mathrm{asin}\left(i\left(C_x C_y^* - C_y C_x^*\right)\right) \tag{3.24}$$

With linear polarization input at angle θ to the fast axis of the internal birefringence, at longitudinal position z is hence given by:

$$\phi = \frac{1}{2}atan\left(\frac{-\frac{2\xi}{\Omega}sin\,(\Omega z)\cos\,(2\theta) + cos(\Omega z)\sin\,(2\theta)}{[\left(\frac{\beta_i}{\Omega}\right)^2 + \left(\frac{2\xi}{\Omega}\right)^2 cos(\Omega z)]\cos\,(2\theta) + \frac{2\xi}{\Omega}si\,n(\Omega z)\sin\,(2\theta)}\right) \tag{3.25}$$

$$\psi = \frac{1}{2}\mathrm{asin}\left(\frac{\beta_i}{\Omega}\left(\frac{2\xi}{\Omega}(cos(\Omega z) - 1)\cos\,(2\theta) + sin(\Omega z)\sin\,(2\theta)\right)\right) \tag{3.26}$$

In CCC fiber fabrication, the spun rate is usually around 6mm / turn, and thus $\xi \approx 167$, which is much larger than the value of internal birefringence perturbation $\beta_i \approx 0.1$ for $\delta n \approx 1\times10^{-7}$. The corresponding azimuth angle to the rotated major axis and ellipticity angle along the propagation direction is then:

$$\phi \approx \theta - \xi z \tag{3.27}$$

$$\psi \cong 0 \tag{3.28}$$

In laboratory frame, $\phi = \theta$. Together with (3.28), it indicates that any linear polarization state is preserved as long as the spin rate is substantially larger than the internal birefringence and the spun CCC fiber is indeed a low birefringent (Lo-Bi) fiber, which naturally preserves any polarization states injected under no external perturbations.

Another main characteristic of CCC fiber that distinguish its polarization preservation performance from that of conventional spun LMA fibers is the robust and pure single mode guidance within the fiber. As introduced in section 3.1.1, the HOM scattering in LMA fiber degrades the polarization preservation since the scatterred modes have a random polarization orientaion and propagating at a different velocity as fundamental mode. In CCC fiber, with the scattered HOM coupled into and undergone high loss in the side core, no mixing of the modes would happen at the output end of the fiber as long as the propagation length is long enough for HOM suppresion, which is usually around 1m for CCC fibers.

Experimental characterization of internal birefringence with CCC fiberInformation on all the tested fibers in this chapter is summarized in Table. 3.1. Commercialized standard single mode fiber (HI-1060, Corning) and 10μm LMA fiber (LMA-GDF-10/400, Nufern) were tested to characterize the geometrical deformation induced birefringence. The 35μm core CCC fiber and two LMA fiber from the same preform as this CCC fiber but without side core structure were compared to further explore the influence of spining and single mode operation on CCC fiber internal birefringence. The 55μm core and 500μm cladding CCC fiber is tested to study the effect of large cladding on external perturbation.

Table 3.1: Table 3.1 Parameters of fiber used in polarization transmission test for birefringence characterizations. * Fibers from the same preform

Fibers	Parameters		
	Core Size	Cladding Size	Spin Period
HI-1060	6μm	125μm	N/A
LMA 10/400	10μm	400μm	N/A
LMA 35/250*	35μm	250μm	N/A
LMA 35/250 spin*	35μm	250μm	6mm
CCC 35/250*	35μm	250μm	6mm
CCC 55/500	55μm	500μm	6mm

To characterize the internal birefringence with CCC fiber, polarization preservation performance was tested with the setup shown in Fig. 3.9. Comparison of the measurement results with several non-Hi-Bi fibers was also done to further verify the origin of CCC internal birefringence.

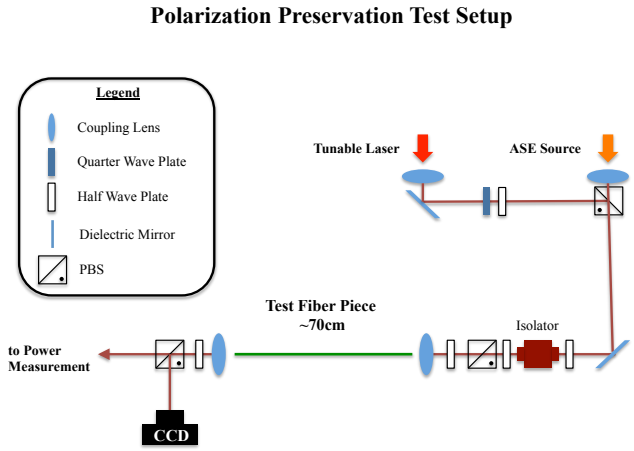

Figure 3.9: Illustration of setup for polarization preservation test. For fibers without robust single mode output, a standard non-PM single mode fiber was used to strip off the HOM in power measurement.

In the internal birefringence characterizations, fiber lengths in use are all around 70cm so that the randomness of the geometrical deformation is not strong enough to interfere with the measurements. Also, the fiber is straight mounted to avoid any possible external perturbations. The tests were carried out for standard single mode fiber, 10μm LMA fiber and the 35μm CCC fiber, since for all the other large core fibers, multi-modes are guided with such short length in a

straigh fiber, and the output beam has a strong polarization beating effects with narrow linewidth source seeded. For 35μm CCC fiber, the polarization extinction ratio (PER) was calculated with the measurement after a non-PM standard single mode fiber, since there is still residual of HOM output with this short length. The impact of robust single mode operation on polarization preservation would be testified later with a longer piece of the same CCC fiber, which would be discussed after the next section.

For arbitrary elliptical polarization state at propagating distance z, it could be described by an equation of polarization ellipse as [16]:

$$\frac{E_x^2(z)}{E_{0x}^2}+\frac{E_y^2(z)}{E_{0y}^2}-\frac{2E_x(z)E_y(z)}{E_{0x}E_{0y}}\cos\zeta=\sin^2\xi \tag{3.29}$$

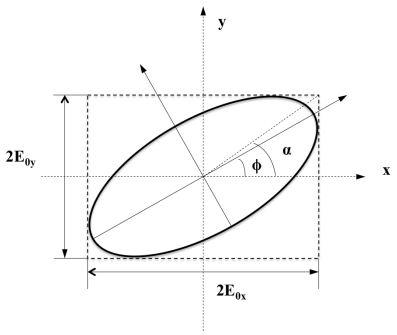

Figure 3.10: Illustration of polarization ellipse.

whereE_{0x}, E_{0y} are as shown in Fig. 3.10. $E_x(z), E_y(z)$ are magnitude of polarization components at z. ζ is the phase difference between them. α is auxiliary angle. Therefore, polarization characteristics such as azimuth angle ϕ(z), and and ellipticity angle ψ(z) are given by:

$$\begin{cases}\tan\big(2\phi(z)\big)=\tan(2\alpha)\cos\zeta(z)\\ \sin\big(2\psi(z)\big)=\sin(2\alpha)\sin\zeta(z)\end{cases} \tag{3.30}$$

with $\phi(z)$ and $\psi(z)$ known from the measurement, one can compute out the value for α and most importantly, the phase difference between the two polarization components ζ, which is euals to $\delta n \bullet k_0$ and leads to estimation of birefringence.

The test were carried out with straightly mounted fiber piece. Linear polarization state from narrow linewidth tunable laser source is injected into the fiber with the azimuth angle varies from 0 to 180^{o}. With recording the output PER and azimuth angle and follwiing Eqn. (3.30) one can get the value of ζ. However, one also need to keep in mind that the output PER value varies periodically evergy quarter of polarization beating length, which is $L_p/4 = \lambda/4\delta n$. Thus, for fiber length larger than quarter of its beating length, this calculation would underestimate the birefringence. To solve this ambiguity problem, a second measurement needs to be done with a different wavelength. In this way, one can get the relative spectral phase differece and:

$$\delta n = \frac{\lambda_1\lambda_2(\delta_{\lambda 1}-\delta_{\lambda 2})}{2\pi L(\lambda_2-\lambda_1)} \tag{3.31}$$

In fig. 3.11, the spectral polarization transmission measurement results of the Hi-1060 and 10/400 LMA fiber are shown. Using Eqn. (3.30) and (3.31), the internal birefringence of these two fibers are about 6×10^{-7} and 2.5×10^{-7} respectively. Assuming that the gemetrical deformation induced linear birefringence is the main origin for these fibers and following calculation for geometrical deformation induced birefringence in section 3.1.1, the core non-circularity of the Hi-1060 and 10/400 LMA fiber are roughly 0.7% and 0.6% respectively, assuming that is the only birefringence perturbation mechanism within the fiber, which agrees with commercial specification of a roughly 0.5% non-circularity for the core of a 10/130 fiber.

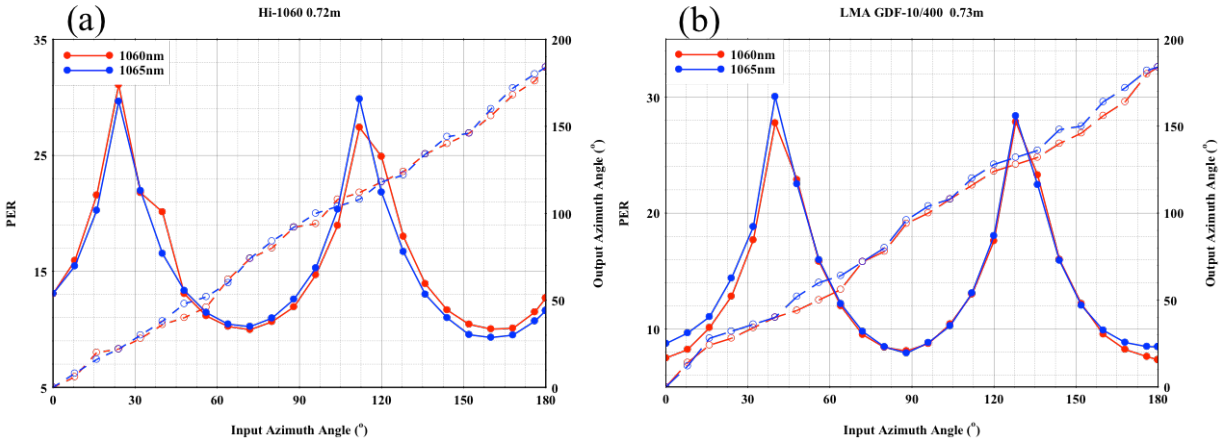

Figure 3.11: Spectral polarization transmission measurement for (a) Hi-1060 single mode fiber and (b) 10/400LMA fiber. The blue curves are measurements with wavelength at 1065nm, and the red ones are of 1060nm. Solid lines represent PER of the output polarization; the dashed ones are the output azimuth angle.

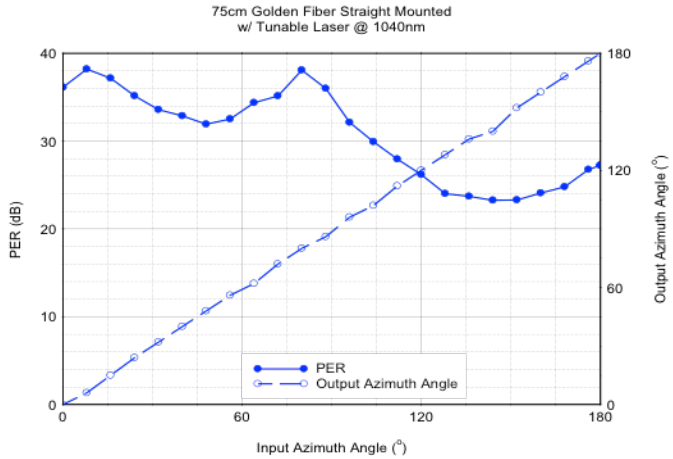

Figure 3.12: Polarization transmission measurements for 35μm CCC fiber with 1040nm narrow linewidth source; The solid curves are PER measurements; the dashed ones are output azimuth angle.

Fig. 3.12 shows the polarization transmission measurements with 35μm CCC fiber. PER of output polarization from CCC fiber with 1040nm narrow linewidth source is above 22dB for all input linear polarization states. The asymmetric PER value over 180° of input azimuth angle is speculated to be from the residual modal scattering effect coupled into single mode fiber. Due to the measuring up-limitations of the polarization optics, it is impossible to determine the actual birefringence related to PER over 20dB. However, the preservation input linear polarization with

various azimuth angle indicates that CCC fiber has extremely low internal birefringence than what is predicted with the geomtrical deformation and further validates that the spinning process largely reduce the overall intrinsic birefringence to negiligible level.

3.2.2 Effects of external perturbations on CCC fibers

Although Lo-Bi fiber also preserves polarization states, it was not considered as a appropriate technique for polarization maintaning systems, due to its sensitivity to external perturbations. To evaluate the capability of polarization maintenance of CCC fibers, the effects of external perturbations such as bending, twisting and stress need to be investigated.

In real high power fiber laser systems, when fiber is coiled, both bending induced linear birefringence and twisting induced circular birefringence coexist, according to previous discussion. Assuming a coiling radius of 20cm, which is mostly used for 30-50μm CCC fiber, the general bending induced birefringences, i.e. from freely bending, combination of freely bending and wounding with axial force and beding induced twisting, are ploted in Fig. 3.13. The kink induced birefringence is not included here, since it is a random local purturbation.

As shown in Fig. 3.13, the twisting circular birefringence is negligible when the fiber is wounded around a drum with axial force, but rather comparable to the linear birefringence from freely bending. To explore the influence of these purturbations, polarization evolution along the fiber was simulated following couple mode theory solution for a fiber size of 250μm with assumption that the bending is over the whole fiber. Although in practical systems, this is not true, the polarization mode does not change while propagating along straight CCC fiber due to its Lo-Bi nature.

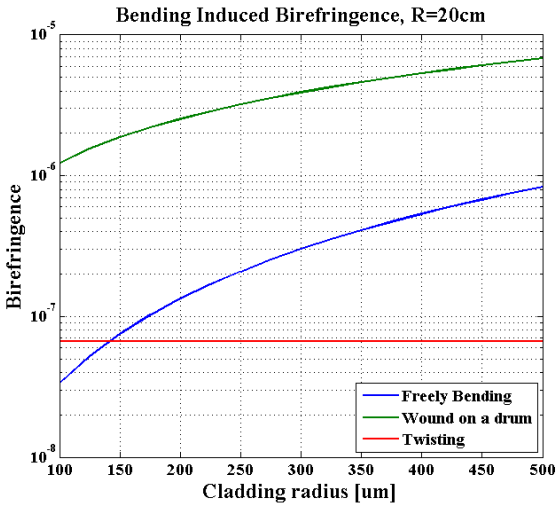

Figure 3.13: Bending induced birefringence with a coiling radius of 20cm.

In Figure 3.14, polarization evolution along a piece of 250μm low birefringent fiber, which is either (a) freely bent with a 20cm radius or (b) wound arong a drum with 20cm radius, is represented on Poincaré sphere. It shows that when fiber is freely coiled and the linear bending birefringence and twisting circular birefringence are comparable, the eigen polarization state is no longer linear. And thus no preservation for linear polarization along the fiber. Meanwhile, the total birefringence is still close to linear, when the fiber is wound around a drum, and it is still possible to maintain linear polarization along the fast or slow axis of bending birefringence, as long as the coiling diameter is sufficiently large.

It is worth noting that for freely coiling case, one will always able to achieve a linear polarizaion output with certain azimuth angle of the linear polarization input. In other words, for freely coiled CCC fiber, linear polarization state can always be reproduced at the output end of the fiber without dependence on the fiber length. And this is the reason why we observed good polarization preservation with coiled CCC fibers in practical amplifier systems. Since in most applications of high power fiber amplifiers, the preservation over whole fiber length is not

indispensable, this reproduction of linear polarization would still be acceptable for polarization maintaning systems as long as external stress perturbation is negligible.

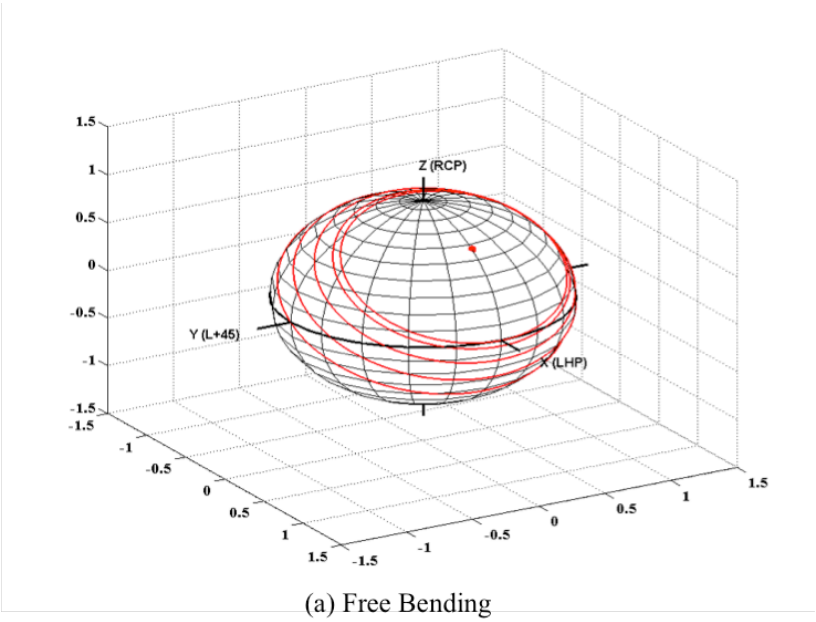

(a) Free Bending

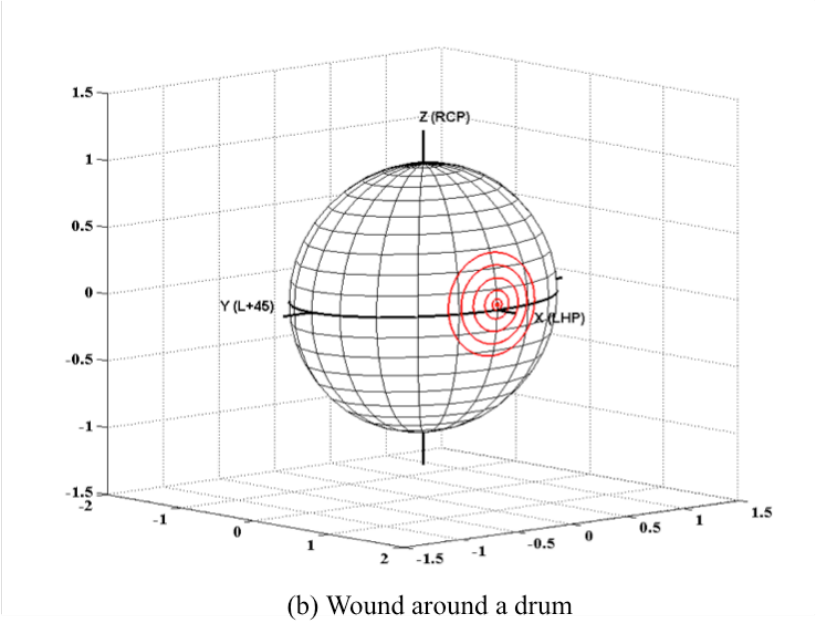

(b) Wound around a drum

Figure 3.14: Poincaré sphere representation of polarization mode evolution along the 250μm fiber when it is: (a) freely coiled, (b) wound around a drum with axial force. The coiling radius is 20cm for both case.

One of the significance of this bending induced linear birefringence is that, in practical systems, these effects are globally applied to CCC fiber and behave as main origin of polarization effect for the low-birefringent CCC fiber. Hence, one can utilize these effect as a control approach for the polarization performance in CCC fibers. Moreover, as shown in Fig. 3.13, the bending induced birefringence scales up with increasing fiber size. Also recall that the external stress induced birefringence scales inversely with increasing of the fibersize as depicted in Fig. 3.3, for fiber with larger cladding size, the less sensitiveness to external stress perturbation would it experience when it is coiling packaged. For example, according to calculation results in Fig.3.3 and 3.14, for 400μm CCC fiber wound around a drum with 20cm radius, the total bending linear birefringence is over 2×10^{-6}, while the linear birefringence per unit line force is about 2×10^{-8}/(N/m). And in real systems, the ramdonly localized external stress perturbation on a fiber is usually less then few Newtons per meter, therefore, the stability of polarization preservation with a bent structure of the fiber is enabled.

3.2.3 Experimental characterization of external birefringence of CCC fiber

Fristly, with longer piece of fiber under test, the effect of robust single modeness on polarization property of the fiber is demonstrated. This time, polarization transmission measurements were done with 35μm CCC fibers and the LMA fibers from same preform with a coiling diameter of 35cm. The testing length for CCC and unspun LMA fiber were both 5m, while for the spun LMA fiber it was 2.5m long. For all the tested fibers, PER of output polarization measured directly from the test fiber was compared to that from the power striped with a non-PM standard single mode fiber (SMF). With unspun LMA fiber, PER output with a deliberate misaligned mode excitation was also measured with SMF fiber output. As shown in Fig. 3.15, the difference between measurements from direct and SMF striped output power from

CCC fiber is negligible, However, for LMA fibers, maximum PER of the total output power is much less than that with the fundamental mode. Furthermore, the degradation of PER maximum with worse single mode excitation of unpun LMA in Fig. 3.15(c), clearly shows the strong dependence of polarization linearity on the modal quality of the beam.

(a)

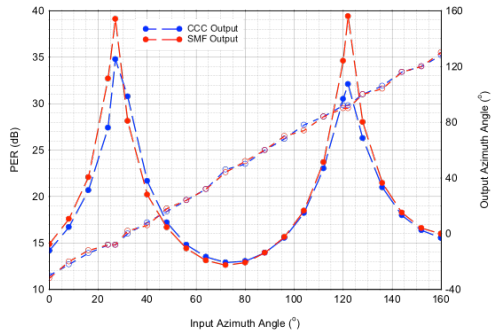

(b)

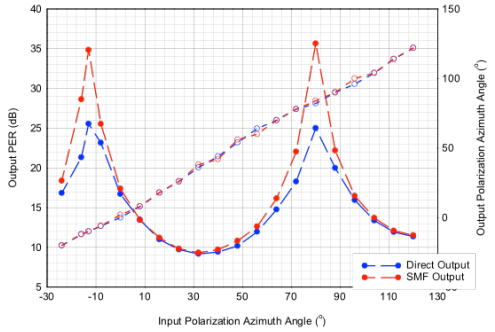

(c)

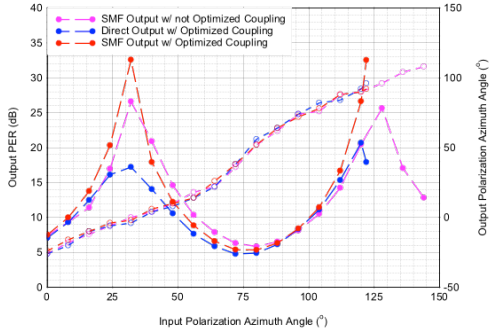

Figure 3.15: Polarization transmission measurement with:(a) 35µmCCC fiber; (b) 35µm spun LMA fiber, (c) 35µm unspun LMA fiber.

One key requirement of polarization maintaning system is the output polarization states do not change with the external perturbation. And this is realized in two perspects: i) the output PER does not degrades, ii) the azimuth angle of output linear polarization does not change. The external perturbations in consideration here, are usually the random lateral aymetric stress and temperature change, since bending and twisting are fixed situation during the packaging process and would not change during the operation. For spun fibers, since the overall internal birefringence perturbation is zero due to the fast spinning or preform, the effect of temperature dependent thermal expansion coefficient would be also averaged out in a same maner. Therefore, polarization performance from CCC fiber is immune to temperature variance, opposite to that of conventional Hi-Bi fibers [62].

(a)

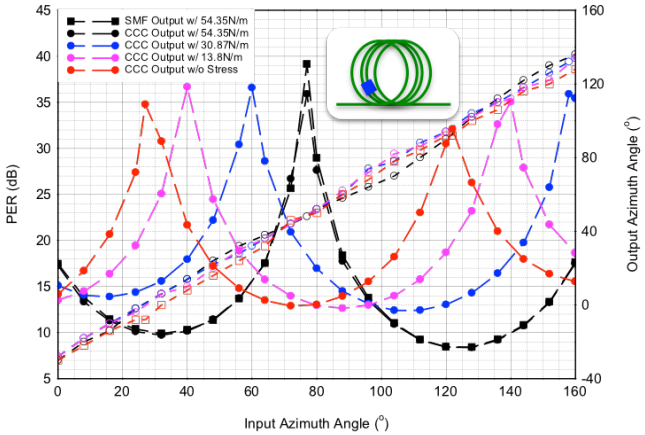

(b)

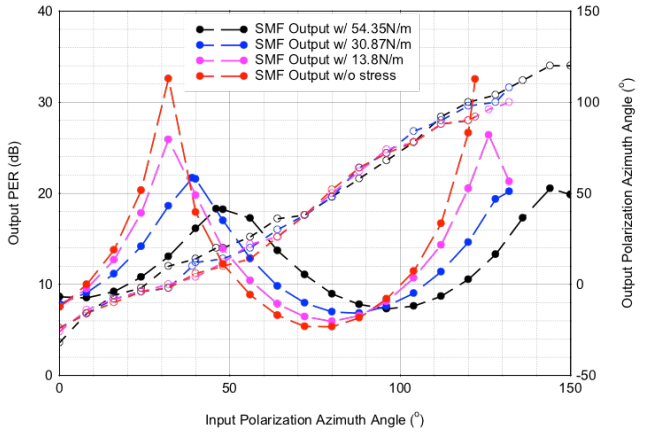

(c)

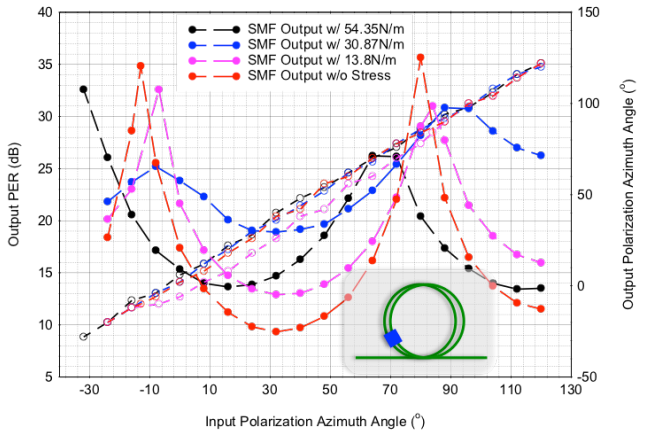

Figure 3.16: Polarization transmission measurement with: (a) 35μm CCC fiber; (b) 35 unspun LMA fiber, (c) 35μm spun LMA fiber. Inserts are illustration of experiment setup.

Fig 3.16 show the experimental test results of 5m pieces of 35μm CCC fiber and unpsun LMA fiber as well as a 2.5m piece of spun LMA respectively. Both 5m long fibers are coiled to 4 rounds with about 36cm diameter and the spun LMA was coiled to 2 turns with around 35cm coiling diameter. Few metal bulk with various weights were layed onto rough 8:00 position of the two coils of the fiber, for 5m pieces, those are the two coils in the middle as shown in the insert illustrations. All the PER measurement for CCC fibers are from the direct output power, while for LMA fibers, HOMs filltering with SMF was employed. The maiximum PER of output polarization from CCC fiber remained at over 35dB with stress up to 54.35N/m. However for spun LMA fibers the maximum PER value varies in a range from 25dB to 35dB. One need to keep in mind that these measurements with LMA fiber are all from a stripped output from single mode fiber. The real PER from direct measurement in practical system would be much lower with multimode output. And worst of all, the maximum PER output from spun LMA fiber kept degrading from an initial value of 32dB to about 18dB. The degradation of maximum PER from spun LMA is due to the HOMs excited within the fiber due to stress perturbation, while for unspun LMA fiber, this droping is the combination result from its resiual intrinsic birefringence and HOMs guidance. From comparison between these reults, it manifests again that the linear polarization reproduction from CCC fiber is due to both its Lo-Bi nature as well as the robust single mode performance. However, the azimuth angle of output polarization from all three fiber shifts due to the external stress. The question now is that whether one can find a way to enhance the insensitivity of azimuth angle of output linear polarization of CCC fiber.

One natural path would be to increase the fiber size. As aforementioned and shown in Fig. 3.3, the stress bifrefingence is inversely dependent on the fiber size, and thus influence of same amount of stress would be reduced. Fig. 3.17 presents the similar polarization transimission measurement with a 2m long 55μm CCC fiber with 500μm outer cladding. the fiber is coiled to one round with 40cm in diameter. The metal bulk applied to the same 8:00 position on the fiber, with short piece of fiber with same dimention to support the bulk, so that the stress distribution per unit length is same as the arrangement in tests with 35μm fibers. Both maximum PER and its corresponding azimuth angle is preserved for stress up to 100N/m.

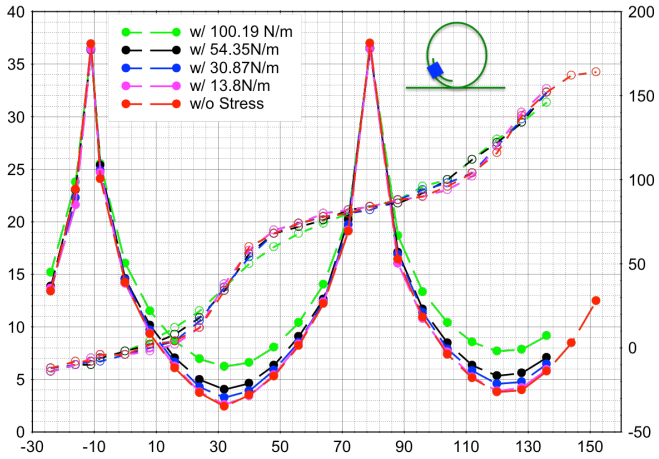

Figure 3.17: Polarization transmission measurement with 2m long 55μm CCC fiber with 400μm cladding

Simulation results of 5m 35μm CCC and 2m 55μm under respective test conditions same as these two tests are shown in Fig. 3.16(a) and 3.18, based on couple mode theory. Comparing the two calculation results with the experimental measurements, it performance of 35μm CCC fiber is different from the prediction, while that of 55μm CCC fiber agrees well. It is not fully understood that where this discrepency of experimental measurement and theoretical prediction on performance of 35μm CCC fiber comes from yet. However, one suspicion is that the local internal birefringence induced by the asymmetric lateral stress from single side core may

interfere with the local external lateral stress. Further exploration on this problem is still undergoing.

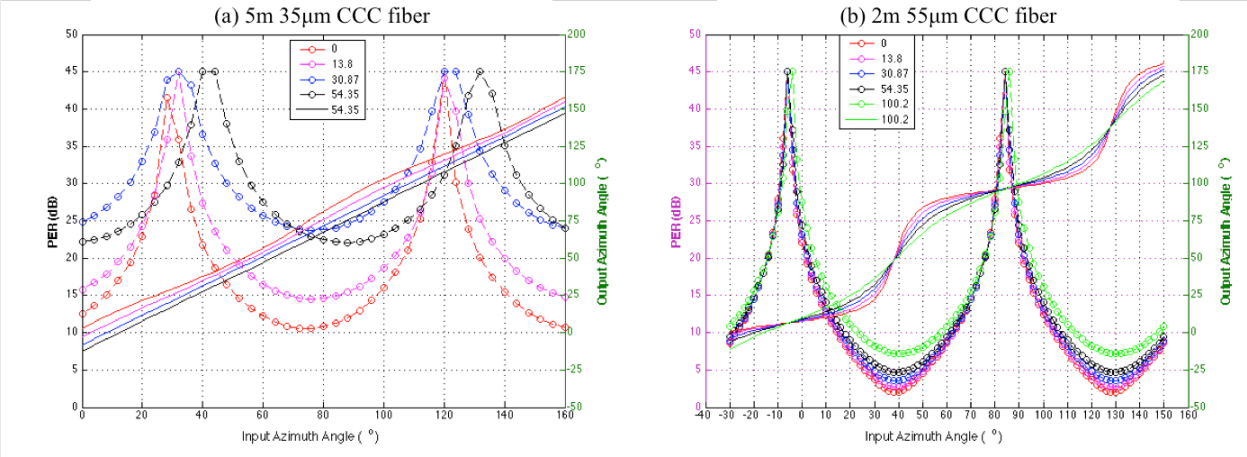

Figure 3.18; Calculated output PER and azimuth angle for (a) 5m 35μm CCC fiber coiled with 4 rounds, (b) 2m 55μm CCC fiber coiled to 1 round, with various stress applied. The simulation parameters are following the parameters in experimens, which were shown in Fig. 3.16 (a) and 3.17.

3.3 Approaches to enhance polarization preservation of CCC fibers

As analyzed and demonstrated in previous sections, the conventional concept of polarization maintenance no longer applies for CCC fiber. And with coiling fiber for practical fiber laser system packaging, CCC fiber is no longer working as a Lo-Bi fiber either. However, all time polarization maintenance within the fiber is not mandatory for most high power fiber laser systems, CCC fiber can still well fit for the requirements of a PM power system as long as:

1) Linear polarization state could be reproduced at output;
2) The azimuth angle of this output linear polarization is insensitive to external stress perturbations.

The first requirement is naturally satisfied with coiling packaging of CCC fiber as illustrated in Fig. 3.10. However, the second one is not fulfilled without extra strategy taken as demonstrated in Fig. 3.16 (a). Since the dependence of stress birefringence and fiber size is a

inversely linear relation, the increasing of fiber size is not a sufficient method to enhance the insensitivity to external stress perturbation.

Since there is a combination of linear and circular birefringence coexisting in the fiber when it is packaged with coiling, a seemingly reasonable solution would thus be either increasing the bending linear birefringence, or strengthen the twisting circular birefringence so that the effect of external stress would be negligible.

To raise the linear birefringence from bending, several ways could be exploited based on the analysis in section 3.1.1. Firstly, one could shrink the coiling radius to enhance the birefringence related. According to Eqn. (3.5-6) the bending birefringence has a quadratic dependence on the inverse of coiling radius and the wounding birefringence is inversely proportional to it. In Fig. 3.18, the birefringence and coiling radius relations for fiber with 400μm cladding is drawn. And with extremely small coiling size, one may achieving close to 1×10^{-5} linear birefringence either by freely bending or wounding of the fiber. However, for fiber with large core size, this is not practical, a coiling radius larger than 15cm is usually applied to avoiding extra fundamental mode loss in the core. Therefore, to have dominant linear birefringence from bending process, wounding the fiber around a drum would be a better choice. And in that way, one can usually get linear birefringence around 2×10^{-6}.

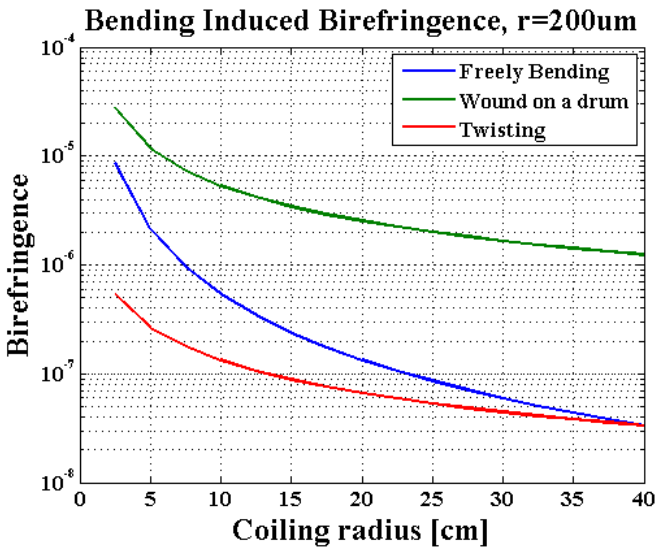

Figure 3.19: Bending induced birefringence versus coiling radius for a 400μm fiber.

To strengthen the circular birefringence, extra twisting is needed to apply on the fiber. Following Eqn. (3.8), the circular birefringence induced by twisting is about 1.55×10^{-7} with each turn per meter. Therefore to get similar magnitude of linear birefringence from wounding with 400μm fiber around a drum, about 13 turns /m is required.

Fig. 3.19 shows the calculated PER of output polarization from a strongly twisted freely coiled fiber based on couple mode theory. The output PER is calculated for polarization at azimuth angle equal to the predicted rotated angle by twisting optic activity. The simulation was done for two 2.5m long fibers with sizes: 250μm and 400μm, which are the sizes of commonly used large core fibers. For 250μm fiber, a coiling radius of 15cm is assumed, and for 400μm fiber, 20cm-coiling radius fits the practical situation. The stress is applied to the whole fiber with a 45^{o} angle to the bending plane, which is the direction for largest decoupling with the bending linear birefringence. In practical situation, external stress perturbation is usually applied with random direction and length. However, this simulation still provides a good prediction as for the worst perturbed case. As marked by the dashed curves where the output PER is 20dB, for fiber with larger size and coiled to larger radius, the stress perturbation influence is reduced. For the

400μm fiber with a twisting rate at 15 turns/m, the insensitiveness of output polarization to the external stress could be maintained to roughly 10N/m.

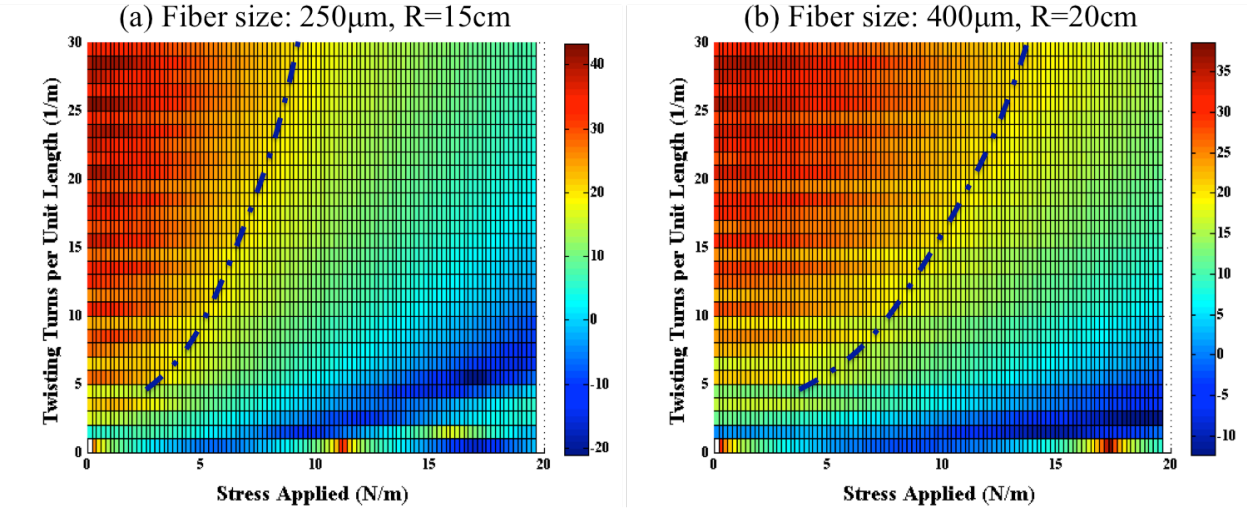

Figure 3.20: Simulation of output PER dependence on fiber twisting rate and external stress perturbation with : a) 250μm fiber coiled to 15cm radius and b) 400μm fiber coiled to 20cm radius. The dashed line indicates roughly where 20dB PER is.

Since the twisting rate is not related to the fiber size and coiling radius, but bending birefringence are, one can utilize these two approaches for different fiber parameters. For example, when fiber size is small, coiling size could be reduced, and the wounding linear birefringence is larger and consequently, better polarization stability is with external stress perturbation. But the twisting rate required to provide same stability would be also increase and may be practically unachievable. Meanwhile, for fiber with larger size and coiling to larger radius, twisting the fiber to produce strong circular birefringence would be a better solution, since at this time, the wounding birefringence is reduced by a similar rate as for the stress birefringence.

Another feature distinguishing these two methods is that while strong twisting of the fiber actually makes it a circular birefringent fiber, with circular polarizations as its eigenmoeds, wounding the fiber around the drum makes it similar to Hi-Bi fiber, with which linear

polarization is maintained over the whole fiber. Therefore, if the system is for applications which requires all time maintenance of polarization such as four-wave-mixing, wounding around the drum is the better choice. On the other hand, for applications, which prefer nonlinear effect suppression, such as SBS and SRS suppression, the twisting approach is perfectly fitted, since it can provide a linear polarization output while double the threshold for those nonlinear effects.

3.4 Conclusion

In this Chapter, polarization preservation in CCC fiber is explored theoretically and experimentally. First, we show that internal birefringence is negligibly low in CCC fibers due to two factors: (1) effects of local stress and geometrical-deformation induced birefringence are eliminated by the spun nature of CCC fibers, which are drawn from a rapidly rotating preform during their fabrication, and (2) effects of modal scattering are also eliminated due to the effectively single-mode performance of CCC fiber core. Second, large cladding size associated with large core CCC fibers significantly reduces fiber sensitivity to external perturbations to a degree that effects of the perturbations occurring due to packaging imperfections (such as random lateral stresses, etc.) become negligible. Furthermore, in practical integrated laser systems containing coiled fibers, fiber bending and the corresponding twisting inevitably occurs, which induces linear and circular birefringence distributed along fiber length. Wounding fiber around a drum provides linear birefringence of approximately 10^{-6}, which enables linear polarization eigenmodes perpendicular to or along the wounding axis over the coiled fiber. Twisting fiber at a rate of approximately 10-20 turns/m creates circular polarization of approximately 10^{-6}. Both effects can be exploited as additional means for polarization preservation in CCC fibers.

Chapter 4

Narrow linewidth CCC fiber amplifier for CW combining laser array

4.1 Introduction

Nowadays, due to their compact and robust structures, superior thermal management properties, near diffraction-limited beam quality, and high conversion efficiencies, CW fiber lasers and amplifiers play an important role in high power systems for various potential applications such as gravitational wave detection, LIDAR, material processing and etc. Few kW fiber lasers with diffraction-limited beams are now commercially available [88]. And 10kW single mode fiber lasers are already realities [24]. However, one single channel is not sufficient to achieve over 100kW practical laser systems due to limitations such as nonlinear effects, bulk silica damage and thermal damage. To overcome this bottleneck, coherent combining of continuous-wave high power fiber lasers is currently considered to be the most promising path for further power scaling.

First of all, to have all the output beams from individual amplification channels overlapped well with each other and to achieve a high brightness combined beam with good combining efficiency, beam with single transverse spatial mode quality from each channel is in need. Moreover, the stability of combined beam is also important for practical applications, thus robust polarization maintenance of individual channel is also required. Furthermore, building

coherent fiber array would require each fiber amplifier output to achieve accurate phasing and have mutual coherence. Thus, very narrow linewidth spectrum of output beam is highly demanded. Spectral bandwidth of each channel should be broad enough to avoid significant nonlinearity appearance, which would be discussed in the next section, while also be within certain range such that the path lengths of each channel could be matched within coherence length. For combinable fiber based master oscillator power amplifiers (MOPA), to have adjustable mismatch path length between each channels, no more than 10 GHz linewidth is acceptable [44].

4.2 SBS mitigation

Stimulated Brillouin Scattering (SBS) is the most significant hindering factor of the power scalability of coherent combining system components operating within narrow linewidth. SBS is induced by interaction between optical field and acoustic phonons in the fiber, driven through the process of electrostriction [31]. With certain spectral power density of optical field, acoustic wave is generated and modulated into a moving index grating in the fiber core. As a result, small portion of amplified signal would be deflected by this grating and backward propagated along the fiber, which will then compete with the signal light for the gain in the amplifier and further be detrimental for the previous amplification stages. The backscattered Brillouin wave is frequency downshifted due to the Doppler shift of the moving acoustic grating. This Brillouin shift is then calculated by [31]

$$\upsilon_B = 2n_p v_A/\lambda_p \tag{4.1}$$

where n_p is the refractive index at wavelength λ_p, and v_A is acoustic wave velocity in fiber core. For silica fibers $n_p = 1.45, v_A = 5.96\text{km/s}$, with wavelength λ_p around 1μm, $\upsilon_B \approx 16\text{GHz}$.

The gain of SBS depends on both the bandwidth of amplified signal $\Delta\upsilon_s$ and its own gain spectrum $\Delta\upsilon_B$, as shown in (4.2). The SBS gain bandwidth $\Delta\upsilon_B$ is related to the phonon lifetime, which is usually 50~100MHz in silica fibers. g_{B0} is the peak value of Brillouin gain at $\upsilon = \upsilon_B$, which is usually about 5×10^{-11} W/m for fused silica.

$$\tilde{g}_B(\Delta\upsilon_s) = \frac{\Delta\upsilon_B}{\Delta\upsilon_B+\Delta\upsilon_s} g_{B0} \tag{4.2}$$

The development of SBS is governed by coupled equations and could be solved analytically under assumption that pump wave depletion is negligible. And the critical power P_{cr} for the Brillouin threshold is given by [96]

$$P_{cr} = \frac{\chi A_{eff}}{\tilde{g}_B(\Delta\upsilon_s)\cdot L_{eff}} \tag{4.3}$$

where A_{eff} is the effective mode area, L_{eff} is effective fiber length and χ is a numerical constant related to all the other parameters in this formula. For conventional single mode fiber MOPA, χ is approximately 21 and the critical power could be calculated out as tens of watts, which are insufficient for high power beam combining system seeking for hundreds kilowatts power output. As a result, methods to mitigate SBS are in demand for further power scaling.

According to the critical power dependence on fiber length, mode area and Brillouin gain coefficient, methods for SBS mitigation fall into three main categories. Firstly, one can enlarge the effective mode area of fiber to increase the critical power. Another method is to increase doping concentration in fiber core and thus shorten the fiber length in need for amplification to raise the SBS threshold. Furthermore, lowering Brillouin gain can also raise the critical power. One of the approaches to achieve this goal is by utilizing thermal gradient in counter-pumped fiber amplifier. In this way, frequency shift associated with Brillouin scattering along the fiber would be changed and it further decouples SBS gain between sections of fiber at different

temperature. Another way is to reduce the overlap between optical and acoustic modes in the fiber by choosing refractive index profile or selecting certain dopants in fiber to spatially separate the two modes or create an acoustic anti-guide. Additionally, one can also broaden the bandwidth of signal to larger than Brillouin gain bandwidth so that SBS gain if reduced and threshold is thus raised. However, this improvement is at the cost of losing coherence of the beam as we stated earlier.

With approaches for SBS suppression discussed above or the combination of these approaches, up to 800W single frequency fiber MOPA output was achieved [89-92, 101], and kW level fiber MOPA output with narrow bandwidth over GHz [94-96] was also realized as shown in figure 4.1.. Furthermore, kilowatt scale coherent combining has been realized by building eight nearly 500W single frequency fiber MOPAs in a filled aperture [36].

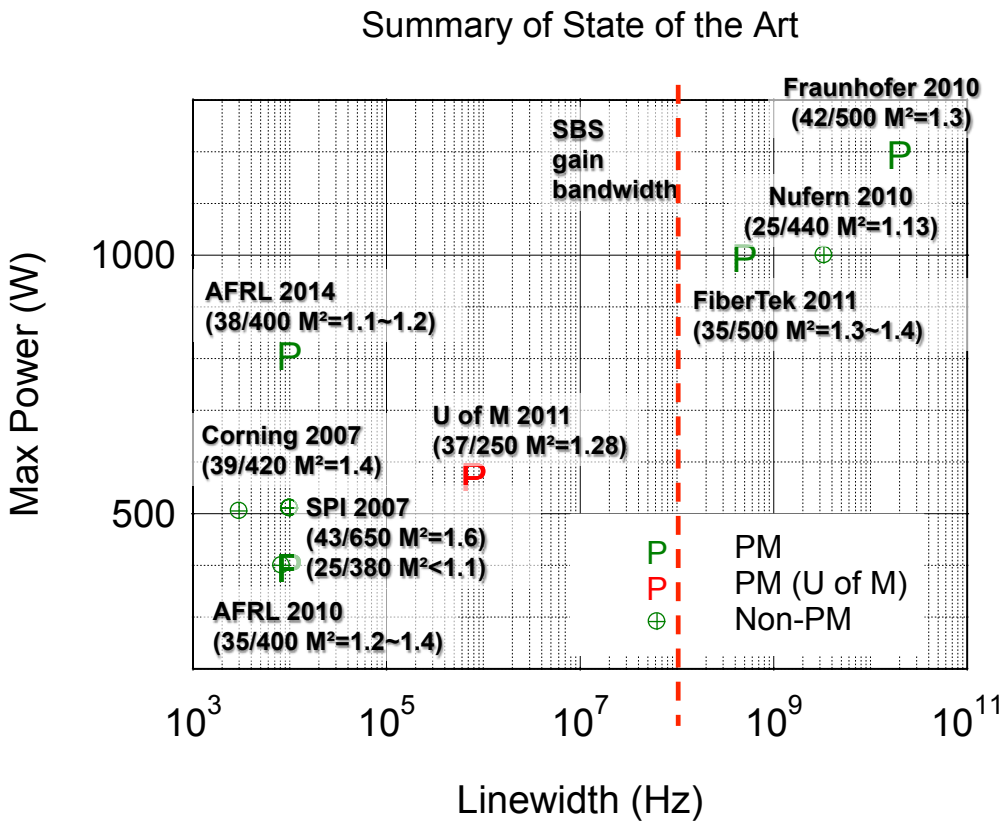

Figure 4.1: State of the art of fiber based CW power amplification with single frequency and narrow linewidth centered at 1064nm. The cross-circle marks are records with no polarization maintenance. P marks represents records with polarization maintenance.

4.3 37μm CCC single frequency amplifier scalability and SBS threshold analysis

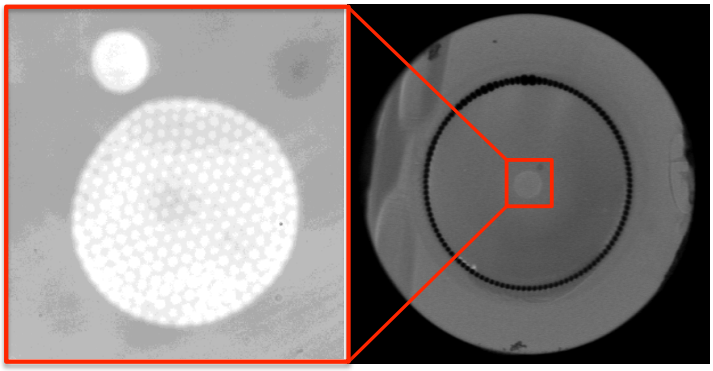

Figure 4.2: Microscopic image of 37μm Yb-doped air-clad CCC fiber with focus on the core area and the whole fiber transection.

To achieve high power CW single frequency amplification, one piece of 37μm Yb-doped air-clad CCC fiber with high absorption is chosen as the main gain medium [56]. Microscopic

image of this fiber is shown in Fig.4.2. And detailed information of this fiber is also listed in Table 4.1. As discussed in Chap 2, the air-hole structure in the cladding could improve the thermal management of fiber coating and thus facilitate high pumping levels for relatively short fiber lengths. Furthermore, the large mode area and high absorption enabled short effective fiber length could raise SBS threshold as analyzed in section 4.2.

Table 4.1: Specification of 37μm Yb-doped air-clad CCC fiber.

Central Core		Side Core		Inner Cladding		Outer Cladding		Helix Period (mm)	Absorption @ 975nm (dB/m)
MFD (μm)	N.A.	Dia. (μm)	N.A.	Dia. (μm)	N.A.	Dia. (μm)	N.A.		
30	0.069	9.8	0.089	260	>0.6	440	0.46	6	8

With these fiber parameters know, we could estimate critical power lever for SBS onset following Eqn. (4.3). For large mode area fiber in use, the numerical factor χ need to be modified. In this case, χ is 32. Assuming the gain in the this amplifier would be around 20-30dB, and the predicted critical power would be inversely proportional to fiber length in use. From this calculation, the critical power for this 2.7m long air-clad CCC based MOPA system for single-frequency operation would be within 800W-1200W. This estimation is for case with seeding bandwidth within SBS gain bandwidth, i.e. 100MHz. It is also under the assumption that the fiber amplifier is counter-pumped. For co-pumping configuration, the expected SBS threshold would be about half of that for counter-pumping condition, due to longer effective fiber length.

4.4 Experiment and results

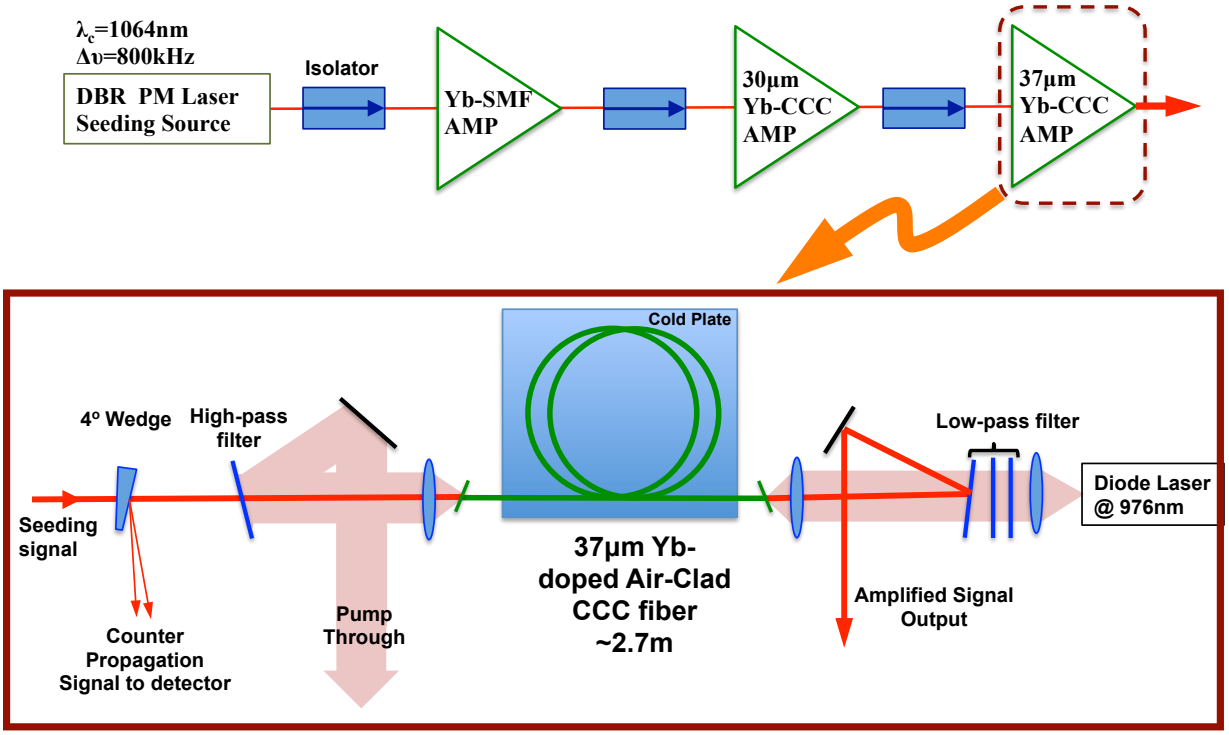

Figure 4.3: Illustration of experimental setup with counter pumping scheme.

A three-stages Yb-doped fiber based Master Oscillator Power Amplifier (MOPA) system was used to demonstrate single frequency CW power scaling (Fig. 4.3). The system was seeded with a single-frequency DBR laser diode (Sacher Lasertechnik TEC 50) operating at 1064nm with spectral bandwidth around 800kHz. The seeding signal then propagated through and was boosted by three Yb-doped polarization maintaining (PM) fiber amplifiers in chain. The two pre-amplifiers were based on standard single mode PM Panda fiber and double-clad CCC fiber respectively, while the final power amplification stage utilized a piece of 37μm airclad CCC fiber introduced in previous section.

The single frequency diode source provided about 40mW PM seeding power. It was then free space coupled into a single mode PM pre-amplifier co-pumped by a 600mW single mode laser diode at 976nm and generated 110mW power. The second pre-amplifier was based on 3m long Yb-doped double clad CCC fiber with 30um core, 250um cladding. It then followed a

counter-pumping scheme by a JENOPTIK fiber coupled CW diode laser to 30W. This stage provided 2.3W single transverse mode, linear polarized beam seeding the last and the main amplifier stage.

The main amplifier of this single frequency fiber MOPA consisted of an Yb-doped airclad CCC fiber introduced in the previous section. Both ends of the fiber were polished to 12^{o}. However due to air-hole structure in the cladding, the pump end, which was also the output end, was not endcaped but just fused for the polishing purpose as well as to avoid degradation of fiber by capillary action while maintaining the input pump power confined inside inner cladding of the fiber. The whole fiber was sandwiched in between two water-cooled cold plate to enhance heat dissipation. It was counter pumped by a combination of 3 fiber coupled high brightness laser diodes provided by Fraunhofer USA. Maximum output power of these three diodes are all above 400W and give the full power of 1.3kW. With selection for cooling temperature of chiller, which water-cools the diodes, wavelength of the pump reaches 976nm at full power to optimize conversion efficiency. The coupling fiber was standard high power delivery fiber with core size of 220μm and NA of 0.22. The output fiber ends of pump diodes were packaged tightly in a triangular shape with all the facets aligned to minimize pointing differences of the output beams. There were two dichroic filters mounted at both ends of the amplifier to separate signal and pump wave. A wedge with 4^{o} was inserted before the seeding end to pick up backscattering signal for SBS onset detecting purpose.

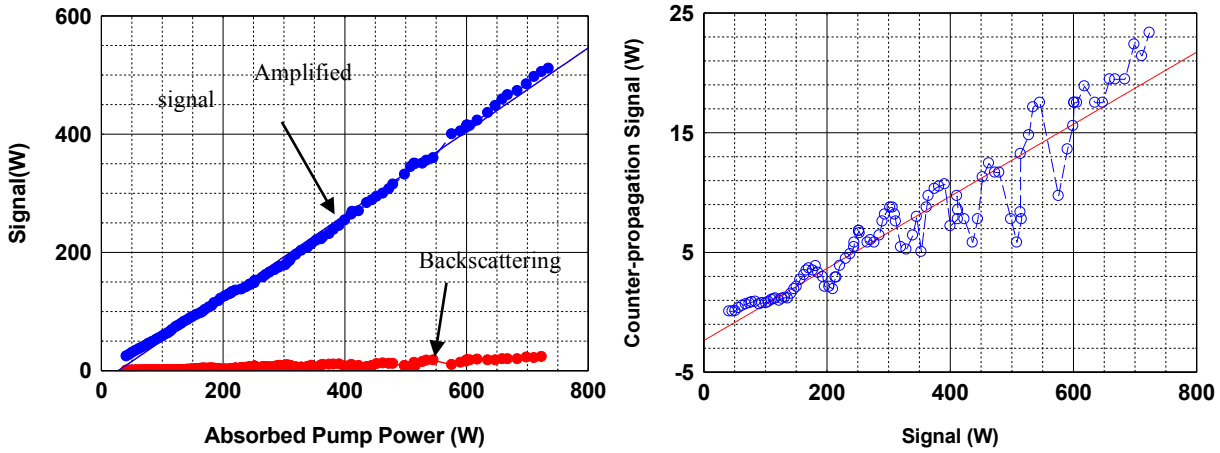

Figure 4.4: (a) Output signal power versus absorbed pump power from final amplification stage with counter-pumping configuration. The blue curve is the amplified single frequency signal. The red curve is the backscattering signal. (b) Backscattering signal power versus amplified single frequency signal power. The blue curve with circular mark is the experimental measurements, and the red solid curve represents the linear fitting curve, which shows no SBS onset during the amplification.

With the last amplifier stage pumped to 1kW and 700W absorbed at around 973nm, we got 511 W signal output with slope efficiency about 71% (Fig 4.4a) [59]. The backscattering signal power was linearly increased with that of forward propagating signal (Fig 4.4b). Ratio between these two signals remained roughly 4%. This stable counter-propagating signal to forwarding propagating signal ratio indicated that there was no SBS onset at this power level, and we did not reach the SBS threshold yet, which is consistent with our earlier estimation about the critical power around 600-900W of this MOPA system. The power scaling was stopped due to output end facet damaging.

Due to the bulk damage of un-endcaped fiber end, we then modified the final amplifier to co-pumping configuration as shown in Fig.4.5, at cost of lengthening effective fiber length and thus lowering SBS threshold. The CCC fiber based second pre-amplifier was replaced by a piece of 2.7m long higher doping Yb-doped CCC fiber with 35um core and 250um cladding to improve the efficiency of the system. The seeding power for the final stage after this CCC pre-

amplifier was then boosted to 5.5W. With co-pumping configuration, output end of CCC fiber at final stage was endcaped and angle polished to 12°. The final amplifier was then pumped to 1.1kW with 800W absorbed. At this pump level, 576 W single frequency CW output was achieved with a slope efficiency about 74% (Fig. 4.6a). A 3nm band-pass filter was added after the wedge picking up backscattering power to filter out ASE. As plotted in Fig. 4.6b, the backscattering signal power within 3nm bandwidth centered at 1064nm was linearly proportional to the amplified single frequency signal power. And the ratio between these two waves was about 0.025%, which confirms that no SBS onset exists at this power level since 0.1% reflectivity is usually defined as SBS onset threshold [101]. The power scaling was limited by the melting of un-endcaped pump end fiber facet.

The mode quality of the output beam was evaluated by knife-edge M2 measurements at about 30W and 100W power level (Fig. 4.7). And the M2 value of 1.19~1.28 showed the robustness of this single mode output. Polarization Extinction Ratio (PER) was also measured at up to 200W as shown in Fig.4.8. With PER maintained above 19dB with up to 200W output power exhibited good polarization preservation of this CCC fiber based MOPA system.

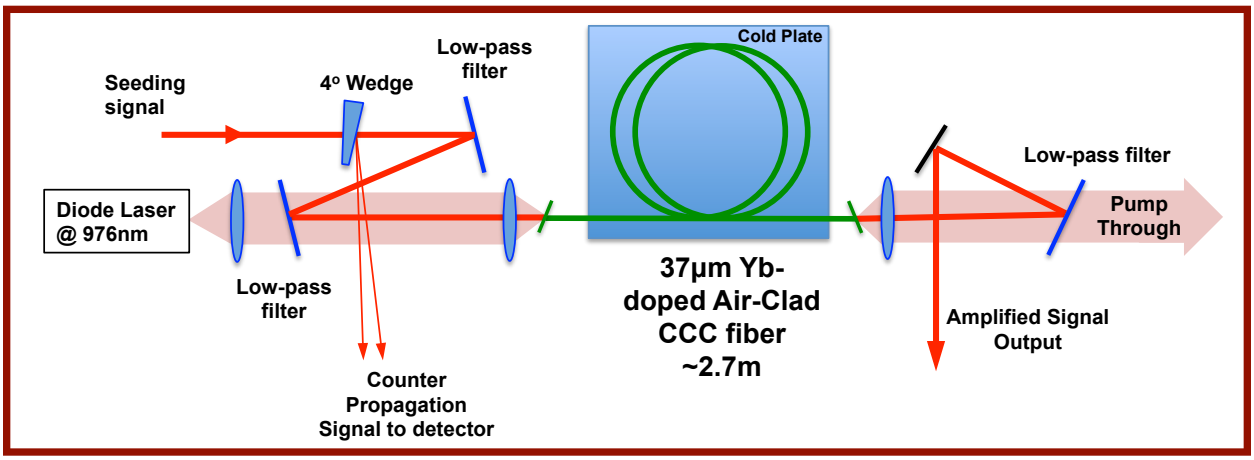

Figure 4.5: Illustration of setup for the final amplifier stage with co-pumping configuration.

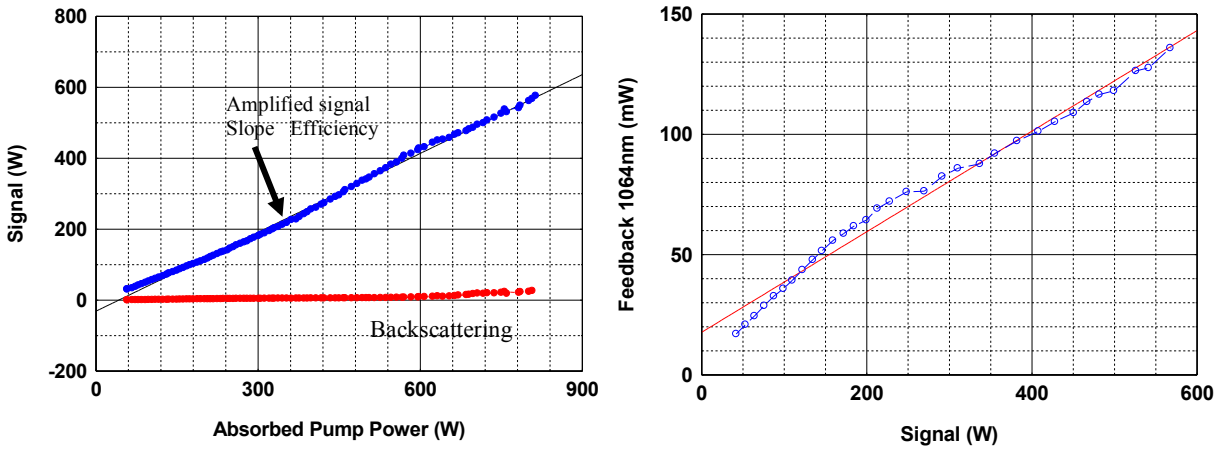

Figure 4.6: (a) Output signal power versus absorbed pump power from final amplification stage with co-pumping configuration. The blue curve is the amplified single frequency signal. The red curve is the backscattering signal. (b) Filtered backscattering signal power with 4nm band-pass filter centered at 1064nm versus amplified single frequency signal power. The blue curve with circular mark is the experimental measurements, and the red solid curve represents the linear fitting curve, which shows no SBS onset during the amplification.

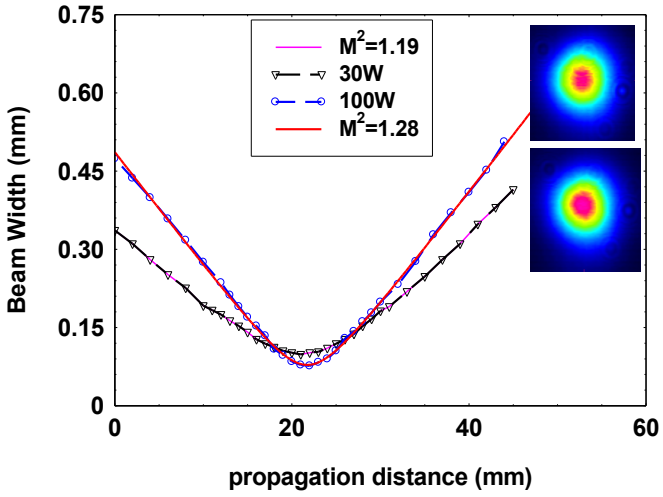

Figure 4.7: M^2 measurements of output from final amplification stage. Dashed curves with triangular and circular marks are experimental M^2 measurements with power level at 30W and 100W respectively. The pink and red solid lines are the M^2 fitting curve to the experiment measurements. Inserts are beam profile recorded for output beam with the two power level.

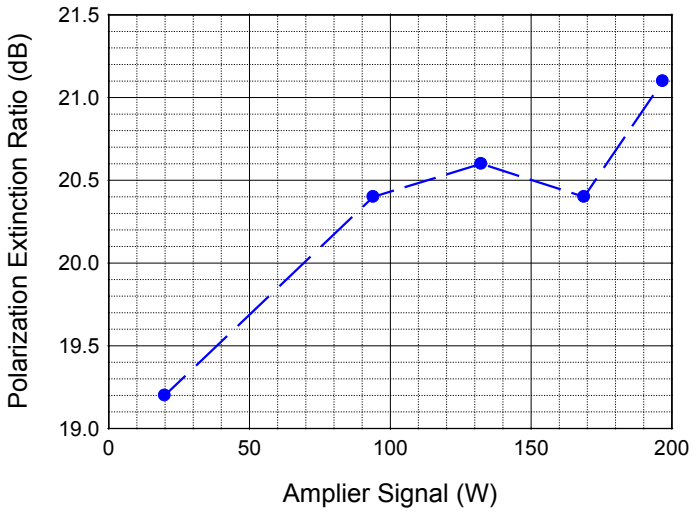

Figure 4.8: PER measurements with final amplifier output power up to 200W.

4.5 Modal content measurement for 37μm active CCC fibers

One of important applications of high power single frequency laser is to provide laser source for interferometry gravitational wave detection (GWD). The 3rd generation of GWD requires laser source with single frequency operation at ~1064nm with kW power level of output as well as high polarization preservation [70]. Fiber based MOPA shows great potential to fulfill these requirements in terms of high power scalability, high conversion efficiency as well as great thermal management. As stated in section 4.2, SBS onset would be the primary limitation for kW level power scaling for single frequency fiber amplifiers, and one main approach to increase critical power for SBS threshold is to enlarge fiber mode area. However, for laser source of GWD, single transverse mode maintenance is also strictly requested. As a result, special design for LMA fibers with effectively single mode output is demanded. CCC fiber seems to be one promising solution to satisfy both requirements due to its robustness of single mode operation with core size up to 60um [55]. To explore the feasibility of CCC fiber based laser system as source for 3rd generation GWD, modal content of output beam from a passive 55um CCC fiber has been measured with TEM00 mode content more than 96.5% which is insensitive to mode excitation condition [102]. While this result solidly validates that CCC fiber is an effectively single mode LMA fiber, further investigation on active CCC fiber under high power operation is still needed.

A 5m long double-clad CCC fiber with 37um core size is examined with amplified single frequency signal power to over 100W. Detailed information and measurement results of this fiber are listed in Table 4.2.

Table 4.2: Summary of specifications of the double-clad 37µm CCC fiber and the TEM_{00} mode content measurement results.

Parameters	Double-Clad CCC
Core Dia. / MFD	37µm / 30µm
Core NA @ 1060nm	0.068
Inner Cladding Dia / NA	N/A
Outer Cladding Dia / NA	413 µm / 0.46
Absorption @ 976nm	~1 dB/m
Side Core Ø, NA	9.8 µm / 0.089
Helix Period	6 mm
Bending Dia.	20cm
Overlap with LP01	100 % (assumed)
Length	5m
Amplifier Power Output	160W
TEM_{00} Mode Content	88%~93%

Single frequency wave was first generated from a NPRO and then amplified by a two-stage Yb-doped PM fiber MOPA as illustrated in Fig. 4.9(a). The amplified signal was then sent to power meter while a small portion of the power was picked and directed to mode content measurement setup as shown in Fig. 4.9(b).

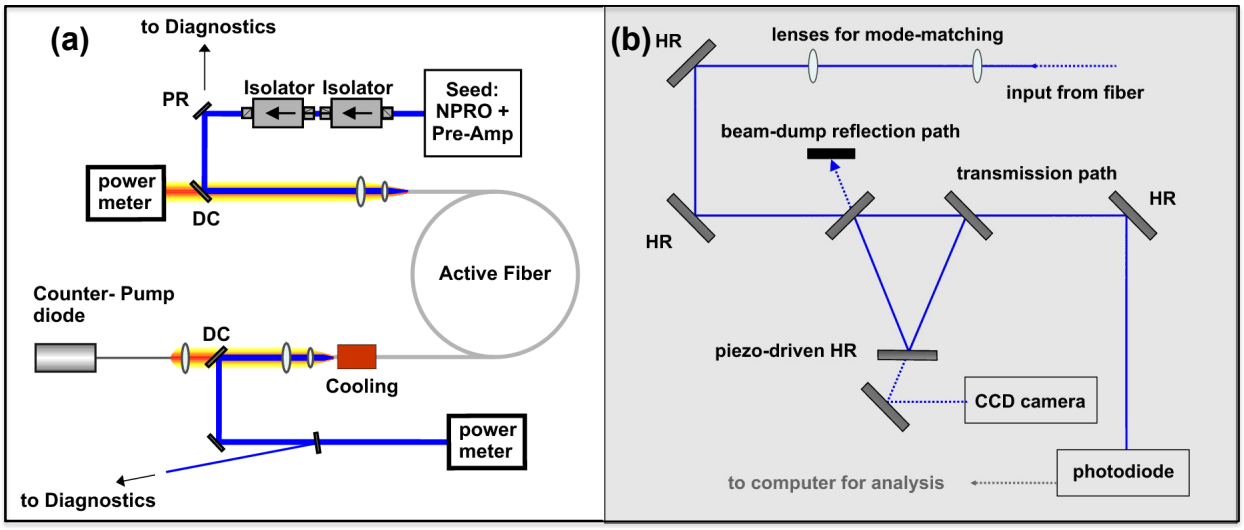

Figure 4.9: (a) Illustration of power amplification stages setup. (b) Model content measurement setup consists of a 3 mirror non-confocal ring cavity.

The fiber MOPA chain was seeded by a non-planar ring oscillator (NPRO) with up to 500mW at 1064nm and ~1kHz bandwidth. A pre-amplifier consisted of PM LMA fiber with

10μm core and 125μm cladding was followed to boost the seeding power to up to 11.5W. The final and main amplifier was based on 37μm Yb-doped CCC fibers, which was counter-pumped by a fiber-coupled pump diode module at 976nm. The amplified signal was then separated from pump-wave by a dichroic mirror with small portion of the output picked up by a silica plate and directed to diagnostic stage.

The diagnostic beam then traveled through several polarization optics such as PBS and waveplates to provide the mode scanning cavity with linear polarized beam at required power level, i.e. ~120mW. The non-confocal scanning cavity contained three mirrors, two of which were plane mirror mounted at 45^{o} with partial transmission and the third one was a piezo-driven curved mirror with high reflection. By driving this mirror, cavity length varied and hence resonant eigenmode was selected and transmitted to photo-detector while the rest of the modes are all reflected. All of the eigenmodes were free space TEM_{nm} modes. With single frequency beam propagating in this cavity, only one eigenmode would exist due to the narrow bandwidth. As a result modes carried with this signal could be decomposed and measured by scanning the cavity length [97].

The mode contents of amplified output were examined in small seeding, high gain region as well as strong seeding high power region. In small seeding case, the final amplifier stage was seeded with 130mW and amplified to achieve over 20dB gain. For strong seeding case, the final amplifier was seeded with 11.5W and amplified to around 150W output power. Modal content was measured during the amplification process for both cases.

As shown in Fig. 4.10, TEM_{00} mode content and amplified power versus absorbed pump power was plotted for the double-clad CCC fibers operating with small and strong seeding respectively. In small seeding amplification, gain up to 21.8dB was achieved with TEM_{00} mode

content over 95% during the whole process. And in strong seeding case, TEM_{00} mode content stayed around 90% for up to 130W output power; it then degraded to 87.3% at a maximum output power of 160W. The power scaling was limited by the low efficiency of pump absorption due to the round shape of 400μm cladding. The mode scan measurements at 20W output with small signal seeding as well as at 130W output with large signal seeding are shown in Fig. 4.11.

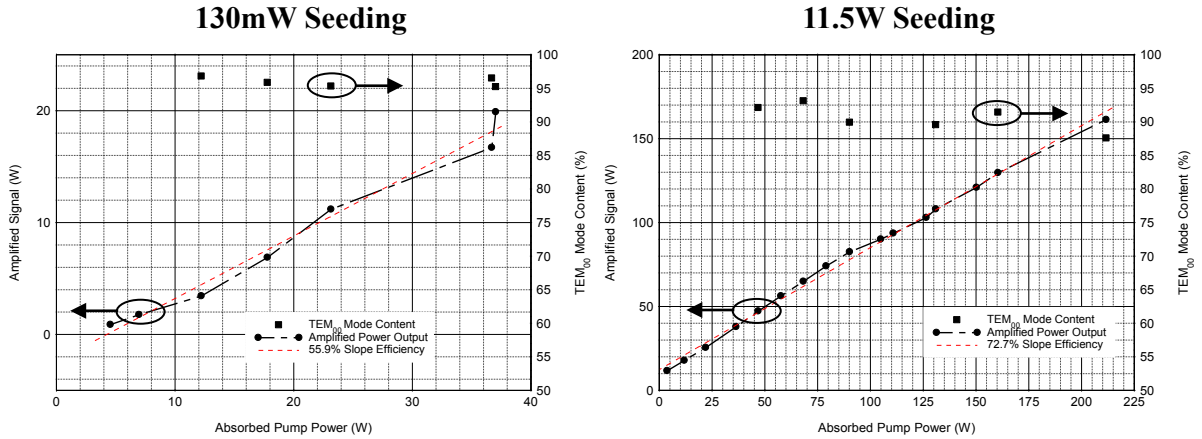

Figure 4.10: Power amplification and TEM_{00} model content measurements versus absorbed pump power. The black curve with dots represents the amplified signal power. The red dashed line is the linear fitting for the amplification. The black square marks are TEM_{00} modal contents measured during power scaling. (a) Small signal seeding with 130mW. (b) Large signal seeding with 11.3W.

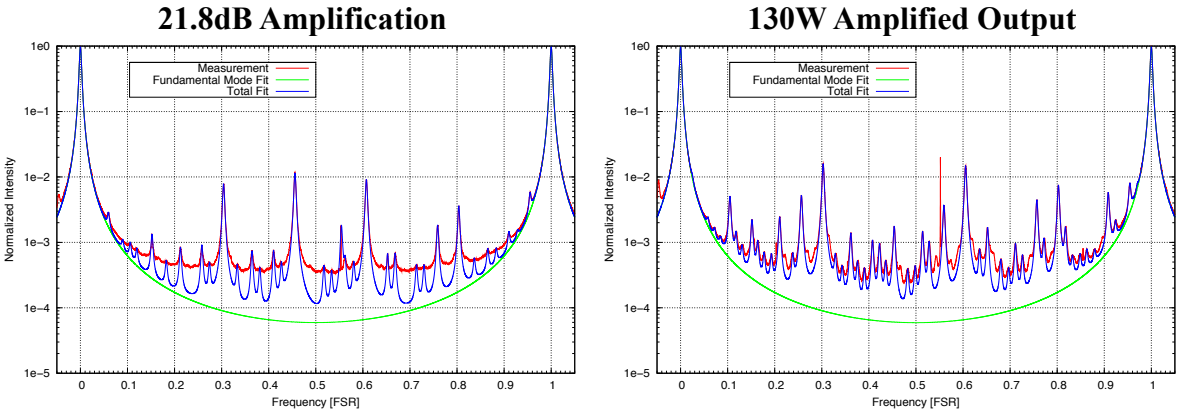

Figure 4.11 Mode scan measurements over one free spectral range. The green curve represents ideal pure TEM_{00} mode scan results. The red curve is the experimental scan recording. The blue curve is the modal content fitting to the measurements. (a) Mode scan recorded at 20W amplified output power with small signal seeding. (b) Mode scan recorded at 130W amplified output with large signal seeding.

These tests though conducted with imperfectly designed but still show comparable fundamental mode content around 150W as that of other commercialized fibers [98-100].

4.6 Conclusion

In this Chapter, single frequency CW power scalability of CCC fiber to nearly 600W is demonstrated with single transverse mode, single polarization and no SBS onset. With also the TEM_{00} mode content characterized, the potential of CCC fiber for high power fiber laser array is demonstrated.

Chapter 5

High-energy nano-second pulse generation with 55μm core Yb-doped CCC amplifier

5.1 Introduction

At present, high-energy nano-second pulse are needed in a variety of industrial applications ranging from material processing to EUV lithography and metrology. For industrial applications productivity, i.e. high processing speed and large volume, is necessary. This productivity is associated with high average power. Furthermore, in practical usage, compactness and reliability of a laser source is very important. High power pulsed fiber lasers show remarkable potential to fulfill these requirements with following advantages. Firstly, effective heat dissipation due to the large surface-to-volume ratio of fiber enables high average powers. Furthermore, the capability of monolithic integration of fiber could significantly reduce the size of the system as well as the needs of realignment.

In recent years, high-energy nanosecond pulses have been demonstrated with large core Yb-doped fiber MOPA both in free space and monolithic format [103,104]. However, due to the large core sizes of the fibers used for high energy extraction, modal quality is sacrificed. To maintain near-diffraction-limit beam quality, various design approaches for fibers with large mode area have been investigated. MOPA based on Photonic crystal fiber (PCF) rods have been developed for high-energy operation, emitting ~1ns pulses of over 4MW peak power with

M2=1.3 [106]. Recently, large–pitch photonic crystal fiber has been presented, culminating in a demonstration of sub-60ns pulses with 26mJ pulse energy and good beam quality [107]. These concepts are inherently free-space approaches though, which sacrifice the remarkable practical advantages of monolithic integration offered by conventional small-core flexible optical fibers. With carefully coiling and seeding to a 65µm - 80µm core LMA fiber laser driver, 6.2ns pulse duration and 6mJ pulse energy has been produced for efficient 13.5nm in-band EUV generation [105], but such a large core LMA fiber does not provide with a robust single mode performance. It cannot maintain beam quality after splicing, which makes further integration impossible. Recently we demonstrated a nanosecond-pulsed fiber MOPA based on 35µm and 55µm core Yb-doped CCC fibers emitting >9mJ SRS free output pulses with approximately MW peak power [61]. Due to the unique features of CCC fiber as effectively single mode fiber, pure and robust single transverse mode is maintained during the energy scaling process. It shows significant potential of CCC fiber technology as a compact and practical platform for industrial applications. In Fig.5.1, all the energy amplification in ns region discussed above is summarized.

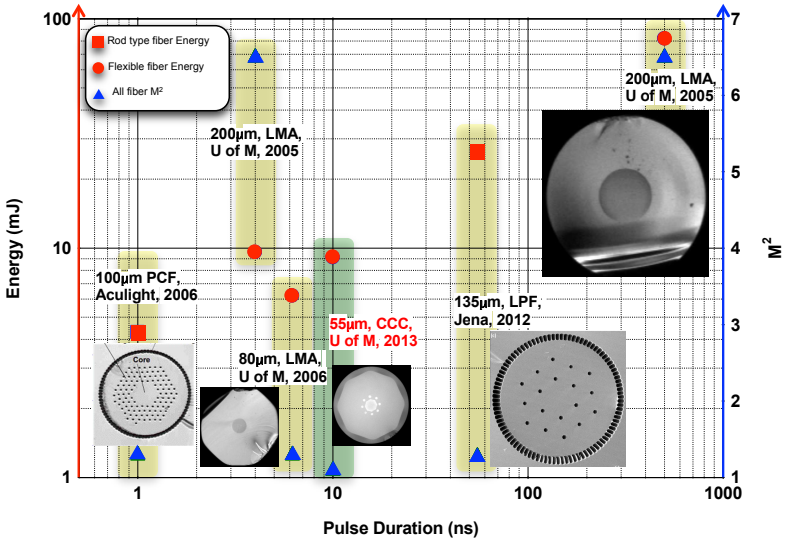

Figure 5.1: State of the art of energy amplification with fiber MOPA in ns region.

5.2 Limitations for pulse amplification in fiber MOPA

Although fiber MOPA has shown great potential for high-energy pulse amplifications, the ultimate pulse energy from a fiber laser is limited by several factors, such as the extractable energy stored in the amplifier, bulk damage of the fiber material and self-focusing.

The energy extractable from a pulsed fiber amplifier is the energy stored in the fiber above the bleaching energy level, which is calculated by the multiplication of natural logarithm of small signal gain G_0 of the amplifier and its saturation energy E_{sat} [108]:

$$E_{ext} = \ln(G_0)\, E_{sat} \tag{5.1}$$

where

$$E_{sat} = \frac{h\nu_s A}{\Gamma_s(\sigma_e+\sigma_a)} \tag{5.2}$$

where h is plank constant. ν_s is signal frequency. A is core area of the fiber and Γ_s is the overlap of signal mode area with core. σ_e and σ_a are absorption and emission cross-section at signal frequency respectively. Since small signal gain of a fiber amplifier is limited by ASE to about 30dB, the extractable energy from a pulsed fiber amplifier could be estimated as about 7 times of its saturation energy.

Another challenge for the energy scaling of pulsed fiber amplifiers is the optical damage of fiber material. Stuart et al has described this phenomenon as result of electro production by multi-photon ionization, joule heating and avalanche driven by the laser field [109]. For pulse duration larger than 1ps, the threshold of damage fluence for the pulse scales with the square root of pulse duration. With the experimental characterized bulk damage threshold for Yb-doped fiber as about 800J/cm^2 for pulse width of 6.2ns [30], the damage threshold for various pulse durations is given by:

$$E_{th} = 3.2\times10^{-6} \cdot A\sqrt{\tau_p} \tag{5.3}$$

where τ_p is the pulse duration and A is the fiber core area.

The ultimate limiting factor for pulse amplification in gain medium is self-focusing of the beam induced optical damage. Due to optical Kerr effect, refractive index of gain medium depends on the intensity of the laser propagating through, and can be described by [110]:

$$n = n_0 + n_2 I \tag{5.4}$$

where n_0 is the linear refractive index, n_2 is the nonlinear refractive index and I is laser intensity. Since in most cases, beam propagating along the fiber for pulse amplification is with a Gaussian distribution, and refractive indices of the material is hence modified by the beam and varies from the center of the beam to the edge. In most of the laser medium, with n_2 as a positive factor, the modified refractive index would behave as a focusing lens. When this focusing effect is balanced with the diffraction of the propagating beam, laser field would propagate with a fixed beam size and the so-called self-trapping of light occurs. The threshold for self-focusing induced damage is hence defined as the critical power of self-trapping:

$$P_{cr} = \frac{\pi(0.61)^2\lambda^2}{8n_0n_2} \tag{5.5}$$

In fused silica, $n_0\approx1.45$, and $n_2=2\times10^{-20}m^2/W$. The critical peak power for pulse amplification at 1μm is hence around 5MW. In Fig. 5.2 we depicted the energy limitations discussed above versus fiber core size for pulse durations range from hundreds of picosecond to tens of nanosecond. It could be concluded from this plot that the higher energy to achieve the larger fiber core is in need.

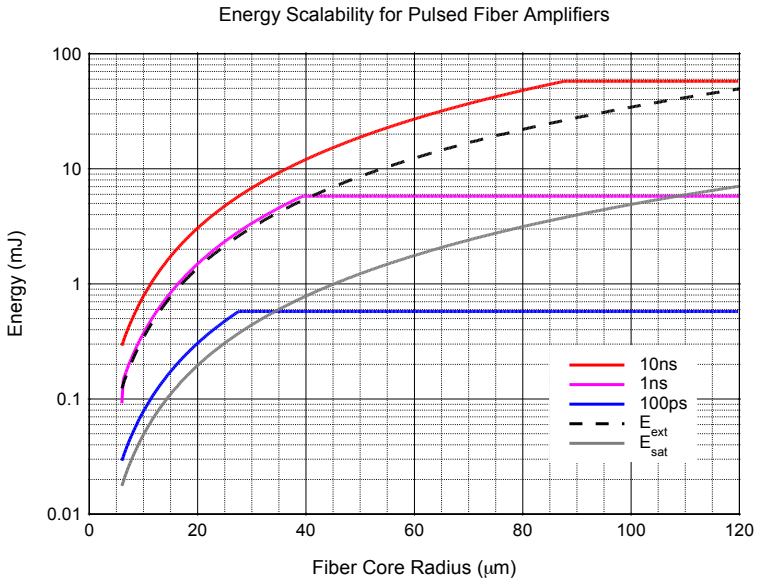

Figure 5.2: Energy scalability for pulsed fiber amplifiers operating at 1064nm in ns region. The dashed black curve is the extractable energy for different fiber core size. The grey solid curve is the saturation energy for various fiber core sizes. The red pink and blue curves are energy limitation set by bulk damage threshold and self-focusing for pulse durations of 100ps, 1ns and 10ns.

However, in practical pulsed fiber MOPA, nonlinear effects such as Self Phase Modulation (SPM), Four Wave Mixing (FWM), Stimulated Brillouin Scattering (SBS) and Stimulated Raman Scattering (SRS) occur well before these limits, which would largely affect the spectral distribution of the energy and even be detrimental for the amplifier system [31]. As Kerr effect causing intensity-dependent modification of material refractive index, other than spatially self-focusing of the beam, it also leads to temporal phase shift within the pulse during propagation, which is SPM and results in a spectral broadening dependent on pulse shape. For pulses with duration < 0.5ns, SPM is most prominent and hence an impeding factor for coherent combining systems. As a third-order parametric process, FWM involves annihilating of two photons and creating two new photons satisfying energy preservation as well as phase matching requirements. In high power fiber lasers in nanosecond region with broadband spectrum, with strong amplification of the signal, which is pump beam for FWM, substantial FWM generation

could be observed as broadening of the spectrum notwithstanding the phase matching [111]. For linewidth-limited pulse in multi-nanosecond region, SBS would be the most detrimental factor for the MOPA [112].

For practical pulse amplification with nanosecond pulse duration, the main limiting factor is SRS. As a inelastic nonlinear process induced by interaction of laser field and optical phonon, SRS involves generation of photons at a frequency downshifted from that of the incident photon. Different from SBS process, the gain spectrum of Raman scattering extends over a broad spectral range. As a result, SRS mainly cause transferring of energy to unwanted spectral range and limits further scaling of the energy. For fused silica fiber, Raman gain spectrum covers a bandwidth of 40 THz, with the gain peak at about 13THz away from the Raman pump wave frequency. The critical power of SRS onset is given by [96]:

$$P_{cr} = \frac{\chi^* A_{eff}}{g_0 L_{eff}} \tag{5.6}$$

where g_0 is Raman gain coefficient at pulse wavelength, which is 1×10^{-13}m/W at 1μm. Leff ≈1/g is efficient propagation length of the fiber, with g as gain of the fiber at pulse wavelength. Aeff is mode field area of the fiber. χ is a numerical factor which depends on fiber parameters and operating conditions. For example, for forward SRS in standard single mode fibers, $\chi = 16$, while for backward SRS in the same fiber, $\chi = 20$. Similar as for SBS mitigation, one could utilize large core fiber with high doping to raise SRS threshold as indicated from Eqn. (5.6). Furthermore, one could also exploit special techniques such as bending fiber to certain radius for Stokes wave peak loss enhancement [114], fiber with special design to have high loss at Stokes frequencies [115] or spectrally tailored transmission induced propagation length independent Raman threshold [113].

As discussed above, to maximize the energy scalability of the fiber amplifier as well as for better mitigation of nonlinear effects, fiber with high doping concentration and large core area is preferred.

5.3 Experiment setup and results

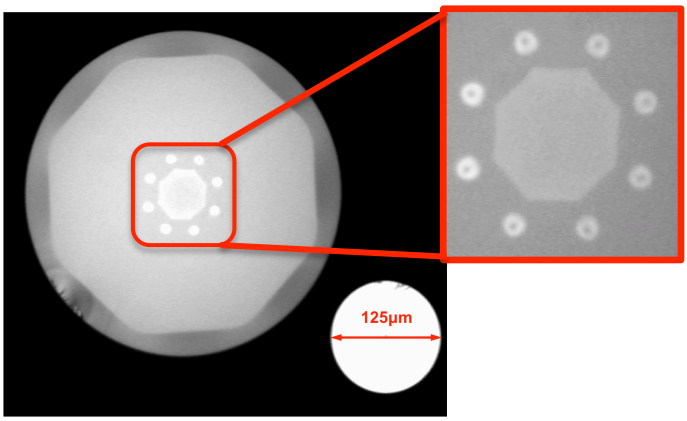

Figure 5.3: microscopic image of triple-clad Yb-doped CCC fiber with 55µm core. The inserted picture shows the octagonal central core surrounded by eight round side cores.

According to the analysis in previous section, a piece of triple-clad Yb-doped CCC fiber with 55µm core diameter was selected as the gain fiber for the main amplification stage to enhance the scalability of our fiber MOPA for nanosecond pulses. Unlike the single side core design for previous CCC fibers, eight identical side cores are helically wound along the octagonal shape central core in this fiber as shown in Fig. 5.3. This design was chosen to enhance the mode coupling strength needed due to the increased amount of high-order modes (HOMs) supported by the central core with enlarged mode area. The Yb-doped central core has a diameter of 55µm with mode field diameter (MFD) of 42µm and NA of 0.072. Side cores are Ge-doped with ~11µm diameter, 0.088NA and a helix period of 5.3mm. Inner pump cladding of the fiber is doped with fluorine providing 0.22NA with a diameter of 305µm while the outer

cladding is 360µm in diameter and 0.46NA. The pump absorption ratio at 975nm is around 10dB/m [55].

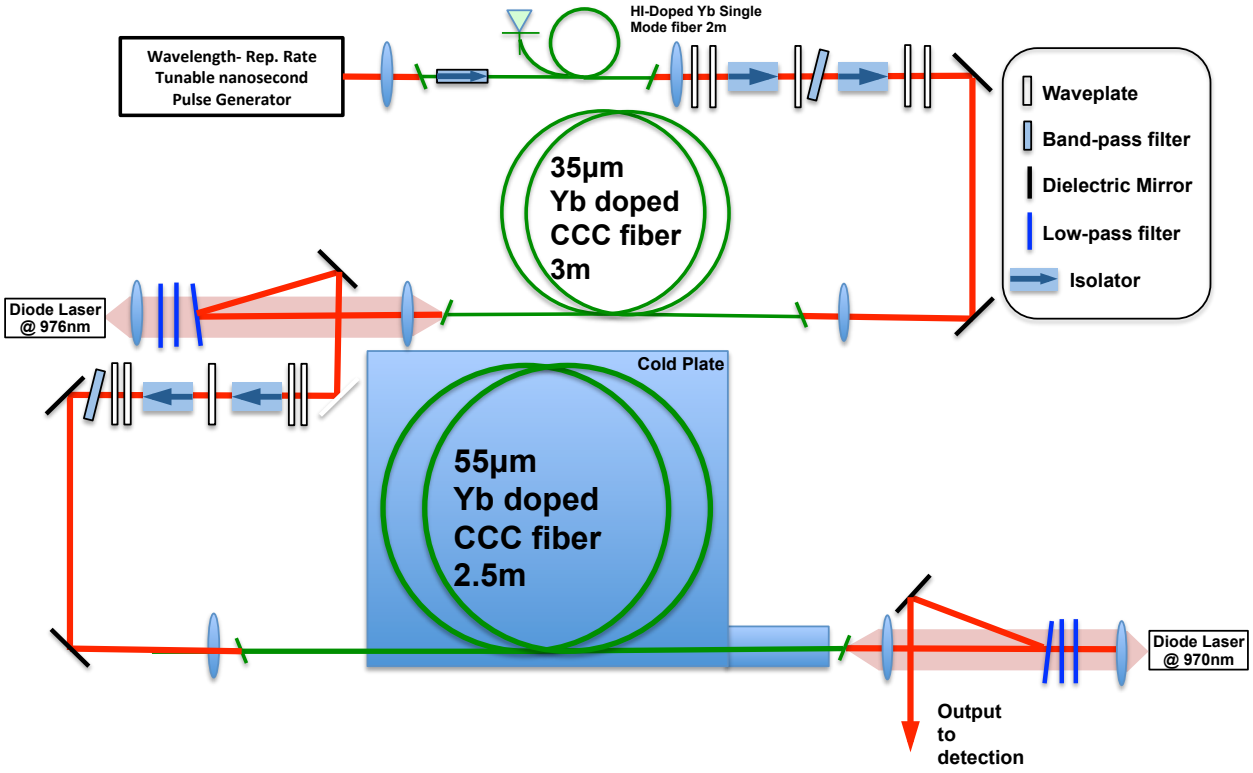

Figure 5.4: System setup for ns pulse amplification.

Fig. 5.4 illustrates the schematic setup of the nanosecond pulsed MOPA based on Yb-doped CCC fibers. Seed pulse was generated by a programmable single-mode fiber based self-seeded nanosecond pulse generator on an optical breadboard, with variable durations and repetition rates, as well as tunable wavelengths [60]. In this experiment, the pulse generator was tuned to operate at 1042nm with a FWHM of ~3nm with a repetition rate of 5kHz. And the pulse energy of the output from this generator was 280nJ with pulse duration of 15ns. The pulses were then coupled into a 2m long Yb-doped polarization maintained (PM) conventional single mode fiber based preamplifier to boost the pulse energy to 8µJ. Two bandpass filters with 3nm FWHM bandwidth were implemented after the pulse generator and this single mode fiber stage

respectively to narrow the pulse spectrum to the original bandwidth from the broadening caused by SPM as well as to filter out the SRS signal.

To better deplete ASE in the final stage and also to extract as many energy as possible, the pulse was further enlarged in a second preamplifier stage consisting of a 3m long double-clad Yb-doped CCC fiber with 35μm core diameter, 250μm cladding and ~9dB/m absorption at 975nm. Counter-pumped by a fiber-coupled diode laser operating at 976nm, this stage increased pulse energy to 140 μJ. Another 3nm bandpass filter was placed in the output beam path to narrow the pulse spectrum again.

The final and main amplification stage was composed of a 2.5m long Yb-doped CCC fiber with 55μm core diameter. The fiber was coiled with a diameter of 40cm and laid on cold plate water cooled to around 15^{o}C. Both ends of the fiber were spliced to a 8mm coreless fiber and polished to 12^{o}. Counter-pumped by a fiber-coupled high brightness diode laser (Fraunhofer USA) to 200W at ~970nm, the main amplification stage absorbed around 150W pump power and emitted 10ns pulses with 9.1mJ energy and 45.5W average power within the core area.

Output energy and peak power of the pulse versus absorbed pump power from the main amplification stage is also depicted in Fig. 5.5. Inserts in Fig. 5.5 shows beam profile recorded with 1mJ and 8mJ pulse energy respectively. The consistency of the beam profile confirms the robustness of the output single mode quality. The overall performance of system is summarized in table 5.1.

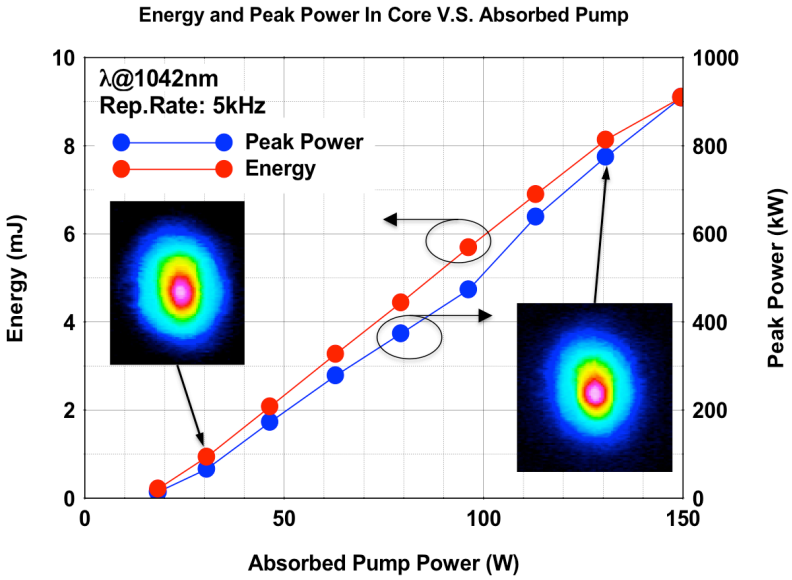

Figure 5.5: Energy and peak power versus absorbed pump power during power scaling. The red curve is energy amplification and the blue one is the peak power. The inserts are beam profiles recorded at 1mJ and 8.1mJ output energy level respectively.

Table 5.1: Summary of specifications for fibers used in different amplification stages as well as the output pulse characteristics from these three stages. *The output energy and pulse duration of the two preamplifiers in this table are measured after the band-pass filter.

Amplification Stage	1	2	3
Fiber type	Panda fiber	CCC fiber	CCC fiber
Core Φ (μm)	6	35	55
MFD (μm)	7.5	30	42
Cladding type	Single clad	Double clad	Triple clad
Cladding Φ (μm)	125	250	300/360
Fiber length (m)	2.5	3	2.5
Pump absorption @ 975nm (dB/m)	250	9	10
Pumping configuration	Co-pump	Counter-pump	Counter-pump
Pulse duration* (ns)	15	15	10
Energy*	8μJ	140μJ	9.1mJ
Peak power	0.5kW	9.3kW	0.91MW

Pulse shape and spectrum were monitored and recorded during the scaling of energy to detect any unwanted power build up in ASE and SRS bandwidth. Spectra of seeding pulse for

the final amplifier as well as of output pulse with 8mJ energy are shown in Fig. 5.6. Normalized spectra in linear scale are also depicted as inserted. The triangle-like shape of spectral broadening also validates that it is free of ASE but purely from nonlinear effects. As discussed in previous section, in fused silica Raman gain peak is at a frequency downshifted by about 13THz from the pump frequency. In this experiment, with pulse wavelength at 1042nm, the Raman gain peak is at around 1080nm. From the recorded spectrum with pulse energy at 8mJ and peak power of 0.8MW, no onset of SRS is observed.

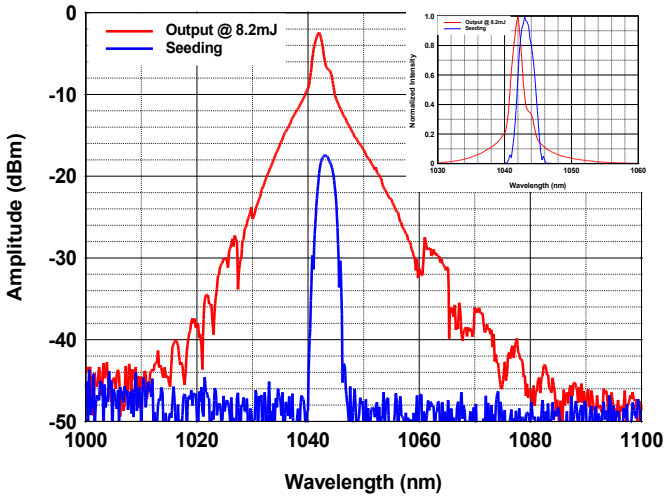

Figure 5.6: Spectra of output pulse at 8.2mJ and seeding pulse for the final amplifier stage based on 55μm triple-clad CCC fiber. The insert shows the spectra in linear scale and a blue shift is observed due to the gain preference of Yb. The red curve is output spectrum at 8.2mJ and the blue one is seeding spectrum.

Following calculation for SRS threshold given by Eqn (5.6), but with a modification of the constant coefficient to apply to large mode area fibers with high gain, we can get an approximation of anticipated critical peak power for this final stage by following equation:

$$P_{cr} = \frac{30^{*}A_{eff}}{g_o L_{eff}} \tag{5.7}$$

With L_{eff} ≈0.6m, A_{eff} around 1400μm^2 in our case, one would expect to have reached SRS threshold at close to 650kW, which is not consistent with our measurement. We contribute this

discrepancy to two reasons. Firstly, because of the sensitivity of material composition in the fiber core, the actual Raman gain coefficient is uncertain, thus making the predicted threshold a rough approximation. Secondly, and the main cause is that SRS is partially suppressed in this fiber. As stated in [60, 113], one important feature of CCC fiber is that the cutoff at long wavelength due to mode selection provides SRS suppression for certain operating wavelength, which is the SRS stokes-wave suppression enabled by the spectrally tailored transmission of CCC fiber. Figure 5.7 shows the overlap of Raman gain spectra with pump wavelength at 1042nm (blue) and the super-continuum transmission spectra of 2.5m long 55um core Yb-doped CCC fiber used in pulse amplification (red). The spike at around 1064nm of the transmission spectra is from the super-continuum source. The dip centered at 1070nm with a maximum attenuation of 25dB is the region of SRS suppression for this fiber. As shown in Figure 7, the Raman gain peak is on the edge of the SRS suppression range, thus we expect that there is still some effect of Raman suppression in this amplification.

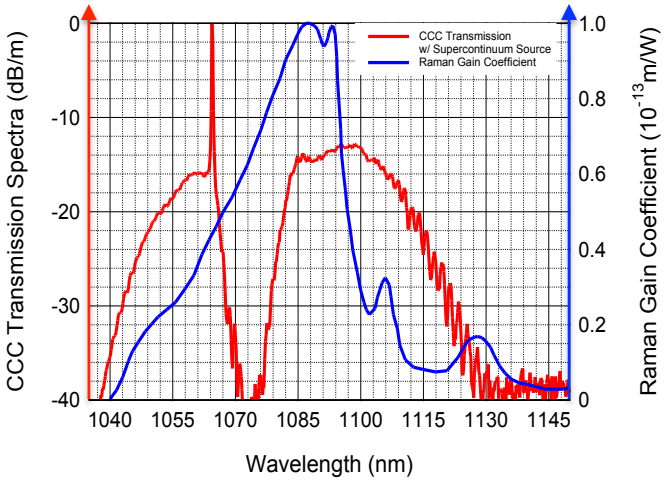

Figure 5.7: Spectrum of transmission of super-continuum from 55µm triple-clad CCC fiber utilized in final amplifier (red curve) as well as that of the Raman gain for nonlinear pump wave at 1040nm (blue curve). The peak at 1060nm from the CCC transmission spectrum is from super-continuum source itself.

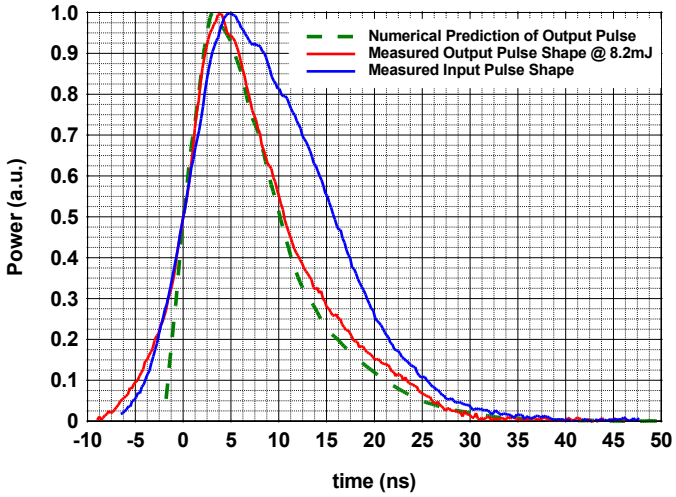

Figure 5.8: Normalized pulse shapes from measurement and calculation. The red curve is the measured output pulse shape at 8.2mJ. The blue curve is the measured input pulse shape for final amplification stage at 140μJ. The green curve is calculated pulse shape with input pulse shape at 140μJ and 25dB small signal gain.

The temporal intensity shape of the seeding pulse and that of pulse with 8mJ at output end are illustrated in Fig. 5.8 as blue and red curves. The pulse duration was narrowed from 15ns to 10ns during the energy scaling. To validate the pulse reshaping as shown in Fig. 5.7, characterization of amplifier saturation is done and the predicted reshaping of pulse with 8mJ output energy is also depicted in Figure 6 as green dashed curve to compare to the measured pulse shape with same pulse energy. The expected pulse shape is numerically simulated following equation [108]:

$$I_{out}(t) = \frac{G_0}{G_0-(G_0-1)\exp\left[-\int_{t_0}^{t} I_{in}(t)dt/U_{sat}\right]} I_{in}(t) \tag{5.8}$$

where G_0 is the small signal gain of the amplifier, which is assumed to be 25dB in this case. $U_{sat} = h\nu_s/(\sigma_e + \sigma_a)$ is saturation fluence at pulse wavelength, which is 0.38μJ/μm^2 for 1042nm. $I_{in}(t)$ and $I_{out}(t)$ are instantaneous input and output pulse intensities respectively. Good

agreement between recorded and calculated pulse shape at 8mJ exhibits the consistency of measured amplifier saturation and the prediction.

5.4 Splicibility of large core CCC fibers

As we mentioned at beginning, for monolithic integration, one of the key requirements is the capability of maintaining mode quality after splicing of the fibers. To confirm the spliciblity of this large core CCC fiber, we measure the output beam quality before and after a cut-and-resplice process with this fiber. The evaluation of the beam quality was by a knife-edge M^2 measurement.

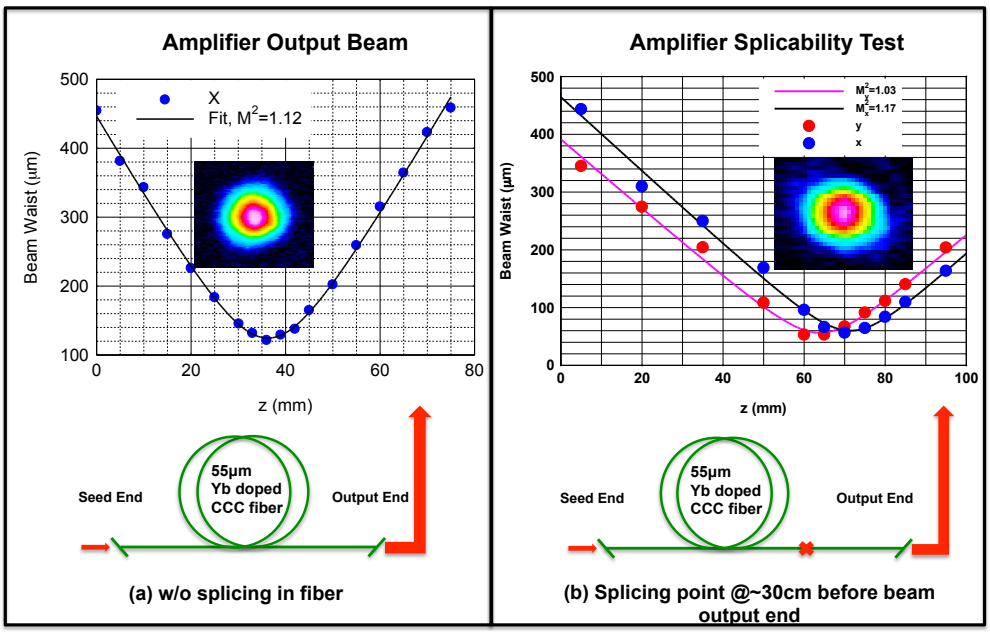

Figure 5.9: Knife edge M^2 measurements with output pulse from the final amplification stage. Dots are experimental measurement of beam waists at different position. Blue dots are measurements along horizontal direction while the red ones are along vertical direction. The solid curves are M^2 fitting curve for the measurements. Inserts are near field beam profiles recorded during the measurements. (a) M^2 measurements along horizontal direction with intact fiber. (b) M^2 measurements along horizontal and vertical direction for output amplified pulse from the same 55μm CCC fiber after a cut-and-resplice process of the fiber at about 30cm away from the output end.

As shown in Figure 5.9(a), M^2 of the output beam from the intact fiber was first measured with a fitted M2 value of 1.12 indicating that the output beam is nearly diffraction limited.

Together with the invariability of beam profiles recorded during the power scaling process in Fig. 5.5, it confirms that the output beam is consistently single mode under all operating conditions.

A cleavage was made at 30cm away from the output end of the fiber and then the two fiber pieces were spliced back together with commercialized fiber fusion splicer (Ericsson PM950). M^2 measurements were done in both directions along with (as x direction here) and perpendicular to (as y direction here) the coiling axis of the fiber. As shown in Figure 5.9(b), M_x^2=1.17 and M_y^2=1.03 are good indications that large core CCC fiber is not only a flexible fiber but also a splicible fiber with effectively single mode operation. And these are all indispensible reasons why CCC fiber is a promising technology for practical high power monolithic laser systems.

5.5 Conclusion

We report 9.1mJ and 10ns pulses with close to mega Watt peak power at 5 kHz form a single-mode 55μm core Yb-doped triple-clad CCC amplifier. It is interesting to note that at these energies relatively small reshaping due to energy saturation have been observed, indicating potential of even higher energies in this fiber. It appears that extractable pulse energy from a 55μm core CCC fiber is significantly higher than from a 80μm core LMA fiber [105]. The system provides near-diffraction limited beam with M2<1.2. And no SRS is onset in this high-energy pulse amplifier, due to the SRS mitigation provided by this CCC fiber. This demonstration shows the potential of large core CCC fiber technology for monolithic fiber laser integration, which could be used as high power and high energy pulsed sources for various applications while preserving advantages of standard single mode fiber technology.

Chapter 6

CCC fiber for advanced pulse and ultra-short pulse coherent combining fiber amplifier arrays

6.1 Introduction

For ultra-short pulse amplification, the main challenge is high peak power induced optical damage and nonlinear effects such as self-phase modulation, four-wave-mixing and catastrophic self-focusing, which may damage the system and restrict the ultimate extractable energy from the system. With relatively small MFD and long propagation length, fiber amplifiers are more susceptible to this limitation. In the latest decades, chirped pulse amplification (CPA) [116] technique has been extensively utilized in fiber-based systems and achieved energy to 2.2mJ level with sub-picosecond pulses [117]. However, the ultimate extractable energy from a fiber based CPA (FCPA) system is restricted by self-phase-modulation nonlinearity since in practice, the stretched pulse duration is limited to around 1ns by the cost and size of gratings [118]. Consequently, to achieve ultra-short pulses with energy of multi-Joule as desired for various applications such as high-field physics research, pulse amplification with a single fiber amplifier system is not sufficient.

Various schemes of coherently combined FCPA systems are proposed and demonstrated as a promising solution for further energy and average power scaling of ultra-short pulses. One approach is to split the pulses emitted from the preamplifier spatially first; amplify them

separately in multiple channels and then recombine them spatially by either partially reflective surfaces or polarization beam splitters (PBS) into one big pulse. With this approach, up to four-channel combination has been demonstrated [123]. More recently, power scaling of four-channel FCPA array has been demonstrated with final output 450fs pulse energy of 1.3mJ and average power of 530W [37]. However, reaching ~J to ~10's J of energy required by majority of high intensity applications, such as laser plasma accelerators, would require very large number of $\sim 10^4$ - 10^5 of parallel amplification channels. Such a large number of amplifier channels constitutes a formidable technological problem.

An alternative path is to separate the pulses temporally instead of spatially before amplification and then coherently adding them together sequentially, so that effective pulse duration in an amplifier is increased, and much higher pulse energies per channel can be extracted. This could significantly reduce number of parallel amplification channels.

Divided-pulse amplification (DPA) has been proposed [41,120] recently to improve the energy scalability of single fiber amplifier channel by utilizing a sequence of cascaded Mach-Zehnder-type splitters and combiners to create pulse train before amplification and recombine them into a single pulse after that. With this approach, up to 6.5mJ amplified pulse energy was achieved and 1.25mJ of recombined and recompressed pulse was demonstrated [41]. However, apart from being very cumbersome, this technique can not be applied to increasing pulse number beyond few, since delay line length increases exponentially with the number of splitting/recombining stages. Hence array-size reduction would be insignificant.

Concept of coherent pulse stacking (CPS) was proposed and demonstrated as a solution that can reduce array size by two to three orders of magnitude [42]. With this approach, the burst of pulses is generated starting from a mode-locked femtosecond pulse laser followed by an

amplitude and phase modulators, which provide the reuiqred amplitude and phase shaping of the pulse burst. The seed pulse burst could pre-shaped to counteract the saturation effect in power amplifiers. After the amplification, the burst is sent into Gires-Tournois interferometer (GTI) resonant pulse-stacking cavities. With phase modulation of the pulses within the burst, individual pulses would be coherently stacked into a single output pulse. The round-trip length of GTI resonant cavity is equal to the separation between pulses but not the burst duration, which makes it compact for high pulse repetition rates. By suitable cascading of a sequence of these GTI cavities, number of stacked equal-amplitude pulses within a burst could reach 100 to 1000, providing with the corresponding increase in energy from a single fiber amplifier channel. Further analysis in section 6.3 shows that, with burst operation, tens of mJ or even >100mJ may be achieved from a single fiber amplifier channels. Consequently, a corresponding two to three orders of magnitude reduction of the FCPA array size could be achieved, and as few as tens to hundreds of parallel coherently-combined channels could be sufficient for generating multi-Joule pulse energies.

6.2 Experimental demonstration of high-energy coherent pulse stacking from CCC fiber base fiber amplifier

To evaluate the feasibility of CPS, amplification and stacking of a burst consists of nanosecond pulses has been demonstrated. This is a collaboration work with other group members working on the combining technique, while the contribution from this dissertation is mainly on providing high energy amplification from 55μm CCC fiber based fiber amplifier.

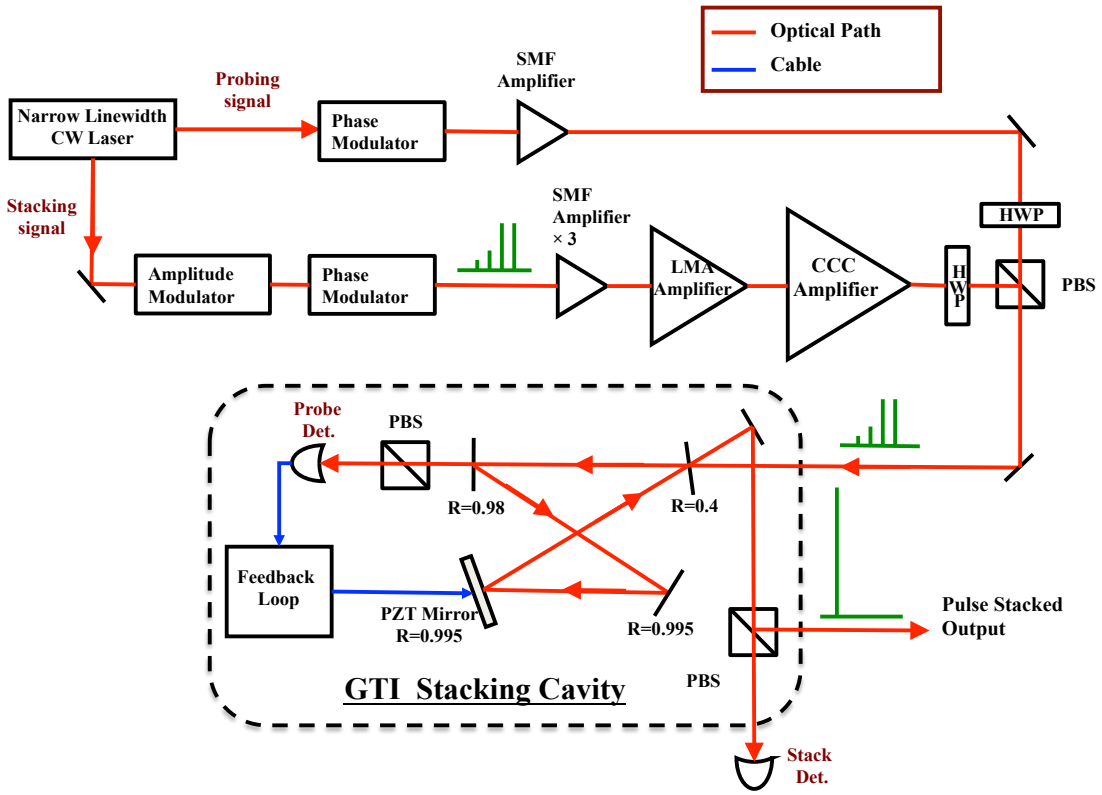

Figure 6.1: Experimental setup for CPS amplification system with carved nanosecond pulse burst.

Fig. 6.1 illustrates the experimental setup for the CPS amplification system with nanosecond pulses. A tunable CW diode laser (Toptica DL100) emitted about 45mW at 1064nm with narrow linewidth. The signal was then divided by a 50:50 fiber splitter into a probing signal for later stabilization of the stacking cavity and a signal as seeding for the pulse amplification and stacking. The seeding signal was carved into a burst of pulses by amplitude modulators and then imprinted with the required phase by a phase modulator. The burst repetition rate is 7.81MHz, with single pulse duration of 850ps and a pulse separation of 5ns. The burst was subsequently amplified by three stages of PM single mode fiber amplifiers. Two acousto-optic modulators (AOM) are implemented between the single mode fiber amplifiers to down-count the burst repetition rate to 10kHz to ensure sufficient seeding power in these pre-amplifiers as well as efficient suppression of ASE power. 1mW burst average power was then injected into a co-

pumped pre-amplifier based on 25μm PM LMA fiber. This pre-amplified was monolithically integrated with a mode-adapting isolator, a 2+1×1 pump combiner and a 2.5m long Yb-doped PM LMA fiber with 25μm core and 250μm cladding. The LMA fiber was coiled to 9cm in diameter to provide sufficient bending loss for HOMs. The burst was boosted to 140mW before the final and main amplifier stage based on 55μm CCC fiber. With a fiber length of 2m and counter pumped by a fiber coupled diode laser (nLight Pearl) the burst was amplified to 10.5W with total energy over 1mJ. A free space isolator and a 4nm bandpass filter were placed between the LMA stage and the final CCC amplifier stage to protect the pre-amplifier from backscattering signal as well as to suppress the ASE power.

The burst entering into and exiting from the GTI resonant cavity is shown in Fig. 6.2. The blue curve is the pulse train within a burst input into the cavity while the red curve represents the corresponding output pulse train. With carefully phase modulation of each pulse within the burst as well as stabilizing the cavity with probing signal, an enhancement of 2.48 of stacked pulse from the maximum individual pulse peak power in the burst was achieved. The contrast of stacked pulse to the most intense “suppressed” output satellite pulse is 16.2dB.

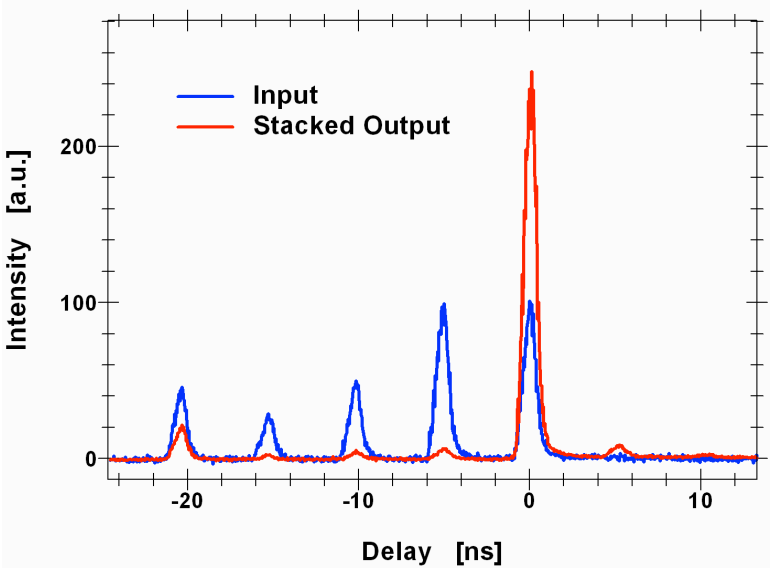

Figure 6.2: Burst shape entering and exiting from the GTI resonant cavity. The blue curve is the input burst signal after amplification. The red curve is the output stacked pulse trace after the cavity.

With experimental demonstration of energy scaled up to over 1mJ and 2.48 enhancement of coherently stacked pulse by CPS of nanosecond pulse amplification from a fiber amplifier based on CCC fiber, this technique shows great feasibility for further energy scaling of ultra-short pulse amplifications with further incorporating of CPA.

6.3 Energy extraction of pulse burst amplification with pulsed pumping.

6.3.1 Limitations for energy scaling in pulsed fiber amplifiers

One advantage of amplification of pulses in a burst is that the ultimate energy limited by optical damage and nonlinearity is raised since the burst could be seen as a further stretching of the pulse. The ultimate energy limits for pulse amplification based on 55μm core CCC fibers with various pulse durations are depicted in Fig. 6.3. The black dashed line is the extractable energy given by Eqn. (5.1) as logarithm of small signal gain multiplies with the saturation energy. Assuming that the small signal gain is 30dB and pulse wavelength is centered at 1064nm, for 55μm fiber core size, the extractable pulse energy is about 10mJ regardless of the pulse duration.

The green line is the self-focusing energy threshold calculated from Eqn. (5.5) while the red line is optical bulk damage limit computed based on Eqn. (5.3). Since in practice, the optical damage may happens at energy lower than the theoretical value indicated by the calculation due to the quality of fiber end facet, one must keep in mind that the optical damage limit may be few factors less than what illustrated in the figure. In practical FCPA systems, the main hindering factor for energy scaling is the SPM induced phase distortions, which cause distortion and breakup of compressed pulses. The accumulation of nonlinear phase shift due to Kerr nonlinearity through the fiber length could be characterized as B-integral, which is given by[108]:

$$B = \frac{2\pi}{\lambda}\int_0^L n_2 I(z)dz \tag{6.1}$$

where I(z) is the intensity of the pulse along the fiber. The criterion to avoid nonlinear distortion and damage due to SPM in a pulsed fiber amplifier is generally to approximately keep B < 1 [108]. Using Eqn. (6.1), the threshold energy before nonlinear damage of the pulse is:

$$E_{crit} = \frac{B\lambda \ln(G_{dB})}{2\pi n_2 L} \cdot A\tau \tag{6.2}$$

where L is the fiber length , A is fiber core area and τ is pulse duration. G_{dB} is the gain of the pulse amplification. In Fig. 6.3, blue and pink curve depicts the threshold energy following calculation in (6.2) at B=π, with assumption of total gain the pulse experienced as 20dB and 30dB respectively. It is clear that for amplification of pulses, the output energy is mainly limited by the nonlinear effect of SPM. For pulses with sub-nanosecond or few nano-seconds pulse duration, the pulse energy without distortion of pulse shape is limited to 100μJ to ~1mJ range. With stretching the pulse duration to hundreds of nano-seconds, this threshold could be increased to few tens of milli-Joule and even 100mJ.

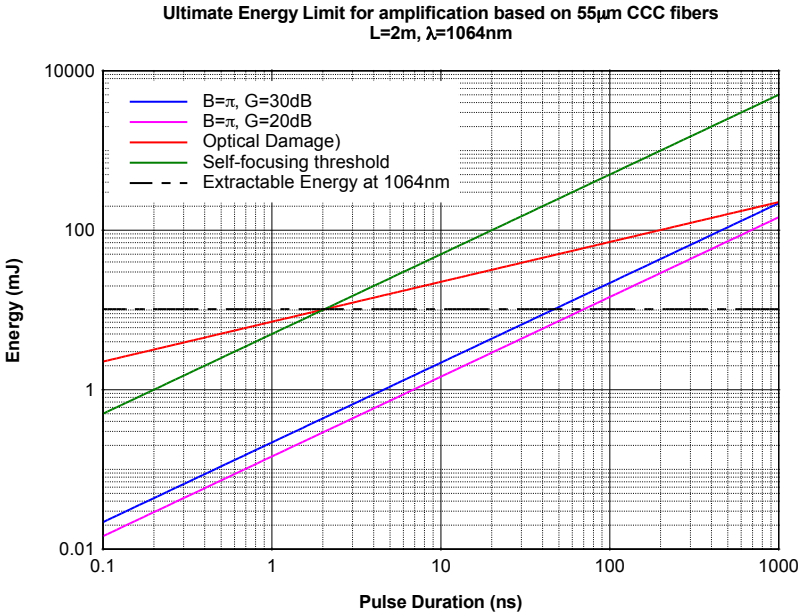

Figure 6.3: Ultimate Energy limit for pulse amplification based on 2.5m of 55μm CCC fiber amplifier.

In pulsed fiber amplifier for CPS, with amplification of a burst of pulses, the effective pulse duration may be much longer than the single pulse duration. Subsequently, the detrimental energy threshold set by optical damage and nonlinear effects are substantially raised up for burst operation. And therefore, the main restriction for further scaling of energy is now set by the extractable energy stored within the amplifier, which is limited by the onset of ASE as discussed in Chapter V.

To overcome this restriction, the only way is to break the energy storage limit set by ASE. In practical system, one plausible solution is to pump the amplifier with pulses synchronized to the signal. Together with burst consists of pulses with high repetition rate, the amplification process within the burst could be seen as a quasi-CW operation. In this way, the extractable energy during the amplification is no longer the stored the energy before the burst, but is indeed the deposited energy by the pumping pulse during the burst. As long as the energy within the pump pulse is large enough, tens or even over one hundred milli-Joule could be deposited and then

extracted during the burst operation. In practical case, this could be realized by tandem pumping with a combination of few pulsed amplifiers based on large core fibers with tens of milli-Joule output at wavelength shorter than 1020nm as illustrated in Fig. 6.4.

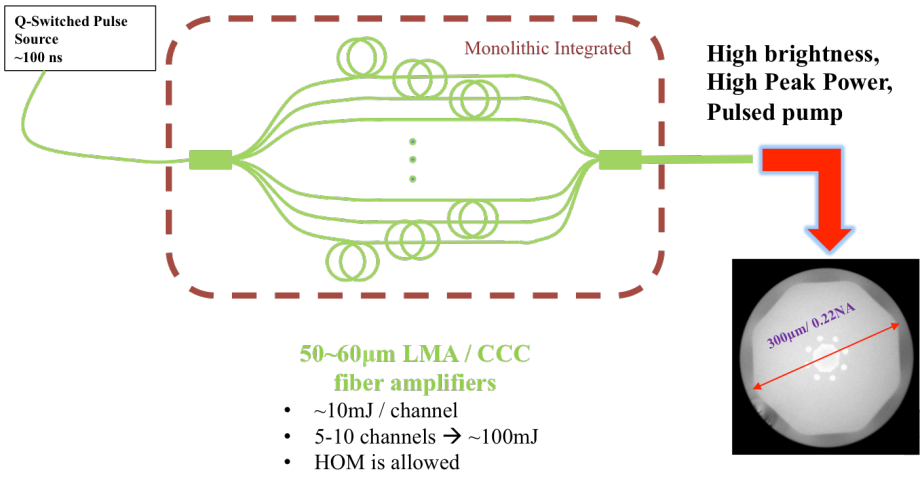

Figure 6.4: Schmetic illustration of pulsed pumping source with high brightness and high peak power by combining multi-channel Q-switched fiber laser amplifiers.

6.3.2 Analytical analysis of extractable energy from a pulse pumped burst operation

As stated above, with pulse repetition rate at around GHz, the amplification process within the pump pulse could be evaluated from a steady state of quasi-CW viewpoint as long as the pump pulse begins ahead the injection of burst, which allows the initial built-up of upper level population inversion. One can estimate the extractable power of this quasi-CW operation following the rate equations.

Aforementioned in Chapter II, a 2-level system model could be used for Yb-doped fiber amplifiers. The upper level population as well as pumping and signal power distribution along the fiber is governed by rate equations as follows [122]:

$$\frac{dN_2}{dt} = -(R_{21} + W_{21} + A_{21})N_2 + (R_{12} + W_{12})N_1 \quad (6.1)$$

$$\frac{dP_p}{dz} = -\sigma_{ap}\Gamma_p N_1 P_p + \sigma_{ep}\Gamma_p N_2 P_p \quad (6.2)$$

$$\pm\frac{dP_s^{\pm}}{dz} = \sigma_{es}\Gamma_s N_2 P_s^{\pm} - \sigma_{as}\Gamma_s N_1 P_s^{\pm} \tag{6.3}$$

where $A_{21} = 1/\tau$ is the upper-level life time of the doping ions. The transition rates of pump and signal are given by:

$$R_{12} = \frac{\sigma_{ap}\Gamma_p P_p}{h\nu_p A}; \qquad R_{21} = \frac{\sigma_{ep}\Gamma_p P_p}{h\nu_p A} \tag{6.4}$$

$$W_{12} = \frac{\sigma_{as}\Gamma_s P_s^{\pm}}{h\nu_s A}; \qquad W_{21} = \frac{\sigma_{es}\Gamma_s P_s^{\pm}}{h\nu_s A} \tag{6.5}$$

where σ_{es} and σ_{ap} are cross-sections of emission at signal wavelength and absorption at pumping wavelength respectively. A is the core area of fiber. Γ_p is pump filling factor and Γ_s is mode filling factor to the fiber core.

From Eqn. (6.1) the dynamics of upper-level population N_2 started from 0 is given by:

$$N_2(z,t) = \frac{(W_{12}+R_{12})(1-\exp(-\omega t))}{\omega} N_{tot} \tag{6.6}$$

where $\omega = (R_{12} + R_{21}) + (W_{12} + W_{21}) + A_{21}$ is the total transition rate of the system. Assuming $P_s^{\pm} \cong 0$, one can get the N_2 dynamics during the building up of small signal population with the steady state population given by:

$$N_{20} = \frac{R_{12}}{(R_{12}+R_{21})+A_{21}} N \tag{6.7}$$

Also, the transition rate ω now is also the effective gain recovery rate of the system, which determines how fast the upper-level population could reach steady state with certain pumping power:

$$\frac{1}{\omega} = \tau_{eff} = \frac{\tau}{1+{P_p}/{P_{p.sat}}} \tag{6.8}$$

where the pump saturation power $P_{p.sat} = \frac{h\nu_p A}{(\sigma_{ep}+\sigma_{ap})\Gamma_p \tau}$, is about 5W for 55μm CCC fiber with pump wavelength at 976nm. The small signal population N_{20} and effective gain recovery time τ_{eff} are both key parameters for characterization of the performance of a fiber amplifier.

With $P_s^{\pm} > 0$, a steady-state solution for upper-level population N_2 during the amplification can be computed as:

$$N_2 = \frac{R_{12}+W_{12}}{(R_{12}+R_{21})+(W_{12}+W_{21})+A_{21}} N \tag{6.9}$$

For amplifier with counter-pumping scheme, using Eqn. (6.7) and (6.9), Eqn. (6.3) can be rewritten as:

$$\frac{dP_s^-}{dz} = -\sigma_{es}\Gamma_s N_{20} \frac{(R_{12}+R_{21})+A_{21}}{(R_{12}+R_{21})+(W_{12}+W_{21})+A_{21}} P_s^- \tag{6.10}$$

Integration of Eqn. (8) provides with the solution:

$$P_{s.sat}(P_{out} - P_{in}) + \ln\left(\frac{P_{out}}{P_{in}}\right) = \sigma_{es}\Gamma_s N_{20} L \tag{6.11}$$

Where $P_{s.sat} = \frac{h\nu_s A}{(\sigma_{es}+\sigma_{as})\Gamma_s \tau_{eff}}$ is the saturation power at signal wavelength. The term on right-hand side of the equation is natural logarithm of small signal gain $\ln(G_0)$ and the second term on left-hand side is the natural logarithm of gain of the signal $\ln(G)$. Therefore one can get an implicit relationship between small signal gain, input seeding power and gain of the amplifier following Eqn. (6.11) as:

$$G = G_0 \exp\left(-\frac{(G-1)P_{in}}{P_{s.sat}}\right) \tag{6.12}$$

Furthermore, the extractable power from the amplifier can also be derived as:

$$P_{ext} = P_{out} - P_{in} = \ln\left(\frac{G_0}{G}\right) \cdot P_{s.sat} \tag{6.13}$$

In burst amplification, the extractable power is the average power of the burst. And one can easily get the extractable energy as:

$$\mathrm{E_{ext}} = \ln\left(\frac{G_0}{G}\right) \cdot \mathrm{P_{s.sat}} \cdot t_{burst} \tag{6.15}$$

Also the ultimate power available would be the extractable with the system under strongly saturation:

$$\mathrm{P_{avail}} = \lim_{G\to 1} \ln\left(\frac{G_0}{G}\right) \cdot \mathrm{P_{s.sat}} = \frac{\mathrm{N_{20}h\nu_s}}{\tau_{eff}} V \tag{6.16}$$

Eqn. (6.16) means that under optimal situation, one can extract the energy store with population inversion under small signal gain once every effective gain recovery time. Since from the definition, effective gain recovery time is dependent on the pumping rate, the stronger the pumping power is, the more power one can extract within a short period. Consequently, one can always extract multiple times of extractable energy for single pulse operation with CW pumping, as long as the effective gain recovery time is shorter than the burst duration, since the maximum available Energy from the amplifier is then given by:

$$\mathrm{E_{avail}} = \lim_{G\to 1} \ln\left(\frac{G_0}{G}\right) \cdot \mathrm{P_{s.sat}} \cdot t_{burst} = \mathrm{N_{20}h\nu_s} V \cdot \frac{t_{burst}}{\tau_{eff}} \tag{6.17}$$

For amplifier with strong pumping power, the integration of a varying value for saturation power over the signal power amplification along the fiber must be taken into consideration for the first term on the left-hand side of Eqn. (6.11) as:

$$\int_{\mathrm{P_{in}}}^{\mathrm{P_{out}}} \mathrm{P_{s.sat}}(z) d\mathrm{P_s^-} + \ln\left(\frac{\mathrm{P_{out}}}{\mathrm{P_{in}}}\right) = \sigma_{\mathrm{es}}\Gamma_{\mathrm{s}}\mathrm{N_{20}}L \tag{6.18}$$

For pump power larger than 1kW, τ_{eff} can be approximated as $\frac{\mathrm{P_{p.sat}}\tau}{\mathrm{P_p}}$, and therefore, $\mathrm{P_{s.sat}}$ is linearly proportional to the pump power. The integration of $\mathrm{P_{s.sat}}$ over the signal power

amplification could be expressed as the effective saturated power multiplies by the extracted power:

$$\int_{P_{in}}^{P_{out}} P_{s.sat}(z) dP_s^- = P_{s.sat.eff} \cdot (P_{out} - P_{in}) \tag{6.19}$$

where the effective saturated power is given by:

$$P_{s.sat.eff} = \frac{h\nu_s A}{(\sigma_{es}+\sigma_{as})\Gamma_s \tau P_{p.sat}} \cdot \frac{\int_{P_{in}}^{P_{out}} P_p(z) dP_s^-}{(P_{out}-P_{in})} \tag{6.20}$$

During the signal amplification process along the fiber, the gain in the signal is linearly proportional to the absorption of the pump for strong pumped system due to the energy transfer nature of the laser medium, and thus there is also a linear dependence of pump power to the signal power along the fiber. The effective saturated power can be approximated as:

$$P_{s.sat.eff} = \frac{h\nu_s A}{(\sigma_{es}+\sigma_{as})\Gamma_s \tau P_{p.sat}} \cdot \frac{(P_{pout}+P_{pin})}{2} \tag{6.21}$$

As a result, the effective saturation power for signal wavelength is given by the intermediate value of the pump power along the fiber. For system with strong absorption of the pump, which is larger than 20dB, this intermediate value of the pump power could be count as half of the input pump power, and hence:

$$P_{s.sat.eff} = \frac{h\nu_s A}{2(\sigma_{es}+\sigma_{as})\Gamma_s \tau_{eff}} \tag{6.22}$$

In the following simulation for extractable energy based on Eqn. (6.15), saturation power $P_{s.sat}$ is substituted by $P_{s.sat.eff}$ in all the case.

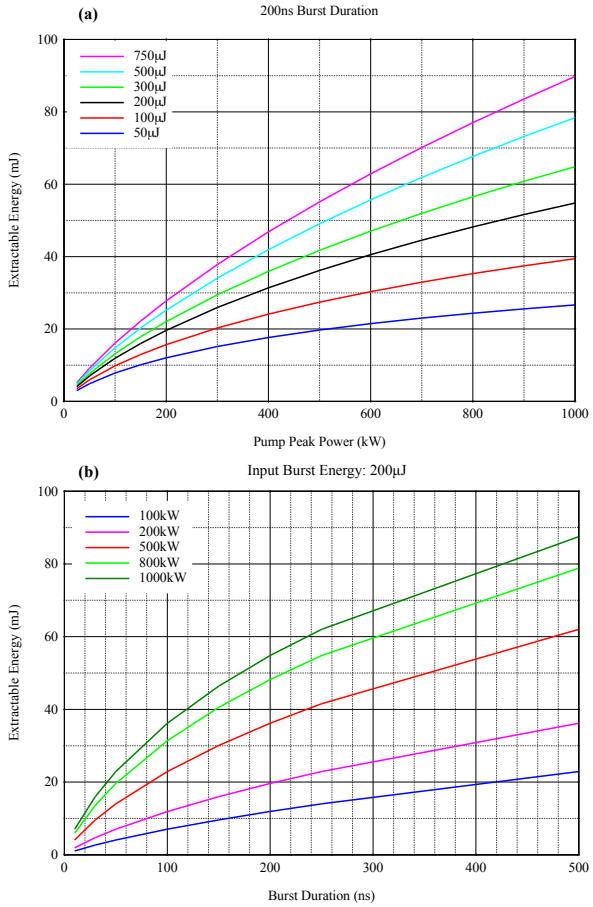

Figure 6.5: Extractable energy of burst amplification in a 2m, 55μm CCC fiber amplifier with assumption that the pump pulse is square shaped. (a) Extractable energy of a 200ns burst versus various pump peak power. The different color of the curves represents different input burst energy respectively, ranging from 50μJ to 750μJ. (b) Extractable energy of a burst with input energy of 200μJ versus various burst durations. Different color of the curves is for different pump peak powers respectively, ranging from 100kW to 1000kW

Fig. 6.5 depicts the calculated extractable energy with various pump peak powers, burst durations as well as burst input energies from a burst amplifier based on a 2m piece of 55μm CCC fiber, following Eqn. (6.15) with assumption of small signal gain G_0 as 30dB. From the simulation result, one could predict that with carefully selection of input energy and duration of the burst as well as pump peak power, the extractable energy from a burst operation with pulsed

pumping is much more than that restricted by ASE with CW pumped single pulse amplification. Tens of milli-Joule is achievable from a single channel of fiber amplifier with the final stage base on a 55μm CCC fiber and even over 100mJ burst output may be realized.

6.3.3 Quasi analytical analysis of extractable energy of burst operation based on amplifier dynamics

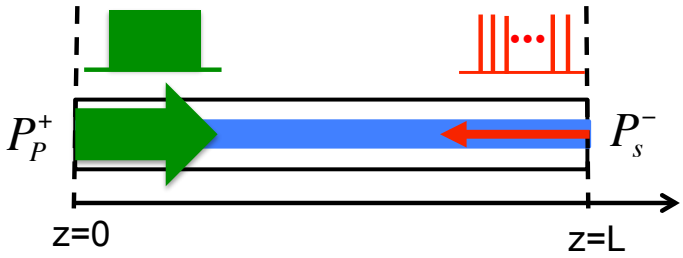

Figure 6.6: Illustration of burst amplification with pulsed pumping in a counter-propagation scheme.

Although one can predict the extractable energy from the pulse pumped burst operation based on the quasi-CW rate equation model aforementioned, in practical case, this assessment is a propagation length independent estimation. Furthermore, since the duration and repetition rate of pulses within the burst would largely affect the dynamics of upper-level population and thus the actual gain experienced. Moreover, to have the burst operation approximating to a quasi-CW operation, a population inversion built up is required before the burst injection other than running the pulses at a high repetition rate. Especially, for counter-pumping scheme as shown in Fig. 6.6, which is commonly used in high energy systems, the pump pulse must arrive at the seeding end before the burst so that the seeding burst is fully amplified. As a result, careful designs of the amplification parameters such as duration and timing of the pumping pulse, burst duration, input energy as well as in-burst-pulse repetition are pre-requisites for practical operation. To meet this end, a more accurate model based on the dynamics of upper-level population during the burst operation is built.

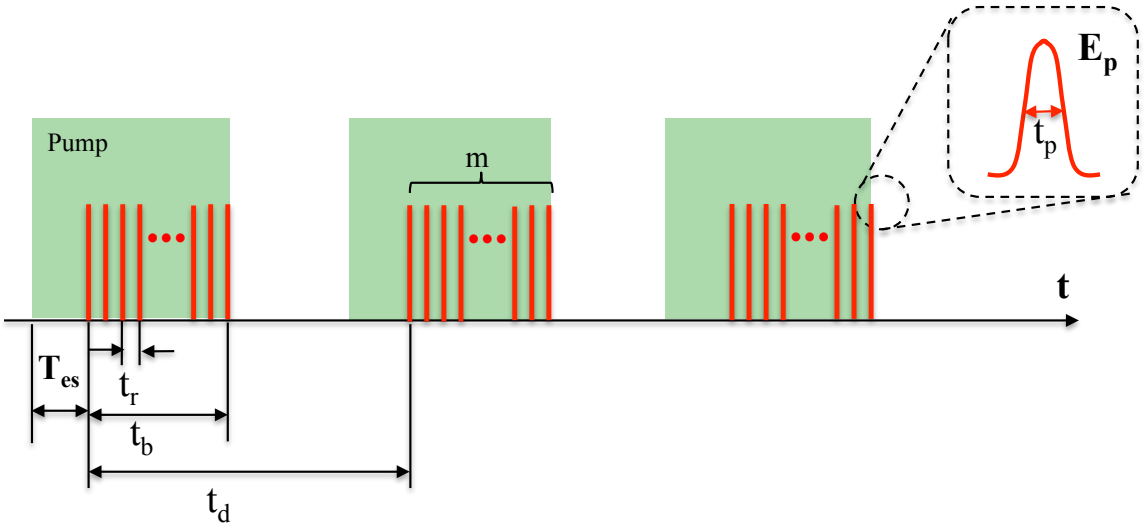

Figure 6.7: Illustration of pumping pulse and burst signal sequences in time domain. T_{es} is time offset between the starts of pumping pulse and burst at the pump end. m is the number of pulses in the burst. t_r is separation between pulses, t_b is the burst duration and t_d is separation between bursts.

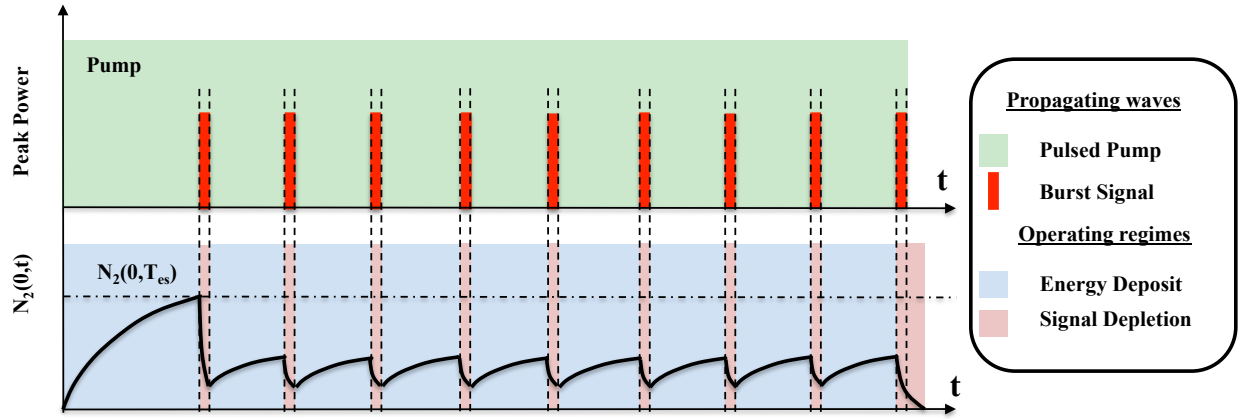

Figure 6.8: Schematic description of operating regimes for energy depositing and signal depleting. $N_2(0,T_{es})$ is the maximum upper-level population limit at z=0 before ASE dominate the depletion.

In Fig. 6.7, the timing for pumping pulse and burst signal are illustrated. The in-burst pulses have a fixed duration of t_p and separated by t_r to each other. With m pulses in the burst, the total width of the burst is denoted by t_b with its separation t_d as the inverse of burst repetition rate. T_{es} represents the timing offset between the pump pulse and burst at pump end of the fiber, z=0. With signal propagating in opposite direction as the pump, T_{es} larger than twice the

traveling time of light through the fiber must be satisfied to ensure no absorption for the first pulse of the burst during the propagation towards pumping end. Fig. 6.8 shows dynamic of pump and signal power as well as upper-level population at pumping end within one pumping pulse. When pulsed pump is applied, the operating regime may be divided into two time regimes: energy depositing regime, when the upper-level population is built with absence of signal pulse, and signal depletion regime during each pulse. For individual pulse as long as the input pulse intensity $I_{in}(t)$ is known, the intensity of output pulse during each pulse is governed by [108]:

$$\mathrm{I_{out}(t)} = \frac{\mathrm{G_0}}{\mathrm{G_0 - (G_0 - 1)\exp\left[-\int_{t_0}^{t} I_{in}(t)dt / U_{sat}\right]}}\,\mathrm{I_{in}(t)} \tag{6.23}$$

where G_0 is the small signal gain of the fiber for each pulse, which is dependent on the integration of upper-level population density $\mathrm{N_{2int}(L,t)}$ over the whole fiber length, at the beginning of pulse injection:

$$G_0 = \exp\left(\Gamma_s \left(\sigma_e^{\lambda_s} + \sigma_a^{\lambda_s}\right) \mathrm{N_{2int}(L,t)} - \left(\Gamma_s \sigma_a^{\lambda s} N_{tot} + \alpha_s(\lambda_s)\right) L\right) \tag{6.24}$$

where $\mathrm{N_{2int}(L,t)} = \int_0^L N_2\left(z, t - \frac{n_c z}{c}\right) dz$ for the case with counter-pumping scheme.

In this way, the amplified burst amplitude and thus total extractable energy could be calculated once the dynamic of upper-level population density $N_2(z,t)$ along the whole fiber during the burst is known.

The general solution for time dependent upper-level population distribution governed by Eqn.(6.1) along a counter-pumped amplifier fiber is given by:

$$N_2(z,t) = \frac{(B - (W_{12} + R_{12})\, N_{tot}) \exp\left(-\omega\left(t - t_0 - \frac{n_c z}{c}\right)\right) + (W_{12} + R_{12}) N_{tot}}{\omega} \tag{6.25}$$

where n_c is the refractive index of fiber core. t_0 is the time point when the transition begins. B is determined by the initial value of $N_2(z, t_0)$ of the transition as:

$$B = N_2(z,t_0)(W_{21} + W_{12} + R_{12} + R_{21} + A_2) \tag{6.26.1}$$

And the transition rate ω is:

$$\omega = W_{21} + W_{12} + R_{12} + R_{21} + A_2 \tag{6.26.2}$$

During the energy deposition before burst arrival, $t_0 = 0$, $W_{12} = W_{12} = 0$, and B=0. $N_2(z,t)$ is hence given by:

$$N_2(z,t) = \frac{R_{12}N_{tot}[1-\exp\left(-\omega_{es}\left(t-\frac{n_c z}{c}\right)\right)]}{\omega_{es}} \tag{6.27}$$

where the transition rate $\omega_{es} = R_{12} + R_{21} + A_2$, which is also the inverse of gain recovery time. Subsequently, the integration of $N_2(z,t)$ over the whole fiber length is:

$$\mathrm{N}_{2int}(\mathrm{L},\mathrm{t}) = \frac{R_{12}N_{tot}}{\omega_{es}}\left[L - \frac{c\cdot\exp(-\omega_{es}t)}{2n\omega_{es}}\left(\exp\left(\frac{2n\omega_{es}L}{c}\right) - 1\right)\right] \tag{6.28}$$

The maximum value of $\mathrm{N}_{2int}(\mathrm{L},\mathrm{T_{es}})$ when burst arrives at the pump end is limited by the domination of ASE depletion, beyond which level the deposited energy would transferred into ASE power and restrict the gain at signal wavelength. As discussed in reference [121], this point is defined as when the emission rate of ASE equals to spontaneous emission rate of upper-level population, i.e. $1/\tau_2$. Similar as the derivation in [121], but with a simplified expression of spontaneous emission seeds ASE band as:

$$SE(z,t,\lambda) = 2\frac{hc^2}{\lambda^3}\sigma_e^{\lambda}N_2(z,t) \tag{6.29}$$

the relationship between fiber parameters and the maximum upper level population integral ($\mathrm{N}_{2int}(\mathrm{L},\mathrm{T_{es}})$) along the entire fiber at the end of energy storage is given by:

$$\frac{A}{2\tau_2 c} = \int_{B.W.} \frac{\exp\left(\Gamma_{ASE}(\sigma_e^{\lambda}+\sigma_a^{\lambda})\mathrm{N}_{2int}(\mathrm{L},\mathrm{T_{es}}) - \left(\Gamma_{ASE}\sigma_a^{\lambda}n_{tot} + \alpha_s(\lambda)\right)L\right) - 1}{1 - \frac{\left(\Gamma_{ASE}\sigma_a^{\lambda}n_{tot}+\alpha_s(\lambda)\right)L}{\Gamma_{ASE}\left(\sigma_e^{\lambda}+\sigma_a^{\lambda}\right)\mathrm{N}_{2int}(\mathrm{L},\mathrm{T_{es}})}} \frac{\sigma_a^{\lambda}}{\lambda^2}\,\mathrm{d}\lambda \tag{6.30}$$

where $\sigma_e^\lambda, \sigma_a^\lambda$ are the Yb^{3+} emission and absorption cross sections at ASE wavelength respectively. $\alpha_s(\lambda)$ is the loss rate of ASE. Γ_{ASE} is the overlap integral between the ASE and doped core. Once $N_{2int}(L, T_{es})$ is solved from Eqn. (6.30), initial small signal gain G_0 for the first pulse as well as maximum time offset T_{es} allowed before significant ASE depletion is derived following Eqn. (6.24) and (6.28).

$$T_{es.max} = -\frac{1}{\omega_{es}} \ln \left[\frac{\frac{2n_c\omega_{es}}{c}\left(L-\frac{\omega_{es}N_{2int}(L,T_{es})}{R_{12}N_{tot}}\right)}{\exp\left(\frac{2n_c\omega_{es}L}{c}\right)-1}\right] \quad (6.31)$$

From (6.31), it is clear that value of $T_{es.max}$ is inversely dependent on the transition rate ω_{es} and pump absorption rate R_{12}, and hence it is indeed inversely dependent on the pumping power. The larger the power of pump pulse, the shorter the maximum time offset between pump pulse and signal burst is allowed before the ASE onset.

Following (6.27), one can also get the distribution of upper-level population at the at the arrival of the first pulse: $N_2\left(z, T_{es.max} - \frac{n_c z}{c}\right)$, which is also the initial condition for the first signal depletion regime. In calculation for N_2, $\exp\left(-\omega_{es}\left(t - \frac{n_c z}{c}\right)\right) < 1$ must be satisfied, since in practice, upper level population value is no more than that at the steady state. Consequently, $T_{es.max} - \frac{2n_c L}{c} > 0$ is requested.

By calculating the intensity distribution for amplified pulse following Eqn. (6.23), one can get the transition of $N_2(0,t)$ during the signal depletion of first pulse following formula (6.25) with the initial value of upper-level population $N_2(0, T_{es.max})$. The transition of $N_2(L,t)$ can also be computed following similar procedure. At seeding end z=L, pump power can be computed by utilizing the numerical model for power distribution calculation for counter-pumped fiber amplifier presented in Chapter II, with the value for input pump power as average power of

pumping pulse while the seeding power as the average power of the burst. Now that the upper-level populations at both ends of the fiber are known for the first pulse depletion regime, the values at the end of the pulse could be served as initial condition for the next energy depositing regime.

Still following expression in (6.25) but with $t_0 = \mathrm{T_{es.max}} + \mathrm{t}_p$, $W_{12} = W_{12} = 0$, and B=$N_2(z, t_0 - \frac{n_c z}{c})(R_{12} + R_{21} + A_2)$, the upper-level population at two ends of the fiber over the depositing period can be achieved. With assumption that the amplifier is under strong pumping condition, which is true for high peak power pulsed pumping scheme, the upper-level population distribution along the fiber is linearly increased from the pump end to the seeding end and hence the integration of $N_2(z,t)$ over the whole fiber length right before the second pulse is given by:

$$\mathrm{N}_{2int}(\mathrm{L}, t_0 + \mathrm{t}_r) = \frac{N_2(0, t_0 + \mathrm{t}_r) + N_2(L, t_0 + \mathrm{t}_r - \frac{n_c z}{c})}{2} L \tag{6.32}$$

Using (6.23-24) and (6.32), the small signal gain before the second pulse and thus the output pulse shape of it may be computed. Repeating the process of upper-level population dynamic calculation for signal depletion and energy depositing regimes as well as the output pulse shape computing for the rest of the burst as that of the first pulse, the extracted energy after amplification is obtained.

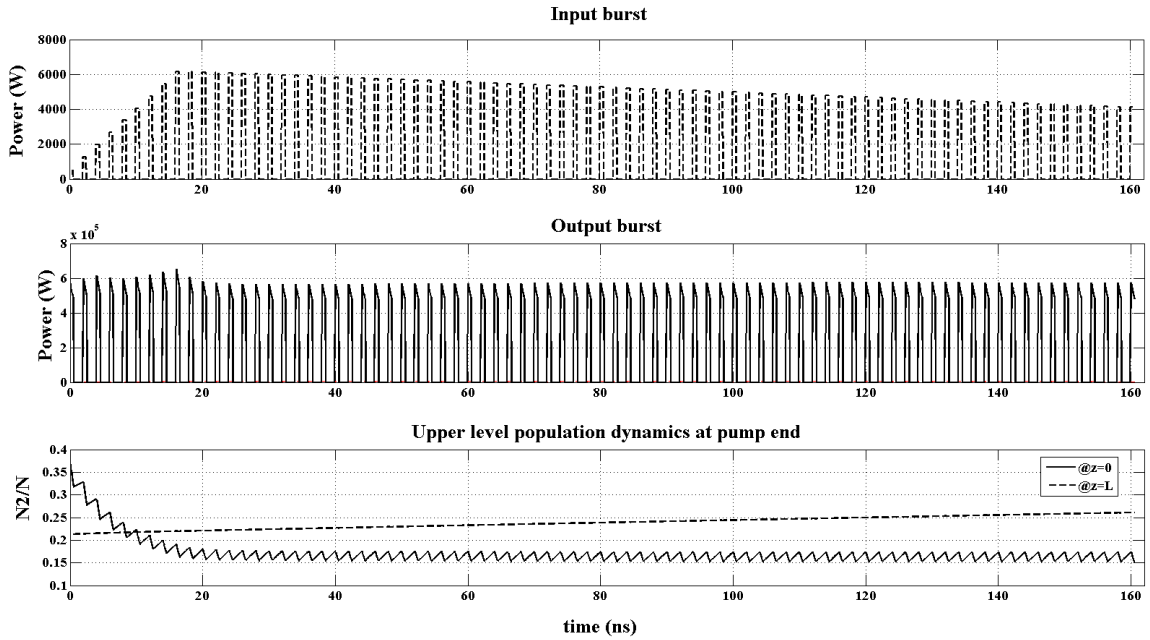

Figure 6.9: Simulation result of burst amplification and upper-level population dynamics for input burst of total energy 200μJ. The peak power of the squared pump pulse is 150kW. Pulse repetition rate within the burst is 0.5GHz.

Fig. 6.9 shows an example of simulation results for burst amplification and the dynamic of upper-level population at fiber ends during the burst. A 2m long 55μm Yb-doped CCC fiber with parameters introduced in Table 5.1 is used in this calculation. The pump absorption ratio for this fiber is about 10dB/m at 976nm. Burst repetition rate ($1/t_d$) is assumed to be 5kHz, and the repetition rate of pulses ($1/t_r$) within burst is 0.5GHz. Number of pulses within the burst is assumed to be 81 as for the case of 4×4 multiplexing of CPS. The pulse duration t_p is around 0.5ns as be restricted by the grating size in practical situation. Pump wavelength is assumed at 976nm and the burst central wavelength is around 1064nm. To simplify the calculation, a square shape for pump pulse is applied with a peak power of 150kW. The maximum time offset for population inversion built up before the burst arrives at the pump end can be first computed as 32.2ns. The total energy within the input burst is assumed to be 200μJ. And the shape of the input burst is modified to achieve a square shaped output burst after amplification as demanded

for good stacking efficiency of CPS. The total energy in the output burst is 21.4mJ. From Fig. 6.8 it is clear that after depletion of the deposited energy before the burst injection, which is around 20ns, the amplification of the rest of the burst is at a quasi-steady state, with upper-level population at pumping end remain at a fixed level while that at seeding end grows very slowly.

Therefore, with this quasi-analytical model, pre-design of the synchronization of the pumping pulse and burst signal as well as selection of operation parameters of the burst such as pulse repetition rate and input burst energy could be done to optimizing the energy extraction. Furthermore, it also provides an estimation for the shape of the input burst which would evolved into the requested output burst shape for optimization of the stacking efficiency in later combining stages.

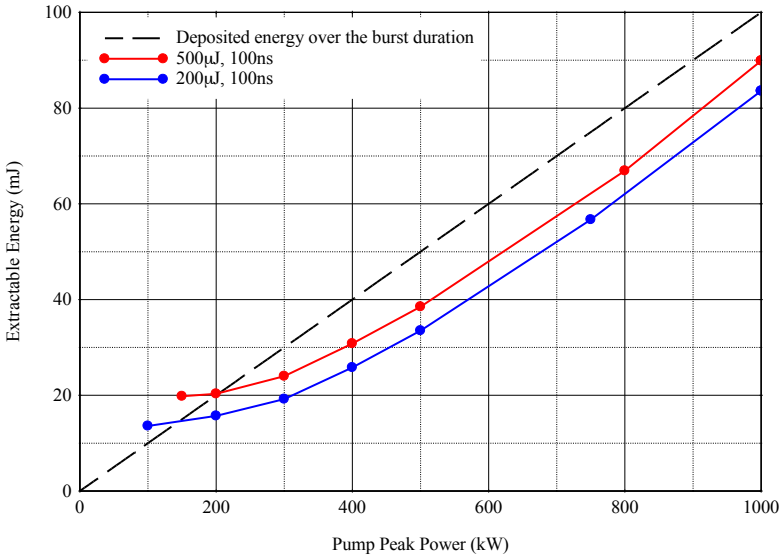

Figure 6.10: Comparison of simulation results for extractable energy from a 2m long 55μm CCC fiber amplifier following the quasi-analytical modeling with the deposited energy over the burst duration. The solid curves are results from the quasi-analytical model based on the dynamics of upper-level population, while the dashed line is the ultimated deposited energy with the pump pulse over the burst duration. The curves in red are simulation with a 100ns input burst of 500μJ; the blues ones are that with a 100ns input burst with 200μJ.

Comparison of simulation results following the quasi-analytical model described in this section and the ultimate deposited pump energy over the burst is depicted in Fig. 6.10. The

extractable energy for a 100ns burst with input energy of 200μJ and 500μJ were computed under various pump peak powers respectively. The solid curves are calculation following dynamics of upper-level population while the dashed line is calculated by assuming all the pump energy is deposited into the amplifier during the burst duration. The difference of extractable energy to the deposited pump energy at low pump peak power region is due to the extraction of pre-deposit pump energy before the burst injected. For calculation with high peak pump powers (>250kW)), the pump peak power before the burst injection is assumed to be as 250kW to satisfy the requirement of T_{es} larger than twice the light traveling time along the fiber. And with the relative much smaller pre-deposit pump energy compared to the total energy over the burst duration, the extractable energy is proportional to the deposit energy with a ratio close to the quantum efficiency. And according to the simulation, close to 100mJ is achievable as long as the deposited energy from pump pulse is sufficient during the burst duration. In conclusion, for burst operation with this novel pumping approach, the extractable energy from a single fiber amplifier channel could be one order of magnitude larger than that was with conventional CW pumping scheme. And this would greatly reduce the complexity of further coherent combining system for multi-Joule laser generation.

6.4 Conclusion

A pulsed pumping for coherent pulse stacking amplification technique was proposed and analyzed theoretically as a solution to overcome limits set by ASE-limited energy storage. Both analytical and quasi-analytical models were developed to explore energy extraction with such pulsed pumping, and up to >100mj energy extraction from a single fiber amplifier channel is predicted according to the simulation. This offers a very promising path to increasing FCPA pulse energies by up to two orders of magnitude. When applied to coherently combined FCPA

arrays with CPS scheme, this could lead to relatively small (~10 - 100 parallel channels) array sizes of future high-power laser-plasma accelerator drivers.

Chapter 7

Conclusion and Future Work

7.1 Conclusion

This thesis is dedicated to the exploration and demonstration of high power and high pulse energy performance of a novel fiber technology: Chirally-Coupled-Core (CCC) fibers. Unprecedented CW high power and high energy nano-second pulses have been demonstrated. The feasibility of CCC fiber as integratable component for practical monolithic fiber laser systems was studied. A novel energy extraction strategy based on pulsed pumping in conjunction CPS with CCC fiber amplifier was proposed.

The investigation starts from developing of simulation tools for power distribution along fiber as well as 2D temperature distribution in high power operation. By combining these two models together, guidance for selection of fiber length, pump wavelength and cooling approach in high power fiber laser and amplifiers is provided, which is essential for optimization of the power scaling process. One concern for large core fiber lasers is that the influence of fundamental mode loss due to various mode stripping approaches, such as bending and coupling, on system efficiency. Both analytical and numerical models for fiber amplifier show that the efficiency of fiber amplifier and lasers is decreasing with increasing leakage loss of the fundamental mode in a fiber, leading to constraints on the maximum tolerable loss, as a design requirement of effectively single-mode fibers.

One critical requirement of coherent combining system is the polarization preservation of each component. For CCC fiber, polarization maintaining has been observed in various experiments, while no HiBi elements were present in these fibers. A thorough exploration and understanding of the mechanism behind this polarization preservation performance of CCC fiber was accomplished for the first time. It reveals that for CCC fiber with spun structure introduced to create the helical side core, an overall effectively low birefringence is realized. This Lo-Bi nature also enables insensitivity of CCC fiber polarization preservation to environment temperature variations. Furthermore, the robust and pure single mode performance of CCC fiber distinguishes it from conventional LMA fibers with immunity to modal scattering induced polarization degradation, which could be triggered by external stress perturbation, drifting of the alignment an etc.

Moreover, in practical packaged systems, coiling of CCC fiber induces linear birefringence by bending as well as circular birefringence by the bending related twisting of the fiber. However, due to the Lo-Bi nature and insensitivity to modal scattering of CCC fiber, a linear polarization could always be reproduced at the output end as long as a linear polarization with certain direction is injected. The azimuth angle of the input linear polarization depends on the fiber length. For most practical high power fiber laser systems, all time polarization maintanence along the fiber is not necessarily required. Therefore, the reproduction of linear polarization with bent CCC fiber is applicable as long as the linearity and direction of this reproduced linear polarization is insensitive to external perturbations. And this uncovers a new regime for polarization controlling in high power fiber systems.

Based on the understanding of polarization preservation with CCC fiber, two approaches were proposed to enhance the polarization stability: i) wound fiber around a drum to create large

linear birefringence, ii) twisting the fiber to produce high circular birefringence. The selection between these two methods is related to the real applications of the fiber system.

To explore the feasibility of CCC fiber for high power fiber laser arrays, single frequency amplification up to nearly 600W with no SBS onset was achieved with single transverse mode and linear polarization. Due to the large core and high doping concentration required short interaction length, CCC fiber also exhibits certain mitigation for the SBS. This high power demonstration shows potential of CCC fiber as components of high power fiber laser array.

To further study the applicability of CCC fiber for pulse and expecially ultra-shor pulse systems, nanosecond pulse amplification was conducted with 55μm CCC fiber. 9.1mJ and close 1MW was demonstrated in 10ns pulses output from the CCC fiber. We found that effectively single-mode performance of the CCC fiber core results in increased stored pulse energy, compared to even large core LMA fibers.

A novel technology for temporal coherent combining: coherent pulse stacking (CPS) has been recently demonstrated with output energy up to 1ns with 850ps pulses based on 55μm CCC fiber amplifier [42]. In reference to this approach, we propose to enhance the energy extractable from a single fiber amplifier channel by using a pulsed pumping scheme with high peak power. With a burst of high frequency pulses with duration of tens to over hundreds of nanosecond, the pulsed pumped amplification may be analog to a quasi-CW operation, in which, small signal gain stored energy is extracted every gain recovery time. With high peak power induced very short gain recovery time at order of tens of nanosecond, the extractable energy from such burst amplification is predicted to be multiple times of the small signal gain stored energy, which is the extractable energy in conventional pulse amplification. This remarkable improvement of

energy extraction from a single fiber amplifier channel would greatly reduce the complexity of coherent combining fiber lasers towards few Joule regime.

All the presented exploration and analysis work establishes a knowledge basis, for designing large core CCC fiber based monolithically-integrated high power and high energy modules for building coherent combining fiber laser arrays, particularly for high peak power (TW~PW) kHz repetition rate, ultrashort-pulse laser systems.

7.2 Future work

There remains a number of important research topics to be explored, as a continuation of the thesis work presented here.

7.2.1 Investigation on relations between HOM leakage loss and extractable energy in pulsed CCC amplifier.

As shown in ChapterV, 9mJ pulse energy was achieved with CCC fiber based pulse amplifier. However, it has already exceeds 10 times of saturation energy of the amplifier at 1040nm. One possible reason for this enhancement is that the high leakage loss of HOM in CCC fiber suppresses the ASE power built-up during energy storage regime. Therefore the small signal gain population inversion exceeds the conventional 30dB limit set by ASE depletion. More detailed investigation is needed to characterize and fully understand this behavior, which provides a promising progress on further energy scaling with CCC fiber.

7.2.2 Exploration on nonlinear polarization effects in CCC fiber

Nonlinear polarization effects have been observed at high peak powers in pulsed CCC fiber amplifiers. Further exploration and understanding of these effects is necessary as an extension of the current study on linear polarization in CCC fibers.

7.2.3 Developing the high peak pulsed pumping source

Presented theoretical analysis indicates that significant increase in energy extraction from a single fiber amplifier channel is possible with the novel pulsed pumping scheme and in conjunction to CPS scheme. Construction of a high peak power pulsed pumping source is a pre-requisite for experimental demonstration of exceeding conventional energy extraction from single channel. A possible approach is to construct a monolithic large core fiber amplifier array seeded with Q-switched laser source. With around 60μm core size of LMA or CCC fibers for each amplifier channel, close to 10mJ is achievable. And a combination of 10 such channels, 100mJ would be available. Moreover, this high energy beam also fits the high brightness pumping requirement, regardless of the mode quality in large core fiber channels.

7.2.4 Further demonstration of energy scaling with CCC fiber based cascaded CPS system

One advantage of the CPS technology is that the burst length is not limited by mechanical restrictions. With cascading of multiple CPS cavities, stacking of tens or hundreds of pulses is possible. And thus, with the pulsed pumping scheme proposed in Chapter VI, close to hundred of mJ is achievable in one final pulse from a single fiber amplifier.

BIBLIOGRAPHY

1. A. L. Schawlow and C. H. Townes, “Infrared and optical masers”, Phys. Rev. 112 (6), 1940 (1958).
2. T. H. Maiman, “Stimulated optical radiation in ruby”, Nature 187, 493 (1960)
3. E. Snitzer, 'Proposed fibre cavities for optical masers', J. App. Phys. 32, 36 (1961).
4. Charles J. Koester and Elias Snitzer, "Amplification in a Fiber Laser," Appl. Opt. 3, 1182-1186 (1964)
5. C. A. Burrus and J. Stone, “Nd3+ doped SiO2 lasers in an end-pumped fiber geometry”, Appl. Phys. Lett. 23 (7), 388 (1973)
6. J. Stone and C. A. Burrus, "Neodymium-Doped Fiber Lasers: Room Temperature cw Operation with an Injection Laser Pump," Appl. Opt. 13, 1256-1258 (1974)
7. C. K. Kao, “Nobel Lecture: sand from centuries past: send future voices fast,” Rev. Mod. Phys. 82(3), 2299– 2303 (2010).
8. S. B. Poole, D. N. Payne, and M. E. Fermann, “Fabrication of low loss optical fibres containing rare-earth ions,” Elec- tron. Lett. 21, 737–738 (1985).
9. R. J. Mears, L. Reekie, S. B. Poole, and D. N. Payne, “Neodymium-doped silica single-mode fibre laser,” Elec- tron. Lett. 21, 738–740 (1985).
10. M. C. Farries, P. R. Morkel, and J. E. Townsend. Samarium3+-doped glass laser operating at 651 nm. Electron. Lett., 24(11):709–711, (1988).
11. Makoto Yamada, Makoto Shimizu, Yasutake Ohishi, Terutoki Kanamori, Shouichi Sudo, and Jiro Temmyo. Gain characteristics of Pr3+-doped fluoride fiber amplifier. Electronics and Communications in Japan (Part II: Electronics), 77(4):75–87, (1994).
12. E. Desurvire and J. R. Simpson. Amplification of spontaneous emission in erbium-doped single-mode fibers. J. Lightwave Technology, 7(5):835–845, 1989.
13. D. C. Hanna, R. M. Percival, I. R. Perry, R. G. Smart, P. J. Suni, J. E. Townsend, and A. C. Tropper, “Continuous-wave oscillation of a monomode Ytterbium-doped fiber laser,” Electronics Letters, vol. 24, no. 17, pp. 1111– 1113, 1988
14. C. Ghisler, W. Luthy, and H. P. Weber. Tuning of a Tm3+ : Ho3+: silica fiber laser at 2 μm. IEEE J. Quantum Electron., 31(11):1877–1879, 1995.
15. R. Maurer, Optical waveguide light source. US patent 3,808,549 (1974).
16. E. Snitzer, H. Po, F. Hakimi, R. Tumminelli, and B. C. McCollum, " Double Clad, Offset Core Nd Fiber Laser," Optical Fiber Sensors, Vol. 2 of OSA Technical Digest Series (Optical Society of America, 1988), paper PD5.
17. Minelly, J. D., Taylor, E. R., Jedrzejewski, K. P., Wang, J. & Payne, D. N. Laser-diode-pumped Nd-doped fibre laser with output power>lW. Paper 246 in Proc. CLEO (1992).
18. V. Dominic, S. MacCormack, R. Waarts, S. Sanders, S. Bicknese, R. Dohle, E. Wolak, P.S. Yeh, and E. Zucker. 110 W fibre laser. Electron. Lett., 35(14):1158–1160, 1999.
19. Y. Jeong, J.K. Sahu, R.B. Williams, D.J. Richardson, K. Furusawa, and J. Nilsson. Ytterbium-doped large-core fibre laser with 272-W output power. Electron. Lett., 39(13):977–978, 2003.
20. J. Limpert, A. Liem, H. Zellmer, and A. Tunnermann. 500 W continuous-wave fibre laser with excellent beam quality. Electron. Lett., 39(8):645–647, 2003.
21. Y. Jeong, J. Sahu, D. Payne, and J. Nilsson. Ytterbium-doped large-core fiber laser with 1.36 kW continuous-wave output power. Opt. Express, 12(25):6088–6092, December 2004.
22. Y. Jeong, J.K. Sahu, D.N. Payne, and J. Nilsson. Ytterbium-doped large-core fibre laser with 1-kW of continuous-wave output power. Electron. Lett., 40(8):470–472, 2004.

23. C.-H. Liu, B. Doerfel, F. Heinemann, S. Carter, A. Tankala, J. K. Farroni, and A. Galvanauskas. 810 W continuous-wave and single-transverse-mode fibre laser using 20-μm core Yb-doped double-clad fibre. Electron. Lett., 40(23):1471–1472, 11 Nov. 2004.
24. E. Stiles, "New developments in IPG fiber laser technology," in Proceedings of the 5th International Workshop on Fiber Lasers (2009)
25. C. Jauregui, J. Limpert and A. Tunnermann, "High-power fibre lasers", Nature Photon. 7, 861 (2013)
26. H. M. Pask, R. J. Carman, D. C. Hanna, A. C. Tropper, C. J. Mackechnie, P. R. Barber, and J. M. Dawes. Ytterbium-doped silica fiber lasers: versatile sources for the 1-1.2 μm region. IEEE J. Sel. Top. Quantum Electron., 1(1):2–13, 1995.
27. Röser, F. et al. 131 W 220 fs fibre laser system. Opt. Lett. 30, 2754–2756 (2005).
28. M. Rever, S. Huang, V. Smirnov, E. Rotari, I. Cohanoshi, S. Mokhov, L. Glebov, and A. Galvanauskas. 200w, 350fs fiber cpa system enabled by chirped-volume-bragg-gratings and chirally-coupled-core fiber technology. volume 7580, page 75800Y. SPIE, 2010.
29. Eidam, T. et al. Femtosecond fibre CPA system emitting 830 W average output power. Opt. Lett. 35, 94–96 (2010).
30. S. Webster, F. C. McDonald, A. Villanger, M. J. Soileau, E. W. Van Stryland, D. J. Hagan, B. McIntosh, W. Torruellas, J. Farroni, and K. Tankala, "Optical damage measurements for high peak power ytterbium doped fiber amplifiers", Proc. SPIE 5991, Laser-Induced Damage in Optical Materials: 2005, 599115 (February 07, 2006).
31. G.P. Agrawal, Nonlinear Fiber Optics (Academic Press, 1995)
32. Arlee V. Smith and Jesse J. Smith, "Mode instability in high power fiber amplifiers," Opt. Express 19, 10180-10192 (2011)
33. C. Jauregui, T. Eidam, J. Limpert, and A. Tünnermann, "The impact of modal interference on the beam quality of high-power fiber amplifiers," Opt. Express 19, 3258–3271 (2011)
34. J. Limpert, F. Roser, D. N. Schimpf, E. Seise, T. Eidam, S. Hädrich, J. Rothhardt, C. J. Misas, and A. Tünnermann, "High repetition rate gigawatt peak power fiber laser systems: challenges, design, and experiment," IEEE J. Sel. Top. Quantum Electron. 15(1), 159–169 (2009).
35. W. S. Brocklesby, J. Nilsson, T. Schreiber, J. Limpert, A. Brignon, J. Bourderionnet, L. Lombard, V. Michau, M. Hanna, Y. Zaouter, T. Tajima, G. Mourou, "ICAN as a new laser paradigm for high energy, high average power femtosecond pulses," EPL 223 (6), 1189-1195 (2014)
36. S.M. Redmond, T.Y. Fan, D.J. Ripin, P.A. Thielen, J.E. Rothenberg, and G.D. Goodno, "Diffractive Beam Combining of a 2.5-kW Fiber Laser Array," Advanced Solid-State Photonics (ASSP) AM3A.1 (2012)
37. Arno Klenke, Sven Breitkopf, Marco Kienel, Thomas Gottschall, Tino Eidam, Steffen Hädrich, Jan Rothhardt, Jens Limpert, and Andreas Tünnermann, "530 W, 1.3 mJ, four-channel coherently combined femtosecond fiber chirped-pulse amplification system," Opt. Lett. 38, 2283-2285 (2013)
38. G. J. Swanson, J. R. Leger, and M. Holz, "Aperture filling of phase-locked laser arrays," Opt. Lett. 12(4), 245– 247 (1987)
39. R. Uberna, A. Bratcher, and B. G. Tiemann, "Coherent polarization beam combination," IEEE J. Quantum Electron. 46(8), 1191–1196 (2010).

40. E. C. Cheung, J. G. Ho, G. D. Goodno, R. R. Rice, J. Rothenberg, P. Thielen, M. Weber, and M. Wickham, “Diffractive-optics-based beam combination of a phase-locked fiber laser array,” Opt. Lett. 33(4), 354–356 (2008).
41. M. Kienel, A. Klenke, T. Eidam, S. Hädrich, J. Limpert, and A. Tünnermann, “Energy scaling of femtosecond amplifiers using actively controlled divided-pulse amplification,” Optics letters 39(4), 1049-1052 (2014).
42. T. Zhou, J. Ruppe, C. Zhu, P. Stanfield, J. Nees and A. Galvanauskas, "Coherent pulse stacking amplification", in preparation
43. F. Gires and P. Tournois, “Interferometre utilisable pour la compression d'impulsions lumineuses modulees en frequence”, C. R. Acad. Sci. Paris 258, 6112 (1964)
44. J. E. Rothenberg and G. D. Goodno, " Advances and Limitations in Beam Combination of Kilowatt Fiber Amplifiers," Proc. of SPIE Vol. 7686.
45. ME Fermann. Single-mode excitation of multimode fibers with ultrashort pulses. Opt. Lett., 23(1):52–54, JAN 1 1998.
46. Jeffrey P. Koplow, Dahv A. V. Kliner, and Lew Goldberg. Single-mode operation of a coiled multimode fiber amplifier. Opt. Lett., 25(7):442–444, 2000.
47. T. A. Birks, J. C. Knight, and P. St.J. Russell, "Endlessly single-mode photonic crystal fiber," Opt. Lett. 22, 961-963 (1997)
48. J. C. Knight, “Photonic crystal fibres”, Nature 424, 847 (2003)
49. Limpert, J. et al. J. Limpert, A. Liem, M. Reich, T. Schreiber, S. Nolte, H. Zellmer, A. Tu¨nnermann, J. Bro- eng, A. Petersson, and C. Jakobsen. Low-nonlinearity single-transverse-mode ytterbium-doped photonic crystal fiber amplifier. Opt. Express, 12(7):1313–1319, 2004. Opt. Express 11, 818−823 (2003)
50. J. Limpert, O. Schmidt, J. Rothhardt, F. Röser, T. Schreiber, A. Tünnermann, S. Ermeneux, P. Yvernault, and F. Salin, "Extended single-mode photonic crystal fiber lasers," Opt. Express 14, 2715-2720 (2006)
51. Christopher D. Brooks and Fabio Di Teodoro. Multimegawatt peak-power, single-transverse- mode operation of a 100 μm core diameter, yb-doped rodlike photonic crystal fiber amplifier. Applied Physics Letters, 89(11):111119, 2006.
52. Fabian Stutzki, Florian Jansen, Tino Eidam, Alexander Steinmetz, Cesar Jauregui, Jens Limpert, and Andreas Tünnermann, "High average power large-pitch fiber amplifier with robust single-mode operation," Opt. Lett. 36, 689-691 (2011)
53. Stutzki F, Jansen F, Liem A, Jauregui C, Limpert J et al. 26 mJ, 130 W Q-switched fiber-laser system with near-diffraction-limited beam quality. Opt Lett 2012; 37: 1073–1075.
54. Tino Eidam, Jan Rothhardt, Fabian Stutzki, Florian Jansen, Steffen Hädrich, Henning Carstens, Cesar Jauregui, Jens Limpert, and Andreas Tünnermann, "Fiber chirped-pulse amplification system emitting 3.8 GW peak power," Opt. Express19, 255-260 (2011)
55. Xiuquan Ma, Cheng Zhu, I-Ning Hu, Alex Kaplan, and Almantas Galvanauskas, "Single-mode chirally-coupled-core fibers with larger than 50μm diameter cores," Opt. Express 22, 9206-9219 (2014)
56. X. Ma, C.-H. Liu, G. Chang, and A. Galvanauskas, “Angular-momentum coupled optical waves in chirally- coupled-core fibers,” Opt. Express, 19, 26515-26528 (2011).
57. X. Ma, “Understanding and Controlling Angular Momentum Coupled Optical Waves in Chirally-Coupled- Core (CCC) Fibers,” PhD Thesis, University of Michigan at Ann Arbor.
58. M. Rever, " Compact, Robust Technology for Next-Generation Ultrafast High-Power

Fiber Lasers", PhD Thesis, University of Michigan at Ann Arbor.
59. C. Zhu, I.-N. Hu, X. Ma, L. Siiam, and A. Galvanauskas, “Single-frequency and single-transverse mode Yb-doped CCC fiber MOPA with robust polarization SBS-free 511W output”, ASSP 2011 Paper AMC5
60. I-N. Hu, X. Ma, C. Zhu, W.-Z. Chang, C.-H. Liu, T. Sosnowski, A. Galvanauskas, “Experimental Demonstration of SRS Suppression in Chirally-Coupled-Core Fibers,” ASSP 2012 Paper AT1A.
61. C. Zhu, I.-N. Hu, X. Ma, L. Siiam, and A. Galvanauskas, “Single-frequency and single-transverse mode Yb-doped CCC fiber MOPA with robust polarization SBS-free 511W output”, ASSP 2011 Paper AMC5.
62. M. L. Stock, C.-H. Liu, A. Kuznetsov, G. Tudury, A. Galvanauskas and T. Sosnowski, “Polarized, 100 kW peak power, high brightness nanosecond lasers based on 3C optical fiber,” Proc. SPIE 7914, 79140U (2011).
63. M. J. F. Digonnet (Ed.), Rare Earth Doped Fiber Lasers and Amplifiers. New York: Marcel Dekker, 1993.
64. R. Paschotta, J. Nilsson, A. C. Tropper, and D. C. Hanna, “Ytterbium- doped fiber amplifiers,” IEEE J. Quantum Electron., vol. 33, pp. 1049–1056, July 1997.
65. L. Zenteno. “High-power double-clad fiber lasers”, J. Lightwave Technology, 11(9):1435–1446, 1993.
66. Hansen KP, Olausson CB, Broeng J, et al, “Airclad fiber laser technology”. Opt. Eng. 0001, 50(11):111609 (2011)
67. B. Zintzen, T. Langer, J. Geiger, D. Hoffmann, and P. Loosen, "Heat transport in solid and air-clad fibers for high-power fiber lasers," Opt. Express 15, 16787-16793 (2007)
68. J. Li, K. Duan, Y. Wang, X. Cao, W. Zhao, Y. Guo, and X. Lin, “Theoretical analysis of the heat dissipation mechanism in Yb3+-doped double-clad fiber lasers,” J. Mod. Opt. 55, 459–471 (2008).
69. P. E. Britton, H. L. Offerhaus, D. J. Richardson, P. G. R. Smith, G. W. Ross, and D. C. Hanna, "Parametric oscillator directly pumped by a 1.55-μm erbium-fiber laser," Opt. Lett. 24, 975-977 (1999)
70. B. Willke, “Stabilized lasers for advanced gravitational wave detection,” Laser Photonics Review 4, 780 (2010).
71. M. Karow, C.Zhu, D. Kracht, J. Neumann, A. Glavanauskas, P. Weßels, “Fundamental Gaussian mode content measurements on active large core CCC fibers”, CLEO/Europe and IQEC 2013 Conference Digest, (Optical Society of America, 2013), paper CJ1_6
72. J. D. Love , R. A. Sammut and A. W. Snyder "Birefringence in elliptically deformed fibers", Electron. Lett., vol. 15, pp.615 -616 (1979).
73. M. J. Adams , D. N. Payne and C. M. Ragdale "Birefringence in optical fibers with elliptical cross-section", Electron. Lett., vol. 15, pp.298 -299 (1979) .
74. D. Gloge, "Weakly Guiding Fibers," Appl. Opt. 10, 2252-2258 (1971)
75. Y. Namihira , M. Kudo and Y. Mushiaka "Effect of mechanical stress on the transmission characteristics of optical fibers", Trans. Inst. Electron. Commun. Eng. Japan, vol. 60-C, pp.107 -115 (1977).
76. A. Kumar and R. Ulrich, "Birefringence of optical fiber pressed into a F-groove", Opt. Lett., vol. 6, pp.644 -646 (1981).
77. R. Ulrich , S. C. Rashleigh and W. Eickhoff "Bending-induced birefringence in single

mode fiber", Opt. Lett., vol. 5, pp.273 -275 (1980)
78. S. C. Rashleigh and R. Ulrich "High-birefringence in tension-coiled single-mode fibers", Opt. Lett., vol. 5, pp.354 -356 (1980)
79. R. Ulrich and S. C. Rashleigh "Polarization coupling in kinked single-mode fiber", IEEE J. Quantum Electron., vol. 18, pp.2032 -2039 (1982)
80. R. Ulrich and A. Simon "Polarization optics of twisted single mode fibers", Appl. Opt., vol. 18, pp.2241 -2251 (1979)
81. S.C Rashleigh, "Origins and control of polarization effects in single-mode fibers" Journ. Lightwave Technol., 1, 312-331 (1983).
82. A. Yariv, P. Yeh, Optical waves in crystals: propagation and control of laser radiation (Wiley-Interscience, 2003)
83. Katsuyama, H. Matsumura, and T. Suganuma, "Low loss single polarization fibers," Electron. Lett., vol. 17, pp. 473- 474,1981.
84. S. C. Rashleighand M. J. Marrone, "Polarization holding in a high-birefringence fiber," Electron. Lett., vol. 18, pp. 326-327, 1982.
85. T. Hosaka, K. Okamoto, Y.Mika,Y. Sasaki, and T. Edahiro, "Low-lossingle polarization fibers with asymmetrical strain birefringence," Electron. Lett., vol. 17, pp. 530-531,1980
86. Peter McIntyre and Allan W. Snyder, "Light propagation in twisted anisotropic media: Application to photoreceptors," J. Opt. Soc. Am. 68, 149-157 (1978)
87. A. J. Barlow , J. J. Raraskov-Hansen and D. N. Payne "Birefringence and polarization mode dispersion in spun single mode fibers", Appl. Opt., vol. 20, pp.2962 -2968 (1981)
88. See IPG website at http://www.ipgphotonics.com/apps_materials_multi_yls.htm
89. P.D. Dragic, C.H.L., G.C. Papen and A. Galvanauskas, "Optical fiber with an acoustic guiding layer for stimulated Brillouin scattering suppression," in Conference on Lasers and Electro-Optics, paper CThZ3 (2005).
90. S. Gray, A. Liu, D. T. Walton, J. Wang, M-j Li, X. Chen, A. B. Ruffin, J. A. DeMeritt and L. A. Zenteno, "502 Watt, single transverse mode, narrow linewidth, bidirectionally pumped Yb-doped fiber amplifier," Optics Express 15, 17044-17050 (2007).
91. Y. Jeong, J. Nilsson, J. K. Sahu, D. N. Payne, R. Horley, L. M. B. Hickey, and P. W. Turner, "Power scaling of single-frequency ytterbium-doped fiber master oscillator power amplifier sources up to 500W," IEEE Journal of Selected Topics in Quantum Electronics 13, 546-551 (2007).
92. C. Robin, I. Dajani, C. Vergien, C. Zeringue, and T. M. Shay, "Experimental and theoretical studies of single frequency PCF amplifier with output of 400W," Proc. of SPIE 7580, 75801I-1 -7580I-11 (2010).
93. J. Edgecumbe, et al, "kW-Class, narrow-linewidth counter-pumped fiber amplifiers", SSDLTR Proc., June (2010).
94. Doruk Engin, Wei Lu, Mehmetcan Akbulut, Bruce McIntosh, Horacio Verdun and Shantanu Gupta, "1 kW cw Yb-fiber-amplifier with <0.5GHz linewidth and near-diffraction limited beam-quality for coherent combining application", Proc. SPIE 7914, 791407 (2011).
95. Christian Wirth, Thomas Schreiber, Miroslaw Rekas, Igor Tsybin, Thomas Peschel, Ramona Eberhardt and Andreas Tünnermann, "High-power linear-polarized narrow linewidth photonic crystal fiber amplifier", Proc. SPIE 7580, 75801H (2010);
96. R. G. Smith, "Optical Power Handling Capacity of Low Loss Optical Fibers as Determined by Stimulated Raman and Brillouin Scattering," Appl. Opt. 11, 2489-2494 (1972)

97. P.Kwee,F.Seifert,B.Willke,andK.Danzmann,“Laser beam quality and pointing measurements with an optical resonator,” Rev. Sci. Instrum. 78, 0731031 (2007).
98. M. Hildebrandt, M. Frede, P. Kwee, B. Willke, and D. Kracht, “Single-frequency master-oscillator photonic crystal fiber amplifier with 148 W output power,” Opt. Express 14(23), 11071–11076 (2006).
99. C. Gréverie, A. Brillet, C. N. Man, W. Chaibi, J. P. Coulon, and K. Feliksik, “High power fiber amplifier for Advanced Virgo,” Conference on Lasers and Electro-Optics, OSA Technical Digest (CD) (Optical Society of America, 2010), paper JTuD36.
100. Malte Karow, Chandrajit Basu, Dietmar Kracht, Jörg Neumann, and Peter Weßels, "TEM00 mode content of a two stage single-frequency Yb-doped PCF MOPA with 246 W of output power," Opt. Express 20, 5319-5324 (2012)
101. Craig Robin, Iyad Dajani, and Benjamin Pulford, "Modal instability-suppressing, single-frequency photonic crystal fiber amplifier with 811 W output power," Opt. Lett. 39, 666-669 (2014)
102. M. Karow, J. Neumann, D. Kracht, and P. Weßels, “TEM00 mode content measurements on a 55 μm core diameter passive chirally-coupled core fiber”, submitted to Opt. Lett.
103. Ming-Yuan Cheng, Yu-Chung Chang, Almantas Galvanauskas, Pri Mamidipudi, Rupak Changkakoti, and Peter Gatchell, "High-energy and high-peak-power nanosecond pulse generation with beam quality control in 200-μm core highly multimode Yb-doped fiberamplifiers," Opt. Lett. 30, 358-360 (2005)
104. S. Maryashin, A. Unt, and V. Gapontsev,“10 mJ pulse energy and 200 W average power Yb-doped fiber laser,” Proc. SPIE-Int. Soc. Opt. Eng. 6102, 61020O (2006).
105. K.Hou, S. George, A. G. Mordovanakis, K. Takenoshita, J. Nees, B. Lafontaine, M. Richardson, and A. Galvanauskas, "High power fiber laser driver for efficient EUV lithography source with tin-doped water droplet targets," Opt. Express 16, 965-974 (2008)
106. C. D. Brooks and F. Di Teodoro, “Multimegawatt peak-power, single-transverse-mode operation of a 100 μm core diameter, Yb-doped rodlike photonic crystal fiber amplifier”, Appl. Phys. Lett. 89, 111119 (2006).
107. F. Stutzki, F. Jansen, A. Liem, C. Jauregui, J. Limpert, and A. Tünnermann, "26 mJ, 130 W Q-switched fiber-laser system with near-diffraction-limited beam quality," Opt. Lett. 37, 1073-1075 (2012)
108. A. E. Siegman. Lasers (University Science Books, 1990)
109. B. C. Stuart, M. D. Feit, S. Herman, A. M. Rubenchik, B. W. Shore, and M. D. Perry, "Optical ablation by high-power short-pulse lasers," J. Opt. Soc. Am. B 13, 459-468 (1996)
110. R. W. Boyd, Nonlinear Optics (Academic, Boston, Mass., 1992)
111. Jean-Philippe F`eve, Paul E. Schrader, Roger L. Farrow, and Dahv A. Kliner. Four-wave mixing in nanosecond pulsed fiber amplifiers. Opt. Express, 15(8):4647–4662, April 2007.
112. Zhang, Z., Zhou, X., Sui, Z., Wang, J., Li, H., Liu, Y. and Liu, Y., "Numerical analysis of stimulated inelastic scatterings in ytterbium-doped double-clad fiber amplifier with multi-ns-duration and multi-hundred-kW peak-power output," Opt. Commun. 282, 1186-1190 (2009)
113. Xiuquan Ma, I-Ning Hu, and Almantas Galvanauskas, "Propagation-length independent SRS threshold in chirally-coupled-core fibers," Opt. Express 19, 22575-22581 (2011)
114. RefP. D. Dragic, “Suppression of first order stimulated Raman scattering in erbium-doped fiber laser based LIDAR transmitters through induced bending loss,” Opt. Commun. 250(4-6), 403–410 (2005).

115. J. M. Fini, M. D. Mermelstein, M. F. Yan, R. T. Bise, A. D. Yablon, P. W. Wisk, and M. J. Andrejco, “Distributed suppression of stimulated Raman scattering in an Yb-doped filter-fiber amplifier”, Opt. Lett. **31**, 2550-2552 (2006).
116. D. Strickland and G. Mourou, “Compression of amplified chirped optical pulses,” Optics Communications 56(3), 219 (1985).
117. F. Röser, T. Eidam, J. Rothhardt, O. Schmidt, D. N. Schimpf, J. Limpert, and A. Tünnermann, "Millijoule pulse energy high repetition rate femtosecond fiber chirped-pulse amplification system," Opt. Lett. 32, 3495-3497 (2007)
118. ref.
119. Arno Klenke, Enrico Seise, Stefan Demmler, Jan Rothhardt, Sven Breitkopf, Jens Limpert, and Andreas Tünnermann, "Coherently-combined two channel femtosecond fiber CPA system producing 3 mJ pulse energy," Opt. Express 19, 24280-24285 (2011)
120. Shian Zhou, Frank W. Wise, and Dimitre G. Ouzounov, "Divided-pulse amplification of ultrashort pulses," Opt. Lett. 32, 871-873 (2007)
121. Yoav Sintov, Ori Katz, Yaakov Glick, Shai Acco, Yehuda Nafcha, Avraham Englander, and Raphael Lavi, "Extractable energy from ytterbium-doped high-energy pulsed fiber amplifiers and lasers," J. Opt. Soc. Am. B 23, 218-230 (2006)
122. R. Paschotta, J. Nilsson, A. C. Tropper, and D. C. Hanna, “Ytterbium- doped fiber amplifiers,” IEEE J. Quantum Electron., vol. 33, pp. 1049–1056, July 1997.
123. Leo A. Siiman, Wei-zung Chang, Tong Zhou, and Almantas Galvanauskas, "Coherent femtosecond pulse combining of multiple parallel chirped pulse fiber amplifiers," Opt. Express 20, 18097-18116 (2012)